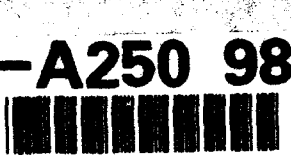
AD-A250 987



1

Interaction of a Turbulent Round Jet with the Free Surface

DTIC
ELECTE
JUN 1 1992
S D
C

K. Madnia and L.P. Bernal
Department of Aerospace Engineering

Contract Number N00014-86-K-0684
Technical Report No. 89-05

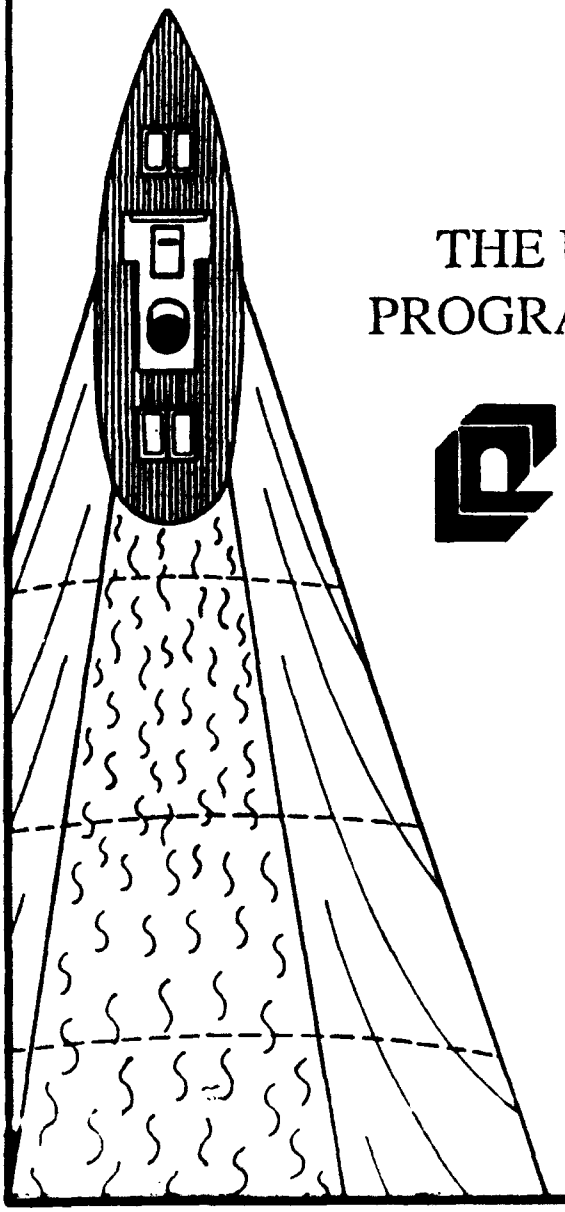
August, 1989

DISTRIBUTION STATEMENT A
Approved for public release;
Distribution Unlimited

92-13786



92 5 26 012



THE UNIVERSITY OF MICHIGAN
PROGRAM IN SHIP HYDRODYNAMICS

COLLEGE OF ENGINEERING

NAVAL ARCHITECTURE &
MARINE ENGINEERING

AEROSPACE ENGINEERING

MECHANICAL ENGINEERING &
APPLIED MECHANICS

SHIP HYDRODYNAMIC
LABORATORY

SPACE PHYSICS RESEARCH
LABORATORY

ERIM

ABSTRACT

An experimental study of the interaction of an underwater turbulent round jet with the free surface was conducted. Flow visualization, surface curvature measurements and hot film velocity measurements were used to study this flow. It is shown that surface waves are generated by the large scale vortical structures in the jet flow as they approach the free surface. These waves propagate at an angle with respect to the flow direction. The propagation angle increases as the strength of the interaction is increased by increasing the momentum flux of the jet or reducing the distance of the jet to the free surface or both. Propagation of these waves in the flow direction is suppressed by the surface current produced by the jet. Far downstream the surface motions are caused by the large scale vortical structures interacting directly with the surface. The fundamental scaling parameters of the free-surface jet have been determined. The velocity scale is the velocity obtained from the combination of jet momentum, density and depth of the jet and the length scale is the distance of the jet to the free surface. It is shown that the centerline velocity decay when scaled with these parameters collapses to a universal curve for different depths of the jet. The asymptotic decay in the far field is reduced by a factor of $2^{1/2}$ compared to the free jet due to the confinement by the free surface. The growth rate of the free-surface jet is found in good agreement with the free jet. However the eccentricity of the jet cross section caused by the displacement of the jet centerline persists for large distances downstream, beyond 40 times the initial depth of the jet centerline. Measurements are also reported on the flow field of a jet moving parallel to a solid surface. These results are compared with the results for the free-surface jet. It is found that the solid wall jet flow is fundamentally different from the free-surface jet flow. The growth rate of the wall jet in the direction parallel to the surface is approximately 3.9 times the growth rate of the free-surface jet. The growth rate of the wall jet in the direction perpendicular to the surface is half the free-surface jet growth rate. This is the result of the different dynamics of vorticity on the free surface compared to a solid wall. The skin friction at the solid wall and increased growth rate combined to give a different maximum velocity decay rate compared to the free-surface jet.

Statement A per telecon Dr. Edwin Rood
ONR/Code 1132
Arlington, VA 22217-5000

NWW 6/1/92

Accession For
NTIS GRA&I
DTIC TAB
Unannounced
Justification
By
Distribution/
Availability Codes
Dist | Avail and/or Special
A-1

TABLE OF CONTENTS

ABSTRACT ii

LIST OF TABLES v

LIST OF FIGURES vi

NOMENCLATURE xv

CHAPTER

I. INTRODUCTION 1

II. EXPERIMENTAL APPARATUS AND INSTRUMENTATION 6

- II.1 Flow Facility 6
- II.2 Flow Visualization 9
- II.3 Surface Curvature Measurements 10
- II.4 Hot film Velocity Measurements 11

III. RESULTS 15

- III.1 Flow Visualization 15
- III.2 Surface Curvature Measurements 18
- III.3 Flow Velocity Measurements 21
  - III.3.1 Free Jet Results 21
  - III.3.2 Free-surface Jet Results 25
  - III.3.3 Wall Jet Results 31

IV. DISCUSSION 34

- IV.1 Mean Flow Characteristics and Scaling of the Free-Surface Jet 34
- IV.2 Surface Waves and Surface Motions 38
- IV.3 Comparisons of a Free-Surface Jet with a Wall Jet 43

V. CONCLUSIONS 48

ACKNOWLEDGMENTS 49

APPENDIX A 50

REFERENCES 54

TABLES 57

FIGURES 61

LIST OF TABLES

Table	Title	Page
2.1	Geometrical characteristics of the jet tanks.	58
2.2	Characteristics of the free shear layer at the jet exit.	59
4.1	Summary of the surface motion and surface wave data.	60

LIST OF FIGURES

Figure		Page
1.1	Schematic diagram of the flow geometry.	62
2.1	Photograph of the experimental facility.	63
2.2a	Photograph of the jet tank.	64
2.2b	Photograph of the jet tank.	65
2.3	Schematic diagram of the free surface tank with jet tank inside.	66
2.4	Schematic diagram of the jet tank.	67
2.5	Schematic diagram of the piping system.	68
2.6	Schematic diagram of the level control apparatus.	69
2.7	Schematic diagram of the apparatus used for the wall jet velocity measurements.	70
2.8	Schematic diagram of the apparatus used for shadowgraph flow visualization.	71
2.9	Schematic diagram of the apparatus used for LIF flow visualization technique.	72
2.10	Schematic diagram of the apparatus used for surface curvature measurements.	73
2.11	Schematic diagram of the surface curvature measurement technique.	74
2.12	Block diagram of the the data aquisition and storage apparatus for the surface curvature measurements.	75
2.13	Block diagram of the the data aquisition and storage apparatus for the hot film velocity measurements.	76
2.14	Schematic diagram of the apparatus used for hot film velocity measurements.	77
2.15	Schematic diagram of the pressure manometer used for	78

measurements of jet exit velocity.

2.16 Plot of measured and calculated calibration velocity data. 79

3.1 LIF photograph of submerged jet flow. Ue = 10 cm, Reynolds number $2.5x10^3$, h/d=1. Region covered 0<x/d<10 80

3.2 LIF photograph of submerged jet flow. Ue = 35 cm/s, Reynolds number $8.9x10^3$, h/d=1. Region covered 0<x/d<10. 80

3.3 Shadowgraph picture of underwater jet flow. Ue = 25 cm/s, Reynolds number $6.3x10^3$, h/d=1. Region covered 1<x/d<10. 81

3.4 Shadowgraph picture of underwater jet flow. Ue = 35 cm/s, Reynolds number $8.9x10^3$, h/d=1. Region covered 1<x/d<10. 81

3.5 Shadowgraph picture of underwater jet flow. Ue = 50 cm/s, Reynolds number $1.27x10^4$, h/d=1. Region covered 1<x/d<10. 82

3.6 Shadowgraph picture of underwater jet flow. Ue = 100 cm/s, Reynolds number $1.27x10^4$, h/d=3.5. Region covered 4<x/d<24. 83

3.7 Shadowgraph picture of underwater jet flow. Ue = 150 cm/s, Reynolds number $9.5x10^3$, h/d=5.5. Region covered 14<x/d<52. 84

3.8 Shadowgraph picture of underwater jet flow. Ue = 250 cm/s, Reynolds number $1.6x10^4$, h/d=5.5. Region covered 14<x/d<52. 84

3.9 Photodiode output signal at x/d=20, y/d=0. U_e = 150 cm/s, Re = $9.5x10^3$, h/d=2.5. 85

3.10 Contour plot of rms value of photodiode output. U_e = 50 cm/s, Re = $3.2x10^3$, h/d=1. 86

3.11 Contour plot of rms value of photodiode output. U_e = 100 cm/s, Re = $6.4x10^3$, h/d=2.5. 87

3.12 Contour plot of rms value of photodiode output. U_e = 150 cm/s, Re = $9.5x10^3$, h/d=2.5. 88

3.13	Contour plot of rms value of photodiode output. U_e = 200 cm/s, Re = 1.27×10^4, h/d=2.5.	89
3.14	Contour plot of rms value of photodiode output. U_e = 100 cm/s, Re = 6.4×10^3, h/d=3.5.	90
3.15	Contour plot of rms value of photodiode output. U_e = 150 cm/s, Re = 9.5×10^3, h/d=3.5.	91
3.16	Contour plot of rms value of photodiode output. U_e = 200 cm/s, Re = 1.27×10^4, h/d=3.5.	92
3.17	Downstream evolution of the rms value of the surface curvature fluctuation along the jet centerline. h/d=2.5	93
3.18	Downstream evolution of the rms value of the surface curvature fluctuation along the jet centerline. h/d=3.5	94
3.19	Downstream evolution of the rms value of the surface curvature fluctuation along the jet centerline. U_e=200 cm/s, h/d=1.5 U_e=50 cm/s, h/d=1.	95
3.20	Power spectrum of the surface curvature fluctuation at x/d=24, y/d=0. U_e = 150 cm/s, Re = 9.5×10^3, h/d=3.5.	96
3.21	Downstream evolution of normalized frequency corresponding to surface curvature fluctuation along the jet centerline.	97
3.22	Power spectrum of the surface curvature fluctuation in the wave region at x/d=28, y/d=12. U_e = 150 cm/s, Re = 9.5×10^3, h/d=3.5.	98
3.23	Velocity profiles for the free jet in the z direction. U_e = 200 cm/s, Re = 1.27×10^4, h/d=24.	99
3.24	Velocity profiles for the free jet in the y direction. U_e = 200 cm/s, Re = 1.27×10^4, h/d=24.	100
3.25	Downstream evolution of maximum mean velocity for the free jet.	101

U_e = 200 cm/s, Re = 1.27x10^4, h/d=24.

3.26 Downstream evolution of half velocity width of the mean velocity profiles for the free jet. U_e = 200 cm/s, Re = 1.27x10^4, h/d=24. 102

3.27 Similarity mean velocity profiles in the y and z directions for the free jet. U_e = 200 cm/s, Re = 1.27x10^4, h/d=24. 103

3.28 Downstream evolution of normalized rms value of the velocity fluctuation on the jet centerline. U_e = 200 cm/s, Re = 1.27x10^4, h/d=24. 104

3.29 Profiles of the rms value of the velocity fluctuation normalized by the local maximum mean velocity on the jet centerline, U_m. U_e=200 cm/s, Re=1.27x10^4, h/d=24, x/d=4, 8. 105

3.30 Profiles of the rms value of the velocity fluctuation normalized by the local maximum mean velocity on the jet centerline, U_m. U_e=200 cm/s, Re=1.27x10^4, h/d=24, x/d=12, 16. 106

3.31 Profiles of the rms value of the velocity fluctuation normalized by the local maximum mean velocity on the jet centerline, U_m. U_e=200 cm/s, Re=1.27x10^4, h/d=24, x/d=20, 24, 32. 107

3.32 Downstream evolution of the normalized frequency of the velocity fluctuations along the jet centerline. U_e=200 cm/s, Re=1.27x10^4, h/d=24. 108

3.33 Time trace of the calibrated hot film velocity signal along the jet centerline at x/d=8. U_e = 200 cm/s, U_{mean} = 157.4 cm/s, U_{rms} = 27 cm/s, Re = 1.27x10^4, h/d=1. 109

3.34 Velocity profiles in the direction perpendicular to the surface. U_e = 200 cm/s, Re = 1.27x10^4, h/d=3.5. 110

3.35 Velocity profiles in the direction perpendicular to the surface. 111

U_e = 200 cm/s, Re = 1.27×10^4, h/d=2.5.

3.36 Velocity profiles in the direction perpendicular to the surface. U_e = 200 cm/s, Re = 1.27×10^4, h/d=1.5. 112

3.37 Velocity profiles in the direction perpendicular to the surface. U_e = 200 cm/s, Re = 1.27×10^4, h/d=1. 113

3.38 Velocity profiles in the direction parallel to the free surface. U_e = 200 cm/s, Re = 1.27×10^4, h/d=3.5. 114

3.39 Velocity profiles in the direction parallel to the free surface. U_e = 200 cm/s, Re = 1.27×10^4, h/d=2.5. 115

3.40 Velocity profiles in the direction parallel to the free surface. U_e = 200 cm/s, Re = 1.27×10^4, h/d=1.5. 116

3.41 Velocity profiles in the direction parallel to the free surface. U_e = 200 cm/s, Re = 1.27×10^4, h/d=1. 117

3.42 Downstream evolution of maximum mean velocity for the free-surface jet. U_e=200 cm/s, Re=1.27×10^4. 118

3.43 Location of the maximum mean velocity as a function of x/d. U_e=200 cm/s, Re=1.27×10^4. 119

3.44 Downstream evolution of the surface velocity normalized by the jet exit velocity U_e. U_e=200 cm/s, Re=1.27×10^4. 120

3.45 Downstream evolution of the half velocity width of the mean velocity profiles for the free-surface jet. U_e=200 cm/s, Re=1.27×10^4. 121

3.46 Downstream evolution of normalized rms value of the velocity fluctuation on the jet centerline. U_e=200 cm/s, Re=1.27×10^4. 122

3.47 Profiles of the rms value of the velocity fluctuation 123

normalized by the local maximum mean velocity.
Plot (a) profiles perpendicular to the free surface.
Plot (b) profiles parallel to the free surface.
U_e=200 cm/s, Re=1.27x10^4, x/d=4.

3.48 Profiles of the rms value of the velocity fluctuation normalized by the local maximum mean velocity. Plot (a) profiles perpendicular to the free surface. Plot (b) profiles parallel to the free surface. U_e=200 cm/s, Re=1.27x10^4, x/d=8. 124

3.49 Profiles of the rms value of the velocity fluctuation normalized by the local maximum mean velocity. Plot (a) profiles perpendicular to the free surface. Plot (b) profiles parallel to the free surface. U_e=200 cm/s, Re=1.27x10^4, x/d=12. 125

3.50 Profiles of the rms value of the velocity fluctuation normalized by the local maximum mean velocity. Plot (a) profiles perpendicular to the free surface. Plot (b) profiles parallel to the free surface. U_e=200 cm/s, Re=1.27x10^4, x/d=16. 126

3.51 Profiles of the rms value of the velocity fluctuation normalized by the local maximum mean velocity. Plot (a) profiles perpendicular to the free surface. Plot (b) profiles parallel to the free surface. U_e=200 cm/s, Re=1.27x10^4, x/d=20. 127

3.52 Profiles of the rms value of the velocity fluctuation normalized by the local maximum mean velocity. Plot (a) profiles perpendicular to the free surface. Plot (b) profiles parallel to the free surface. U_e=200 cm/s, Re=1.27x10^4, x/d=24 128

3.53 Profiles of the rms value of the velocity fluctuation normalized by the local maximum mean velocity. Plot (a) profiles perpendicular to the free surface. Plot (b) profiles parallel to the free surface. U_e=200 cm/s, Re=1.27x10^4, x/d=32. 129

3.54 Power spectrum of the velocity signal at x/d=8; y/d=0 U_e = 200 cm/s, Re = 1.27x10^4, h/d=1. 130

3.55	Downstream evolution of the normalized frequency along the jet centerline. U_e=200 cm/s, Re=1.27x10^4.	131
3.56	Velocity profiles in the direction perpendicular to the solid wall. U_e = 200 cm/s, Re = 1.27x10^4, h/d=1.	132
3.57	Velocity profiles in the direction parallel to the solid wall. U_e = 200 cm/s, Re = 1.27x10^4, h/d=1.	133
3.58	Decay of maximum mean velocity with the downstream distance for the wall jet. U_e = 200 cm/s, Re = 1.27x10^4, h/d=1.	134
3.59	Location of the maximum mean velocity for the wall jet. U_e = 200 cm/s, Re = 1.27x10^4, h/d=1.	135
3.60	Downstream evolution of half velocity width of the mean velocity profiles for the wall jet. U_e = 200 cm/s, Re = 1.27x10^4, h/d=1.	136
3.61	Downstream evolution of the rms value of the velocity fluctuation for the wall jet. U_e = 200 cm/s, Re = 1.27x10^4, h/d=1.	137
3.62	Profiles of the normalized rms value of the velocity fluctuation for the wall jet. Plot (a) profiles perpendicular to the wall. Plot (b) profiles parallel to the wall. U_e = 200 cm/s, Re = 1.27x10^4, h/d=1, x/d=4, 8.	138
3.63	Profiles of the normalized rms value of the velocity fluctuation for the wall jet. Plot (a) profiles perpendicular to the wall. Plot (b) profiles parallel to the wall. U_e = 200 cm/s, Re = 1.27x10^4, h/d=1, x/d=16, 24, 32.	139
4.1	Far field scaling of the free-surface jet.	140
4.2	Decay of maximum mean velocity for the free-surface jet. U_e = 200 cm/s, Re = 1.27x10^4.	141

4.3	Mean velocity similarity profiles for the free-surface jet. Plot (a) profiles perpendicular to the free surface. Plot (b) profiles parallel to the free surface. U_e = 200 cm/s, Re = 1.27×10^4, x/h=10.67, 12, 13.33.	142
4.4	Mean velocity similarity profiles for the free-surface jet. Plot (a) profiles perpendicular to the free surface. Plot (b) profiles parallel to the free surface. U_e = 200 cm/s, Re = 1.27×10^4, x/h=24,32.	143
4.5	Downstream evolution of half velocity width of the mean velocity profiles normalized by the jet depth h.	144
4.6	Downstream evolution of normalized rms value of velocity fluctuation along the centerline of the free-surface jet. U_e = 200 cm/s, Re = 1.27×10^4.	145
4.7	Downstream evolution of normalized frequency along the jet centerline. U_e = 200 cm/s, Re = 1.27×10^4.	146
4.8	Downstream evolution of normalized mean surface velocity for the free-surface jet. U_e = 200 cm/s, Re = 1.27×10^4.	147
4.9	Downstream evolution of normalized frequencies along the jet centerline. Velocity and surface curvature data. U_e = 200 cm/s, Re = 1.27×10^4.	148
4.10	Downstream evolution of the rms value of the surface curvature fluctuation along the jet centerline.	149
4.11	Maximum rms surface curvature fluctuation as a function of the interaction 'strength'.	150
4.12	Location of the maximum rms surface curvature fluctuation as a function of the interaction 'strength'.	151
4.13	Schematic diagram of the flow field for the wall jet.	152

4.14	Decay of maximum mean velocity for the wall jet and the free-surface jet. Solid symbol, wall jet. Open symbols, free-surface jet. U_e = 200 cm/s, Re = 1.27×10^4, h/d=1.	153
4.15	Downstream evolution of half velocity width of the mean velocity profiles for the wall jet and the free-surface jet. U_e = 200 cm/s, Re = 1.27×10^4, h/d=1.	154
4.16	Location of the maximum mean velocity for the wall jet and the free-surface jet. U_e = 200 cm/s, Re = 1.27×10^4, h/d=1.	155
A.1	Geometry of the deformed water surface.	156
A.2	Plot of the location at which the ray of light intersects the photodiode plane, x', versus the location, x, at which the incoming ray intersects the undisturbed surface.	157

NOMENCLATURE

Symbol	Description
d	jet exit diameter
E	output voltage of the hot film signal
E_{max}	output voltage of the hot film signal corresponding to $Ue = Ue_m$
E_{min}	output voltage of the hot film signal corresponding to $Ue = 0$
f	frequency
f_w	fundamental frequency in the wave region
h	distance from the centerline of the jet to the free or solid surface
I_o	incoming light beam intensity
$I(x')$	light intensity at location x'
J_o	jet momentum flux
L_y	half velocity width of the mean velocity profiles in the direction parallel to the free surface
L_z	half velocity width of the mean velocity profiles in the direction perpendicular to the free surface
L'_z	half velocity width of the mean velocity profiles in the direction perpendicular to the free surface and measured from the free surface
n_a	index of refraction of air
n_w	index of refraction of water
N	ratio of n_a / n_w
P_s	static pressure
P_t	total pressure

R	jet nozzle radius
Re	Reynolds number based on jet exit diameter, d
$Re_{\delta 1}$	Reynolds number based on the displacement thickness, δ_1
s	distance from the photodiode or film plate to the undisturbed surface.
St	Strouhal number
t	time
U	mean jet velocity in the axial direction
U_e	jet exit velocity
Ue_m	maximum jet exit velocity set in calibration
U_m	maximum mean velocity
U_{rms}	root-mean-square of the axial velocity fluctuation
U_s	surface velocity in the downstream direction
U_w	minimum dispersion velocity of capillary-gravity waves; $U_w = 23.2$ cm/s
V_L	mean value of the photodiode output voltage
V_{rms}	root-mean-square of the photodiode output fluctuation
V_s	surface velocity in the direction perpendicular to the jet axis
x	Cartesian coordinate aligned in the stream direction
x_m	location of the maximum rms value of the surface curvature fluctuation
x_o	location of the virtual origin of the jet
x'	location of the light ray intersecting the film or photodiode
x_w	x-location of a point in the wave region
y	Cartesian coordinate aligned parallel to the free surface
y_w	y-location of a point in the wave region
z	Cartesian coordinate aligned perpendicular to the free surface

z_m	location of the maximum mean velocity
δ	boundary layer thickness at the jet exit
δ_1	displacement thickness at the jet exit
η	distance to the undisturbed free surface
η'	first derivative with respect to x coordinate
η''	second derivative with respect to the x coordinate
ρ_o	density
θ	momentum thickness at the jet exit
θ_d	deflection angle of the light ray in Figure A.1
θ_i	angle of incident of the light ray in Figure A.1
θ_r	angle of reflection of the light ray in Figure A.1
τ_w	shear stress at the solid wall
$( )_m$	maximum value

CHAPTER I

INTRODUCTION

The results of an experimental investigation of the interaction of a submerged turbulent jet moving parallel to the free surface with the free surface are presented. The flow geometry and parameters are shown in Figure 1.1. One motivation for this study is to obtain a better fundamental understanding of the nature of the free surface waves and motions caused by the interaction of turbulent shear flows with the surface. These flow processes are an important part of the free surface signature of the turbulent wake behind a ship. Aerial and space photographs of the sea surface show distinct features which persist for very large distances behind the ship in the viscous wake region (Munk *et al.* 1987). The turbulent jet/free-surface interaction is one of the simplest flow configurations which incorporates many of the vortical interactions encountered in the turbulent ship wake problem.

An early experimental investigation of the interaction of a submerged jet with the free surface was conducted by Evans (1955). He demonstrated the calming effect on surface waves caused by the surface currents produced by the jet. Evans study did not consider the details of the turbulent flow structure. He showed that when the waves and currents move in the same direction the wave amplitude is decreased. A theoretical analysis of this phenomenon by Taylor (1955) provides an explanation of these results and further show that in this case the wavelength of the surface waves is increased. The effect of nonuniform steady surface currents was also investigated by Longuet-Higgins and Stewart (1961) theoretically (See also Phillips,1966). They consider different types of nonuniform surface currents. They show that if the current is in the same direction as the direction of

propagation of the waves the amplitude of the waves decreases. On the other hand if the waves propagates into a region where the surface current is in the opposite direction as the propagation direction, the amplitude of the waves increases.

Rajaratnam and Humphries (1984) studied the mean flow characteristics of free surface jets when the free surface is located at the edge of the jet nozzle, i.e. h/d=0.5. In their investigation they did not study the free surface motion caused by the jet/free-surface interaction. However they reported a reduction of the mean velocity near the surface at high Froude numbers which was attributed to surface wave generation. For circular surface jets they confirmed the same scaling for the maximum mean velocity decay as for the free jet or wall jet measurements of Rajaratnam and Pani (1974). Self-similarity was found for the mean velocity profiles. The growth rate in the direction perpendicular to the free surface was found equal to the wall jet growth rate while the growth rate in the direction parallel to the free surface was found to be approximately half of the wall jet growth rate. Rajaratnam and Humphries (1984) and more recently Ramberg *et al.* (1989) have studied two-dimensional free-surface jets. They also pointed out the similarity with a wall jet in this case. Ramberg *et al.* noted the pervasive effects of jet confinement in their tank. These confinement effects have been studied by Kotsovinos (1976, 1978). These effects can lead to break down of the similarity scaling laws because of the momentum flux associated with the entrained fluid. Novikov (1988) discussed the mean surface deformation of the free surface caused by an underwater jet. He did not consider the effect of the velocity fluctuations.

The significance of the comparison between the wall jet and the free-surface jet is not immediately obvious. The main similarity between these flows is the confinement by the surface which limits the flow at the free surface or at the wall. However, in a wall jet the no slip boundary condition requires the velocity to be zero at the wall which results in a boundary-layer-like behaviour near the solid surface. On the other hand at a free surface the velocity can be different from zero. The viscous boundary condition at a free surface

requires continuity of normal and shear stresses at the water surface (Batchelor, 1967 Sec.3.3). For a flat free surface and neglecting the shear stress of the air this condition implies zero stress at the surface. Although a free surface boundary layer will form to satisfy the nonsteady viscous boundary condition at the free surface and possible capillary effects, the dynamics of this free-surface boundry layer is fundamentally different than the boundary layer at the solid surface.

Davis and Winarto (1980) studied the interaction of a jet with a solid surface for different distances between the jet and the solid surface. This geometry is the same as the one studied in the present investigation except for the fact that the free surface is replaced by a solid surface. The results of Davis and Winarto are in disagreement with the results of Rajaratnam and Pani (1974). Davis and Winarto (1980) measured a somewhat higher growth rate in the direction perpendicular to the solid wall and somewhat lower growth rate in the direction parallel to the solid wall compared to the the results of Rajaratnam and Pani. This work as well as other investigations of the solid wall jet for different jet exit geometries by Sforza and Herbst (1970), Newman *et al.* (1972), Chandrasekhara and Bandyopadhyay (1975) was reviewed by Launder and Rodi (1981, 1983). Launder and Rodi (1981) noted that the high rate of spanwise spreading of the wall jet may be caused by a secondary motion in the cross-sectional plane. This is attributed to the generation of streamwise vorticity by bending of vortex lines near the wall.

In contrast to the turbulent-jet/free-surface interaction problem the flow characteristics of a turbulent free jet, i.e. in the absence of the free surface, has been the subject of many investigations. It seems appropriate to discuss the underwater flow characteristics in the turbulent jet/free-surface interaction in terms of the flow characteristics of the free jet problem. The flow field can be divided into three regions: the near field, the transition region and the far field (Abramovitz 1963). The mean and turbulent flow properties in the far field of a turbulent jet have been measured by several investigators and most extensively by Wygnanski and Fiedler (1969). In the far field the maximum mean

velocity at each cross-section decays like 1/x, where x is the distance to the jet exit plane, and the width of the velocity profile is proportional to x. This scaling implies that the flux of downstream momentum is constant along the axis of the flow. As mentioned earlier for the two-dimensional jet, Kotsovinos (1978) and Schneider (1985) have investigated the effect of the momentum flux associated with the entrained fluid. They show a continuous reduction of the momentum flux with downstream distance due to this effect.

The turbulent structure of the free jet has been the subject of many investigations. In the near field the potential core region is surrounded by a turbulent shear flow region. For an initially laminar shear layer, instability waves grow exponentially and result in the formation of vortex-ring-like structures which interact with each other by amalgamation as they grow downstream. At the end of the potential core in the transition region vorticity within these structures reaches the centerline and associated with this process there is a characteristic frequency or preferred mode of the jet (Browand and Laufer, 1975, Yule, 1978). In the far field of the jet the evidence for the existence of large scale turbulent structures is convincing (Tso, Kovasznay and Hussain,1981 and Dimotakis *et al.*, 1983). There are however a number of unanswered questions regarding the topology and dynamics of these structures in the far field. It follows that an important aspect of the interaction of the free-surface with the turbulent jet is to determine the effect of the free-surface on these turbulent structures as well as to determine the role of these structures in the dynamics of the free-surface.

In the present investigation, we consider the interaction of a circular jet with the free surface for various depths of the jet below the surface. The main objectives of this investigation are:

- To determine the surface waves and motions produced by the interaction of the turbulent jet with the free surface.
- To determine the scaling characteristics of the underwater turbulent jet.

- To investigate the differences and similarities between the free-surface jet and the wall jet to clarify the role of the boundary conditions at the surface in these flows.

The presentation of the results is organized as follows. In Chapter II the flow facility and instrumentation is described. In Chapter III the results of a flow visualization study, surface curvature measurements and hot film velocity measurements for the free-surface jet and the wall jet are presented. In Chapter IV these results are discussed and finally, in Chapter V, the main conclusions of the investigation are summarized.

CHAPTER II

EXPERIMENTAL APPARATUS AND INSTRUMENTATION

II.1 Flow Facility

The experiments were conducted in a water tank facility specifically designed for flow visualization and Laser diagnostics. Some of the criteria considered in designing this facility are the ability to maintain a constant water temperature and quality, as well as the ability to maintain a constant water level in the free surface tank. Photographs of the facility are shown in Figure 2.1 and Figure 2.2. A schematic diagram of the facility is shown in Figure 2.3. It consists of a free surface tank, a reservoir tank, a jet tank and the associated piping and control valves. The free surface tank was made of glass 76.2 cm wide, 76.2 cm high and 167.6 cm long. The frame for this tank was constructed from steel angles 5.08 cm x 5.08 cm x 0.64 cm and steel plates. The frame was bolted to a double 'Unistrut' structure which raised it 80 cm above the floor for optical access through the bottom surface. The steel frame was isolated from the glass walls by 0.32 cm thick open cell sponge rubber. The side walls were made of 1.27 cm thick glass. The bottom surface was made in two sections. A glass section 1.90 cm x 147.3 cm x 76.2 cm and a PVC section 1.90 cm x 20.3 cm x 76.2 cm. Drainage and water intake are provided by a 5.08 cm diameter hole and a 1.90 cm hole, respectively, located on the PVC section of the bottom face.

Water used in the facility was stored in a 1800 liter reservoir tank. The external dimensions of the reservoir tank are 122 cm in width, 61 cm in height and 244 cm in length. The tank was constructed from 0.64 cm thick sheets of PVC. To further strengthen the tank, it was braced by two 'Unistrut' structures one located at the top and the

other at the mid-height of the tank. The tank was covered with 0.64 cm thick PVC sheet to prevent dust particles and other debris from contaminating the water.

The jet flow was generated by a jet tank located inside the free surface tank. A diagram of the jet tank is shown in Figure 2.4. Water entered the tank from above. Large scale flow nonuniformities associated with the inlet flow were removed by a layer of foam 5.08 cm thick located between two Acrylic sheets with square meshes of 1.27 cm x 1.27 cm as shown in Figure 2.4. The jet exit orifice is located on the side wall at the mid-point between the foam and the bottom of the tank. A circular-arc-shaped nozzle with a radius equal to the wall thickness provides a smooth transition from the side wall of the tank to the jet exit plane. In continuous operation the large area ratio of the contraction helps reduce the turbulent intensity at the jet exit to a level lower than 0.5%. Three jet tanks were used in the experiments with jet exit diameters of 2.54 cm, 1.27 cm and 0.64 cm respectively. The geometrical dimensions of these tanks are presented in Table 2.1. The jet tank for the 1.27 cm exit diameter jet was constructed from 1.27 cm thick Acrylic sheets and was used for flow visualization and surface curvature measurements. The other two were constructed from PVC and Acrylic plate.

The velocity profile at the exit plane of the jet was uniform except for a boundary layer region at the surface. The momentum thickness of the boundary layer, θ, was estimated using Thwaites method. The result for the three jet tanks are presented in Table 2.2. The calculated values of the boundary layer Reynolds number based on the displacement thickness, δ_1, suggests that the boundary layer is laminar except for the higher values of the velocity when it approaches the instability point (See for example Schlichting, 1955.)

Experiments were conducted at several jet exit velocities, U_e, and jet exit depths, h. The jet exit velocity was adjusted with suitable needle valves located in the facility's control panel. The jet exit depth was kept at the desired value by maintaining a constant level in the free-surface tank during the experiment. A schematic diagram of the control panel and the

associated piping is shown in Figure 2.5. In addition to the flow-control needle valves the control panel includes the necessary plumbing for various house keeping chores.

The facility was operated in two different modes, an open loop configuration and a closed loop configuration. The open loop configuration was used in several flow visualization experiments and in the surface curvature measurements. In this case tap water is stored in the reservoir tank and pumped through the facility into the drain. The water level in the free surface tank was kept constant by means of a stand-up pipe technique shown schematically in Figure 2.6. In the open loop operation, the PVC discharge valve is closed so that excess water above the desired level overflows through the stand-up pipe into the level control box and into the drain. In the closed loop configuration water in the free-surface tank is recirculated through the jet tank using the pump. The closed loop operation was used in velocity measurements to maintain a constant temperature and water quality throughout the system during the experiment. The maximum flow rate that can be obtained using the pump in this facility was 15 lit/min. However, operating the facility at such a high flow rate caused excessive recirculation in the free surface tank. Therefore, the facility was operated at considerably lower flow rates. The entrainment velocity was calculated using the results of Ricou & Spalding (1961). The value of the recirculation velocity for U_e=200 cm/s, d=0.64 and x/d=40 was estimated to be 0.23 cm/s which is approximately 0.7% of the local maximum mean velocity. The maximum jet exit velocity used was 220 cm/s in the 0.64 cm diameter jet tank.

Experiments were also conducted on the interaction of the jet with a flat solid surface. A schematic diagram of the experimental apparatus used is shown in Figure 2.7. The apparatus and instrumentation used were the same as for the jet / free-surface interaction experiments, with the addition of a solid wall. The solid wall was made of 0.64 cm thick PVC plate 61 cm long and 55 cm wide. In order to stiffen the plate, PVC angles 5.08 cm x 5.08 cm x 0.64 cm were glued on the edges and one on the center of the plate. The surface of the plate was smoothened by polishing it with steel wool. The plate

was suspended from the edges of the free surface tank by four 1.27 cm diameter stainless steel threaded rods. It was then set against the jet tank at the desired height below the jet nozzle. The small gap between the plate and the jet tank was covered by a water-proof transparent tape. The plate was made flat to within 0.3 mm over its total length of 60.1 cm. In these experiments the free surface was located at least 28 jet exit diameters from the centerline.

II.2 Flow Visualization

Flow visualization of the free surface deformation and of the jet fluid was obtained using the shadowgraph technique. A schematic diagram of the optical system used is shown in Figure 2.8. A collimated beam of light 30 cm in diameter was formed from the output beam of a Copper Vapor Laser 2.2 cm in diameter by means of a focussing lens and a spherical mirror. A 30 cm x 30 cm first surface mirror was utilized to direct the collimated beam of light through the bottom glass window perpendicular to the undisturbed free surface. Refraction at the water-air interface causes variations in beam intensity in the regions where the free surface is not perpendicular to the beam. The resulting shadow image was viewed on a screen located above and close to the free surface. The pictures presented here were obtained by photographing the image on the screen with a 35 mm camera. The jet fluid was simultaneously visualized by using 1-2 °C warmer water in the jet tank. The corresponding change in the index of refraction results in the light intensity variation typical of shadowgraph images. Motion pictures of this flow were also obtained using a Hycam Model K20S4E high speed camera at a nominal frame rate of 100 pictures per second.

Laser Induced Fluorescence (LIF) was used to visualize cross-sections of the underwater flow. A schematic diagram of the apparatus used for LIF flow visualization is shown in Figure 2.9. A fluorescent dye (Rhodamine 6G) with a concentration of 2 ppm was homogeneously mixed with water in the jet tank. The dyed water was then driven

through the jet nozzle into clear water in the free surface tank. Excitation of the fluorescence was induced by a plane sheet of light from a Copper Vapor Laser formed by a combination of cylindrical lenses with focal lengths of -60mm, 100mm and 150mm corresponding to lenses L1, L2 and L3, respectively, in Figure 2.9. This combination of lenses allowed control of the thickness and width of the laser sheet. The sheet thickness was 1-2 mm over the region of observation. Rhodamine 6G dye fluoresces efficiently when excited by the green (511 nm) line of the Copper Vapor Laser. The scattered light, yellowish in color, from dye-containing fluid in the plane of the laser sheet was then recorded by a 35 mm camera positioned perpendicular to the sheet.

II.3 Surface Curvature Measurements

Surface curvature measurements were conducted to quantify the various surface features observed in the flow visualization study. A schematic diagram of the apparatus used for these measurements is shown in Figure 2.10. The technique used is based on the same principle as the shadowgraph flow visualization technique. In this case a photodiode (SKAN-A-MATIC Model S118 1/4) was used to measure the temporal fluctuation of light intensity at a fixed point on the surface. The diameter of the photocell was 5 mm and it had a nominal frequency response of 300 KHz. A 1 mm diameter circular aperture was utilized to improve the spatial resolution of the measurements. In the experiments the photodiode was positioned 0.64 cm above the water surface. A collimated beam of light was formed using the 514.5 nm line of an argon-ion laser (Lexel Model 95) as the light source. Following the notation in Figure 2.11 the light intensity at the photodiode aperture from a two-dimensional deformation of the surface η is given by

$$I(x') = I_o \left| \frac{dx}{dx'} \right|$$

where x' is the location of the photodiode and x is the location where the ray captured by the photodiode intersects the surface. In the limit of small surface deformations $\frac{\eta}{s} << 1$,

small surface slope $\frac{d\eta}{dx} << 1$ and small surface curvature $s\frac{d^2\eta}{dx^2} << 1$, it can be shown that the light intensity measured by the photodiode is given by

$$I(x') = I_o \left\{ 1 - s(n_w - 1) \frac{d^2\eta}{dx^2} \right\}$$

where s is the distance from the photodiode to the water surface and n_w is the index of refraction of water. Thus in this limit the light intensity measured by the photodiode is proportional to the surface curvature. A detailed analysis of this relationship between the light intensity measured by the photodiode and the surface deformation is presented in Appendix A.

Figure 2.12 is a block diagram showing the data acquisition and storage system. The signal from the photocell was DC shifted, amplified and filtered using a Tektronix AM 502 differential amplifier. The analog output of the filter was then digitized using a Lecroy Model 8210 Transient Digitizer. Typical sampling rate was 200 Hz. The digitized output was then stored on permanent files using an IBM CS9000 mini computer.

II.4 Hot Film Velocity Measurements

Velocity data were obtained using a constant temperature hot film anemometer. A standard TSI quartz coated cylindrical sensor with a frequency response of approximately 80 KHz was used in the measurements. The sensor length was 0.51 mm and the diameter 25 μm. The sensor axis was positioned perpendicular to the flow direction and parallel to the free surface. The hot film was operated at the overheat ratio of 1.09. Figure 2.13 is a block diagram of the electronics and data acquisition system. A TSI Model 1750 constant temperature anemometer box in conjunction with a TSI Model 1056 Decade Resistance box, with a resolution of 0.01 Ω, was used to obtain the data. The output of the anemometer was DC shifted and amplified using a Tektronix AM501 operational amplifier

wired as a differential amplifier with a gain of 2.6. The output of the differential amplifier was digitized using a Lecroy Model 8210 Transient Digitizer. Typical sampling rates used were between 200-800 Hz. The digitized output was then stored on permanent files using an IBM CS9000 computer.

A schematic diagram of the apparatus used for velocity measurements is shown in Figure 2.14. The hot film probe was mounted on a computer controlled traverse mechanism. The traversing gears in the axial (x-axis) and transverse (y-axis) directions were actuated by two Sigma Model 18-1408 D40-F stepping motors with a 50:1 gear ratio (Willmarth, 1977). A Transicoil Model U-217094 Gearhead Stepper Motor with a gear ratio of 60:1 was used to move the probe in the direction perpendicular to the free surface. The stepping motor was controlled by the IBM CS9000 computer using a parallel port. An interface circuit was designed and built to convert the parallel port output to the required control signals for the stepping motor. It provided full three-dimensional positioning of the probe. The resolution of the traverse motion along the axial and transverse directions was 25 μm and in the vertical direction was 6.86 μm.

The hot film probe was calibrated in the same free surface tank facility used in the experiments by locating it at the jet exit and varying the jet exit velocity. The jet exit velocity was measured by a manometer which was constructed using a precision Vernier Caliper, 0.64 cm diameter glass tubing and 0.95 cm diameter Tygon tubing. A schematic diagram of the pressure manometer is shown in Figure 2.15. The height of the column of water corresponding to the total pressure P_t and the static pressure P_s at the exit of the jet were measured using the manometer. The difference between the total and static pressures, measured in cm of water, is proportional to the square of the jet exit velocity. For each jet exit velocity, the output voltage of the amplifier and the exit velocity obtained from the manometer were recorded. A typical calibration curve is shown in Figure 2.16. The solid line on this plot is a fourth order polynomial fit through the measured data obtained using the least squares method. The triangles in this figure represent the measured

data points. The error between the measured and calculated values is less than 1% of the maximum jet exit velocity U_{e_m}. The calibration curve was incorporated into the Data Acquisition software and used to obtain the velocity for each measured value of the hot film output voltage.

In order to minimize probe interference with the free surface at close distances to the free surface, the probe was tilted backward by 4 degrees (See Figure 2.14). The velocity calibration was performed with the probe in the tilted position. The closest point to the water/air interface for which the measurements were performed was at 0.64 mm from the surface. At this point the hot film sensor was intermittently in and out of the water, which resulted in sharp voltage spikes on the time trace of the velocity signal. The velocity data corresponding to the points close to the surface were examined and those contaminated with sharp spikes were discarded.

For the wall jet velocity measurements, the probe support was modified in order to gain access to the jet exit orifice and to conduct measurements as close as possible to the wall. Referring to Figure 2.7, the 90 degrees angle adapter was removed from the probe support. The probe was mounted directly on the probe support which was tilted backward at an angle of 9 degrees as shown in Figure 2.7. The closest point to the flat plate for which data could be obtained was at 0.25 mm above the plate. The probe was calibrated in this configuration by position it at the exit of the jet.

In the velocity measurements particular emphasis was placed on insuring a constant temperature and quality of the water in the tanks to minimize drift of the velocity signal. The water temperature and the probe's cold resistance were monitored during the measurements. The water temperature was maintained constant to within 0.5 °C. In order to improve the water quality, the tap water was passed through a nominal 5 μm sediment removal filter and a water softener filter before filling the reservoir tank. To inhibit the growth of one-celled animal and plant life, Chlorine with the concentration of 3 ppm was added to the water in the reservoir tank. The reservoir tank was covered with a sheet of

gray PVC 0.64 cm thick to prevent light, dust and dirt particles from falling into the clean water. The water stored in the reservoir tank was used to fill the free surface tank to the desired height. The jet was produced by recirculating the clean treated water in the free surface tank using the pump. To insure that no significant drift in the hot film instrumentation occurred, the probe was moved to the jet exit orifice at the end of each traverse and the jet exit velocity measured. If a significant change in the measured velocity at the jet exit were detected the measurements were discharged.

CHAPTER III

RESULTS

III.1 Flow Visualization

Figures 3.1 and 3.2 show LIF photographs of the jet development and interaction of the jet with the free surface. In both figures the jet flow is from left to right and the jet centerline was positioned one diameter below the surface. Figure 3.1 shows a cross-section view of the underwater jet through the symmetry plane at a Reynolds number of approximately 2.5×10^3. The vortex ring like structures in the potential core of the jet ($0<x/d<4$) are clearly observed in this image. As they convect downstream these vortical structures interact with each other and with the surface. From this image the interaction of the jet with the surface begins at approximately $x/d=4$. Downstream of this point smaller scale features are observed. Figure 3.2 shows a similar cross-section obtained at a Reynolds number of 8.9×10^3. In this case the vortical structures are formed with a wavelength smaller than in Figure 3.1. The wavelength of the vortical structures increases with downstream distance. The interaction with the free surface starts also at approximately $x/d=4$, the same value as for the flow in Figure 3.1. The wavelength of the structures at the beginning of the interaction with the free surface is approximately the same in both pictures.

Typical flow visualization shadowgraph pictures of jet/free-surface interaction are presented in Figures 3.3 to 3.8. In all cases the flow is from left to right. The jet fluid is visualized by a slightly lower temperature of the jet tank fluid. Figures 3.3 to 3.5 were obtained at a jet exit depth corresponding to $h/d=1$. In these cases the interaction of the jet with the free surface occurs in the near field of the jet. Figure 3.3 shows the interaction at

low jet exit velocity as indicated. Near the jet exit the vortex-ring-like structures can be observed. These structures interact with the free surface and produce characteristic surface deformations which travel with the vortices. The light intensity pattern along the jet centerline in Figure 3.3 indicates a depression of the surface on top of the core of the vortices and an elevation of the surface between the vortices. Further downstream the jet vortical fluid interacts with the surface. In this region the shadowgraph image of the jet fluid is dominated by the small scale features in the flow. A remarkable feature in this photograph are the two dark spots located at x/d≈4. The dark spots are associated with vortex lines terminating at the free surface (Berry and Hajnal 1983 and Sterling *et al* 1987). They are generated by opening of vortex lines of the initially submerged coherent eddy. This type of interaction has been investigated by Bernal and Kwon (1989) and Kwon (1989) for axisymmetric vortex rings.

The flow pictures in figures 3.4 and 3.5 were obtained at jet exit velocities of 35 cm/s and 50 cm/s respectively. These pictures show typical surface wave patterns produced by the interaction of the jet with the free surface. The flow conditions in Figure 3.4 are slightly above the values for which surface waves are first observed. The vortex-ring-like structures moving underneath the surface start deforming the surface at a distance of x/d≈1, and it is not before a distance of x/d≈4 for which waves are produced. At these flow conditions the waves are produced in the region where the coherent eddy opens up in Figure 3.3. The resulting wave fronts propagate at an angle of 39 degrees with respect to the downstream direction. Downstream of the wave generation region the turbulence in the jet interacts with the free surface. Dark spots indicating vortex lines terminating at the free surface are observed in this region. At a higher jet exit velocity in Figure 3.5 the waves are generated over a larger region in the downstream direction. In this case the waves are initially formed at x/d≈4 and propagate at an angle of 60 degrees relative to the downstream direction. However the wavefronts curved farther downstream suggesting a steepening of the direction of propagation. Along the centerline the wavefronts are quite well-defined and

are normal to the flow direction. This picture and the motion pictures of the flow obtained at the same flow conditions show an increase of the wavelength of the waves as they propagate along the centerline.

The same basic features observed in the near field interaction are also found when the interaction occurs in the far field of the jet. Figure 3.6 is an instantaneous (1-2μs) spark shadowgraph picture of the flow field at a Reynolds number of 1.27×10^4 and h/d=3.5. The corresponding jet exit diameter was d=1.27 cm. The shadowgraph image of the flow shows small scale turbulent structures in the submerged jet fluid. Although more remarkable is the deformation of the surface at x/d≈16 which is caused by the interaction of a large scale vortical structure approaching the surface. As can be observed from the picture, the size of this structure is comparable with the local width of the jet. It is striking that similar large scale structures are not seen on the shadowgraph image upstream of the interaction with the free surface. A plausible explanation is that the intensity variation on the shadowgraph image is due to variations of the second order spatial derivative of the index of refraction integrated along the beam path. It follows that the shadowgraph image of the turbulent region enhances the small scale structures in the flow. As the turbulent jet reaches the surface the refraction effects associated with the surface deformation dominate the shadowgraph image. This surface deformation is caused by the large scales in the jet flow. Also from Figure 3.6, a measure of the visual growth rate of the jet upstream of the interaction can be determined which gives a value of 11 degrees for the half angle.

Figures 3.7 and 3.8 are shadowgraph images of the flow for h/d=5.5 and Reynolds number of approximately 9.5×10^3 and 1.6×10^4 respectively. At the lower jet exit velocity, Figure 3.7 shows surface deformation caused by the large scale turbulent structures in the jet at an axial location of x/d≈25 on the left side of the photograph. Weak surface waves are observed propagating at an angle of 42 degrees relative to the downstream direction. Farther downstream the vortical fluid in the large scale structures breaks the surface resulting in complicated surface patterns (x/d≈33). Again the dark spots

associated with the vortex lines terminating at the free surface are clearly visible in this photograph. At higher jet exit velocity, in Figure 3.8, the surface deformations caused by the large scale structure in the jet results in stronger surface waves being generated at the interaction. The waves propagate at an angle of 54 degrees relative to the downstream direction. In this Figure the wavelength of the surface waves is approximately 7 cm compared to values of the order of 2 cm measured in the near field interaction of Figures 3.4 and 3.5. The location where waves are first observed x/d≈25 and the location where the vortical fluid breaks the surface x/d≈33 are approximately the same as for the low velocity conditions in Figure 3.7.

III.2 Surface Curvature Measurements

The surface curvature measurements were conducted to quantify the various surface features produced by the interaction of the jet with the free surface. The measurements were performed by locating the photodiode on a matrix of 54 points and recording the temporal fluctuations of light intensity at each point on the surface. An area of 22.9 cm x12.7cm was covered at 2.54 cm intervals. A typical time trace of the photodiode output as recorded by the Digital Data Acquisition System is shown in Figure 3.9. No attempt was made to calibrate this signal in terms of the surface curvature. However all the data were obtained at the same conditions of illumination, amplifier gain and with the photodiode at the same distance to the surface so that meaningful comparisons between the results of various tests can be conducted. The mean value of the photodiode output signal, V_L, is related to the local light intensity of the collimated beam, I_o. The temporal fluctuation of the output is the result of temporal fluctuations of the surface curvature at the probe location. Therefore the rms value of the photodiode output, V_{rms}, is a measure of the rms amplitude of the surface curvature fluctuations.

The rms value of the photodiode output fluctuation were mapped over the region of interaction of the jet with the free surface at several flow conditions. The results are

presented in Figures 3.10 to 3.16 in the form of contour plots of the rms value at each flow condition. Also shown in each plot is a straight solid line which corresponds to the visual growth of the free jet determined on the shadow image in Figure 3.6. A common feature of all contour plots is that along the centerline the rms value reaches a maximum some distance from the nozzle and then decreases farther downstream. This corresponds to the region of maximum surface activity on the flow pictures. The lateral extent of surface activity region clearly extends beyond the visual growth of the free jet. This is due to the propagation of waves away from the interaction region. The surface area bounded by a contour line for relatively small values of the rms can be loosely characterized as a sector of a circle. The straight lines on the upstream side of the sector corresponds to the direction of propagation of waves at the beginning of the interaction region. This angle changes with flow conditions.

Figure 3.10 was obtained at $Re=3.2x10^3$ and jet exit depth corresponding to h/d=1. At these flow conditions the maximum interaction occurs in the near field x/d=4. Figures 3.11 to 3.13 were obtained at h/d=2.5 for jet exit velocities of 100 cm/s, 150 cm/s and 200 cm/s respectively. Figures 3.14 to 3.16 were obtained at h/d=3.5 for the same jet exit velocities. In all cases the jet exit diameter was 0.64 cm. The corresponding Reynolds number varied from $6.4x10^3$ to $1.27x10^4$ as indicated. For a fixed depth, as the jet exit velocity is increased the location of the maximum interaction moves downstream and, also, the propagation angle of waves generated at the beginning of the interaction region is increased. This behaviour is found for both h/d=2.5 (Figures 3.11 to 3.13) and h/d=3.5 (Figures 3.14 to 3.16). The effect of increasing depth for a constant jet exit velocity is a displacement of the maximum interaction point farther downstream and to decrease the propagation angle of waves generated at the beginning of the interaction.

A better measure of the rms value of the surface curvature fluctuation is obtained by normalizing V_{rms} with the local mean light intensity, V_L. The downstream evolution along the centerline of the normalized rms values of the surface curvature fluctuation V_{rms}/V_L, for

several flow conditions is shown in Figures 3.17, 3.18 and 3.19. The results plotted in Figure 3.17 correspond to a normalized jet exit depth h/d=2.5, at several jet exit velocities and for different jet exit diameters as indicated in the figure caption. The results plotted in Figure 3.18 correspond to h/d=3.5 and for several jet exit velocities and jet exit diameters as well. The results for Figure 3.19 are for h/d=1.5, U_e=200 cm/s and h/d=1, U_e=50 cm/s. The jet exit diameter for both cases was d=0.64 cm. Several trends are readily identified in the data. At a fixed normalized depth, say for h/d=2.5 (Figure 3.17), the effect of increasing jet exit velocity is to increase the maximum value of V_{rms}/V_L and to displace the location of the maximum value downstream. The effect of jet exit diameter for fixed jet exit velocity and normalized depth is very small. At the larger value of h/d the same trends are observed for variations of the jet exit velocity and the jet diameter. The effect of the normalized depth h/d on these profiles is determined by comparing the various curves in Figures 3.17, 3.18 and 3.19. It is apparent that increasing h/d results in a displacement of the interaction point in the downstream direction and, for the same jet exit velocity, a reduction of the maximum value of V_{rms}/V_L.

The surface curvature fluctuations were further characterized with power spectrum measurements along the nterline of the flow and at selected locations away from the centerline where waves were observed in the pictures. Figure 3.20 is a typical plot of the frequency power spectrum measured on the centerline at x/d=24 for U_e=150 cm/s and h/d=3.5. This point corresponds to point 1 in Figure 3.15 in the region of maximum rms fluctuation for this flow conditions. The vertical axis in this power spectrum plot is normalized with the square of the rms value so that the area under the curve is unity. There is a distinct peak in the power spectrum at a frequency of 8 Hz. The corresponding normalized frequency using jet exit parameters is $fd/U_e = 0.034$ at least an order of magnitude below the value for the preferred mode for the free jet at these conditions. Similar power spectrum plots were obtained along the centerline at other flow conditions. From these plots the frequency corresponding to the maximum power spectral density was

determined. The results are presented in Figure 3.21 where this frequency normalized with the jet exit velocity and diameter is plotted as a function of x/d for several values of h/d. The diameter of the jet was 0.64 cm in all cases. For h/d=3.5, solid symbols, the measured frequency is approximately constant up to x/d= 40 the farthest location measured in this case. In contrast for h/d=2.5 and 1.5 there is a significant drop of the frequency for the larger values of x/d. There is also significant scatter among the normalized frequency measured at different flow conditions suggesting that the jet exit parameters are not the most appropriate scaling parameters for this flow.

The power spectrum measured along the centerline can also be compared with a similar power spectra measured away from the centerline. Figure 3.22 is such a power spectrum measured at x/d=28 and y/d=12 for U_e=150 cm/s and h/d=3.5, the same flow conditions as for the power spectrum in Figure 3.20 but at point 2 in Figure 3.15. The power spectrum shows three distinct peaks of frequencies of 8 Hz, 16 Hz and 24 Hz. The tallest peak occurs at the same frequency as the peak in point 1 (Figure 3.15) on the centerline. The fact that the frequencies are the same indicates that the measured surface deformations are the result of waves propagating through points 1 and 2 on the surface. This is of course consistent with the results of the flow visualization study.

III.3 Flow Velocity Measurements

III.3.1 Free Jet Results

A systematic study of the flow field caused by the jet at a large distance from the free surface was conducted to determine the free jet behaviour in the facility. As mentioned earlier the jet establishes a recirculating flow in the free surface tank. While this effect is expected to be small, the free jet data was measured in the tank to confirm this expectation and to provide basic data for comparison with the free surface cases discussed below. The measurements were conducted at a jet exit velocity of 200 cm/s and jet exit diameter d=0.64

cm. The corresponding Reynolds number is $Re=1.27x10^4$. The centerline of the jet was positioned 24 diameters below the surface (h/d=24).

The mean and rms value of the velocity fluctuation was measured along vertical and horizontal traverses at several distances from the jet exit plane. The measured mean velocity profiles are shown in Figure 3.23 for the vertical profiles (z-direction) and in Figure 3.24 for the horizontal profiles (y-direction) respectively. In these figures the velocity profiles are normalized with the maximum mean value of the velocity, U_m, measured at each cross-section on the centerline. The vertical or horizontal coordinate is measured from the centerline and is normalized by the jet exit diameter. In each figure the measured profiles at x/d=4, 8, 12, 16, 20, 24, 32 and 40 are presented. Also shown in Figures 3.23 and 3.24 are the definition of the half velocity width of the jet along the vertical, L_z, and horizontal, L_y, directions. As customary the half velocity width is defined as the distance from the centerline to the point on the profile where the velocity is one half the maximum velocity on the centerline. It is apparent that the velocity profiles measured in the horizontal and vertical directions are very similar which confirms the axial symmetry of the flow and indicates that the spatial resolution of the hot wire probe in the horizontal and vertical directions is adequate for the study as mentioned earlier in Section II.4.

The two main features of the mean velocity field in the jet is the lateral growth of the profiles with downstream distance clearly observed in Figures 3.23 and 3.24 and the corresponding decay of the centerline velocity, U_m. This effect is not immediately obvious in the profiles in Figures 3.23 and 3.24 because they are normalized with the local maximum velocity. The downstream evolution of the measured maximum value of the mean velocity along the centerline is shown in Figure 3.25. In this plot the ratio U_e/U_m is plotted as a function of x/d. The decay of U_m with downstream distance implies an increase of U_e/U_m with x/d as shown in Figure 3.25. Also the linear growth of U_e/U_m with x/d expected from similarity arguments is found downstream of x/d=12. A least squares fit to the data for $x/d \geq 12$ gives

$$\frac{U_e}{U_m} = 0.162\,(\frac{x}{d} - 1.9)$$

This result for the free jet is in good agreement with the results of other investigators (e.g. Wygnanski and Fiedler 1969, Rajaratnam 1976, Davis and Winarto 1980 and Rajaratnam and Humphries 1984). It indicates that the finite size of the facility does not result in a significant change in the decay of the centerline velocity. Although the momentum flux may be reduced as the flow develops downstream (Schneider 1985), its effect on U_m is within the scatter of the data.

A quantitative measure of the lateral growth of the jet can be obtained from the evolution with downstream distance of the half velocity width of the velocity profiles. The results are shown in Figure 3.26 where the normalized half velocity width in the vertical direction, L_z/d (open symbols), and in the horizontal direction, L_y/d (solid symbols), are plotted as a function of the normalized downstream distance, x/d. As indicated earlier the measured widths are almost the same in the horizontal and vertical direction at all downstream locations. In the far field, the results show the expected linear growth with downstream distance. A least squares fit to the data for $x/d \geq 12$ gives

$$\frac{L_z}{d} = \frac{L_y}{d} = 0.078(\frac{x}{d} + 0.97)$$

This result is also in good agreement with the measured values reported in the literature (e.g. Wygnanski and Fiedler 1969, Rajaratnam 1976, Davis and Winarto 1980, and Rajaratnam and Humphries 1984). It implies that the small recirculating flow in the free-surface tank has no apparent influence on the growth of the free jet. It is interesting to compare the growth rate determined from the half width of the velocity profile with the visual growth of the jet obtained in Figure 3.6. The value of 0.078 of the slope of the half velocity width implies a divergence angle of 4.5 degrees which is approximately one half the visual divergence angle of 11 degrees measured in Figure 3.6. Note that these angles are measured with respect to the centerline of the jet.

The mean centerline velocity and the half velocity width evolution indicate that similarity is obtained for x/d≥12. This implies that the mean velocity profiles measured downstream of x/d=12 should collapse on a single profile when the mean velocities are normalized by the maximum velocity in the profile and when the transverse coordinates y or z are normalized with the corresponding half-widths L_y or L_z respectively. The similarity velocity profiles obtained from these data are shown in Figure 3.27. There is good collapse of the data. The scatter of the data is due to uncertainty of the position measurement and calibration of the hot wire probe.

The turbulent fluctuations of the velocity were characterized at each measurement point by the rms value. Also the power spectrum of the velocity fluctuation was measured along the centerline. Figure 3.28 is a plot of rms value of the velocity fluctuation normalized by the mean velocity, both measured on the centerline of the jet, as a function of downstream distance. The turbulence intensity U_{rms}/U_m increases to a value of approximately 0.23 for x/d>20. This value is in agreement with the results of Davis and Winarto (1980). A value of U_{rms}/U_m=0.28 was measured at large downstream distances (x/d≥40) by Wygnanski and Fiedler (1969). Comparison with the mean velocity evolution indicates that similarity is reached farther downstream for the turbulence intensity. These results suggest a value of x/d=32 for the turbulent intensity compared to x/d=12 for the mean velocity profiles. Davis and Winarto (1980) find a similar result while Wygnanski and Fiedler (1969) gives a value of x/d=40 to reach similarity for the turbulence intensity.

Profiles of the rms value of the velocity fluctuation normalized by the local maximum mean velocity on the centerline as a function of transverse coordinate normalized by the corresponding half velocity width are plotted in Figures 3.29 to 3.31. In these figures solid symbols correspond to profiles measured along the horizontal direction and the open symbols correspond to the vertical direction. Figure 3.29 for x/d=4 and 8 show a well defined minimum of the turbulent intensity on the centerline. The minimum is more pronounced at x/d=4 compared to x/d=8. This is associated with the termination of

potential core region in the near field of the jet. The two maximum values on either side of the minimum at the centerline increase slightly from x/d=4 to x/d=8. The rms velocity profiles at x/d=12 and x/d=16 are shown in Figure 3.30. The minimum at the centerline, if present, is within the scatter of the measurements. The plot also shows an increased normalized rms value on the center region compared to the profiles measured closer to the jet. At x/d=20, 24 and 32 the results presented in Figure 3.31 show large scatter. This is associated with the increased uncertainty of the measurements at these locations where the measured velocities are small. The basic trends observed in these figures are consistent with measured rms velocity profiles by Davis and Winarto (1980), Wygnanski and Fiedler (1969) and others. A common feature in these profiles (Figures 3.29-3.31) is the good agreement, within the uncertainty of the measurements, found between the horizontal and vertical profiles. This is a expected result from the axial symmetry of the free jet flow.

The power spectrum of the velocity fluctuations was measured along the centerline of the jet. A distinct peak is found where the power spectral density is maximum. The frequency corresponding to this maximum was determined as a function of downstream location. This maximum frequency can be associated with the passage frequency of the large scale turbulent eddies at a particular location in the flow. The variation of this frequency normalized with jet exit parameters, fd/U_e, as a function of normalized distance downstream, x/d, is shown in Figure 3.32. Close to the nozzle at x/d=4 the value of fd/U_e=0.36 corresponds to the preferred mode of the jet (Gutmark and Ho, 1983). Far downstream, x/d=12, the frequency decreases as x^{-2} as expected from similarity arguments.

III.3.2 Free-surface Jet Results

Velocity measurements for the free-surface jet were conducted at a jet exit velocity of 200 cm/s and a jet exit diameter of 0.64 cm which corresponds to a Reynolds number of

1.27×10^4. The jet centerline was positioned at several depths below the surface corresponding to h/d=1, 1.5, 2.5 and 3.5.

A typical time trace of the velocity measured at x/d=8 for h/d=1 is shown in Figure 3.33. The velocity field at this and all other points were characterized by the mean value of the velocity, in this case 157.4 cm/s, and the rms value of the fluctuation, in this case 27 cm/s. In addition the characteristic time scales in the flow were characterized by power spectrum measurements at selected locations in the flow.

Mean velocity profiles were measured as a function of downstream distance along directions perpendicular to the free surface, Figures 3.34 to 3.37, and parallel to the free surface, Figures 3.38 to 3.41, for various depths of the jet. In all cases the measured mean velocity profiles are normalized by the maximum velocity, U_m, measured at each cross section. The transverse coordinates measured from the jet centerline are normalized by the jet exit diameter d. Figure 3.34 shows the velocity profiles measured at h/d=3.5 and several distances from the jet exit plane. The location of the free surface is indicated in the figure. As the flow evolves downstream the jet reaches the free surface resulting a mean velocity at the surface different from zero. For $x/d \leq 16$ the jet has not reached the surface and the velocity profiles are very similar to the free jet velocity profiles. Downstream of this station the normalized mean velocity at the point closest to the surface increases. However, at this depth the maximum mean velocity is always found at the centerline of the jet. As the jet is positioned closer to the free surface, Figure 3.35 for h/d=2.5, the mean velocity profiles reach the free surface somewhere downstream of x/d=8. As in the case h/d=3.5 the normalized mean velocity at the point closest to the surface increases downstream of that point. The maximum velocity on the profile is located on the centerline at all distances documented.

The same trends are found for smaller values of h/d. For h/d=1.5 in Figure 3.36 the beginning of the interaction is found between x/d=4 and x/d=8. In this case the maximum velocity at x/d=40 no longer occurs on the centerline of the jet but moves closer

to the free surface. For h/d=1, Figure 3.37, the beginning of the interaction occurs upstream of x/d=4. The maximum mean velocity on the profiles downstream of x/d=24 move towards the free surface. As indicated in Section II.4 the minimum distance to the free surface at which measurements could be obtained was 1.9 mm which corresponds to 0.3 times the jet exit diameter.

The mean velocity profiles measured along the direction parallel to the free surface are shown in Figures 3.38 to 3.41 for h/d=3.5, 2.5, 1.5 and 1 respectively. The same normalization as for the vertical profiles was used. These profiles were measured on a plane containing the centerline of the jet. As noted in the discussion of Figures 3.36 and 3.37 the mean velocity on the centerline is not the maximum value measured on the cross section for h/d=1.5,x/d=40 (Figure 3.40) and h/d=1, x/d=32 and 40 (Figure 3.41). However at these conditions the centerline velocity is very close to the maximum value on the cross section ($U/U_m \geq 0.98$) so that in the plots this value on the centerline can not be differentiated from unity. At a fixed downstream distance the measured mean velocity profiles for various depths are very similar to each other and also to the profiles measured in the free jet (Figures 3.23 and 3.24). A more detail comparison is conducted below in terms of the half velocity width measured on these profiles.

As for the free jet, the maximum mean velocity at each cross section decreases with downstream distance. This evolution of the mean centerline velocity is shown in Figure 3.42 for h/d=1, 1.5, 2.5 and 3.5. In this figure the parameter U_c/U_m is plotted as a function of x/d. Also shown in this figure is a solid line which corresponds to the least squares fit to the free jet data discussed above (See Figure 3.25). For $x/d \leq 16$ the mean centerline velocity in the free-surface jet follows the same evolution as the free jet for all values of h/d. Farther downstream the values of U_c/U_m for the free surface jet are generally lower than the corresponding value for the free jet (solid line). This result implies that the mean centerline velocity decay is slower in the free surface jet compared to the free

jet. The effect is more pronounced for the smaller values of h/d. For h/d=3.5 the departure from the free jet data can only be observed for x/d≥32.

The mean velocity profiles showed a displacement of the location of the maximum mean velocity towards the free surface. This effect is quantified in Figure 3.43 where the distance from the location of the maximum mean velocity to the free surface z_m normalized by the jet exit diameter is plotted as a function of x/d for the various cases investigated. As noted earlier, for h/d=2.5 and h/d=3.5 the location of the maximum mean velocity remains on the centerline and therefore $z_m/d=h/d$. For h/d=1 and 1.5 the maximum mean velocity moves towards the free surface starting at x/d=20 and 32 respectively. Also for h/d=1 and x/d=40 the location of the maximum mean velocity is as close to the surface as it was possible to measure it.

It was also noted in the velocity profiles of the free-surface jet that the normalized mean velocity measured at the closest distance to the free surface increased with downstream distance. However, because of the normalization with the maximum velocity on the cross section this result conceals important features of the evolution of the mean velocity at the free surface. A better characterization of the mean velocity at the surface U_s is obtained when U_s is normalized by the jet exit velocity U_e. These results are presented in Figure 3.44 where U_s/U_e is plotted as a function of x/d for all values of h/d investigated. At a fixed value of h/d the mean velocity at the surface increases to a maximum value and decays further downstream. As h/d is increased the maximum value of U_s/U_e is reduced and the location of this maximum value moves downstream.

These results on the mean velocity profiles of the free-surface jet show that as the depth of the jet is increased the interaction region moves downstream, which in turn results in a reduction of the maximum mean velocity measured on the free surface. This is in general agreement with the results of the surface curvature measurements. From the point of view of the mean velocity field the interaction region can be characterized by a reduced decay rate of the maximum mean velocity a downstream displacement of the location of this

maximum and, perhaps more precisely, by a maximum of the mean velocity at the free surface.

The growth rate of the free-surface jet was characterized by the half velocity width of the mean velocity profiles in the directions perpendicular and parallel to the free surface measured from the centerline of the jet. The definition of the half velocity width is the same as the one used for the free jet and is shown schematically in Figures 3.37 and 3.41 for the direction perpendicular and parallel to the free surface respectively. The measured half velocity width normalized by the jet exit diameter are plotted as a function of x/d in Figure 3.45 for all the values of h/d considered in this study. Also plotted in this figure is a solid line representing the least squares fit to the free jet data (Figure 3.26). The half velocity width in the direction perpendicular to the surface is given by the open symbols and the width parallel to the surface is given by the solid symbols. The results show generally lower values of the half velocity width by as much as 20% compared to the free jet results. It should be noted that in this nondimensional coordinates the mean velocity results discussed above show that the interaction with the surface occurs at different locations depending on h/d. More suitable nondimensional parameters are introduced in Section IV.1 which help clarify the evolution of the half velocity width in the free-surface jet problem.

The measured rms values of the velocity fluctuation on the centerline normalized by the local maximum mean velocity are shown in Figure 3.46. Also shown in this figure is a solid line corresponding to the free jet data. Upstream of x/d=12 the results for the free-surface jet are in good agreement with the free jet data for all values of h/d. Downstream of this point the free surface jet values are lower than for the free jet. It should be noted that the uncertainty of these results increases with x/d. The uncertainty of U_{rms}/U_m at x/d=32 is estimated as ±0.05.

Profiles of the rms value of the velocity fluctuation normalized by the local maximum mean velocity for the various values of h/d are presented in Figures 3.47 to 3.53

for x/d=4, 8, 12, 16, 20, 24 and 32 respectively. Two plots are given in each figure. Plots labeled (a) are the profiles in the direction perpendicular to the free surface. Plots labeled (b) are the profiles in the direction parallel to the free surface. In each case the transverse coordinate is normalized by the corresponding half velocity width. The vertical velocity profiles are limited on the right hand side by the location of the free surface which is different for each value of h/d and for each downstream location. For $x/d \leq 12$ the shape of the rms velocity profiles in the direction parallel to the free surface, Figures 3.47(b) to 3.53(b), are in general agreement with the free jet profiles for all values of h/d. The shape of profiles in the direction perpendicular to the free surface, Figures 3.47(a) to 3.53(a), are also in general agreement with the free jet data. However it should be noted that each of the vertical profiles is abruptly terminated at the free surface. The variations along the centerline noted in regard to Figure 3.46 can also be observed in these profiles. Also increased uncertainty with downstream distance is apparent in the larger scatter of the results at the farthest distance from the jet exit. This increased scatter is also found in the free jet data.

The turbulent velocity fluctuations were further characterized by power spectrum measurements along the centerline of the jet. A typical power spectrum of the velocity fluctuation measured at x/d=8 for h/d=1 is shown in Figure 3.54. Although the spectrum is broadband, there is a fairly well defined peak at a frequency of 30 Hz. This frequency is associated with the large scale structures in the flow. The frequency for maximum power spectral density was determined as a function of downstream distance along the centerline for all values of h/d. The results are presented in Figure 3.55 in terms of the nondimensional frequency fd/U_e. Also shown in this figure is a solid line which corresponds to the free jet data. The results generally follow the free jet trend. However significant differences exists without a well defined trend which suggest that jet exit parameters are not the most appropriate scaling parameters for the free surface jet.

III.3.3 Wall Jet Results

Experiments were conducted to determine the velocity field in a wall jet. A single flow condition was investigated. The jet exit velocity was U_e=200 cm/s and the jet exit diameter was d=0.64 cm. The jet was positioned at a distance from the solid wall corresponding to h/d=1.

Figure 3.56 and 3.57 show the profiles of the local mean velocity normalized by the maximum mean velocity at each cross section measured along directions perpendicular and parallel to the solid surface respectively. The horizontal profiles in Figure 3.57 were obtained on a plane parallel to the solid surface at the distance from it where the maximum mean velocity was measured. In contrast with the free-surface jet the vertical profiles show the development of a boundary layer on the solid surface so that the maximum velocity is found at a distance from surface at all downstream locations. Note that the z coordinate in this figure is measured with respect to the solid surface. The profiles parallel to the wall have the same general shape as the free jet and free-surface jet. Although the growth rate in this case is much larger than in those other two cases as is immediately evident from these profiles. This aspect of the flow will be quantified by the half velocity width results discussed below.

The decay of the maximum mean velocity,U_m, with downstream distance for the wall jet is shown in Figure 3.58. As in other cases the parameter U_e/U_m is plotted as a function of x/d in this figure. Also shown in the figure is a solid line which corresponds to the least squares fit to the free jet data in Figure 3.25. The results for the solid wall jet are in good agreement with the results of Davis and Winarto (1980). It is apparent that downstream of x/d=15 the maximum mean velocity for the wall jet is larger than for the free jet at same downstream distance. This behaviour is similar to the free-surface jet. A detailed comparison with the free-surface jet will be presented in Section IV.3 after the proper scaling parameter for these flows are introduced.

The location of the maximum mean velocity normalized by the jet exit diameter as a function of normalized downstream distance x/d are shown in Figure 3.59. The results show a rapid displacement of the maximum mean velocity toward the surface upstream of x/d≈15 followed by an approximately linear growth of z_m/d with x/d downstream of this location. This result is also in good agreement with Davis and Winarto (1980). It should be noted that the minimum distance to the wall is found at the same downstream location where the values of U_m depart from the free jet results in Figure 3.58. Also the linear growth of z_m with downstream distance is consistent with the behaviour of three-dimensional wall jets in the far field (Launder and Rodi, 1981).

The evolution of the half velocity width normalized by the jet exit diameter is shown in Figure 3.60 for directions perpendicular (open symbols) and parallel (solid symbols) to the wall. In this case the half velocity width is measured relative to the location of the maximum velocity. Again these measurements are in good agreement with the results of Davis and Winarto (1980). It is apparent that the wall jet grows much faster in the direction parallel to the wall compared to the direction perpendicular to the wall. In the far field and at sufficiently high Reynolds number these length scales are expected to vary linearly with downstream distance (Launder and Rodi, 1981). The results show an approximately linear behaviour for L_z as a function of x with slope $dL_z/dx = 0.040$. The expected linear dependence of L_y on x is not yet found for x/d≈40. An estimate of dL_y/dx obtained from the last two points of the curve gives $dL_y/dx=0.30$. These values can be compared with the value for a free jet 0.078. Thus the growth rate in the direction perpendicular to the wall is 0.51 times the value for the free jet and the growth rate in the direction parallel to the wall is 3.9 times the free jet value. These result are in good agreement with the results of Davis and Winarto (1980) ($dL_y/dx=0.33$ and $dL_z/dx=0.036$) as well as the asymptotic values reported by Launder and Rodi (1981) in their wall jet data review for a three-dimensional wall jet ($dL_y/dx=0.26 \pm 0.02$, $dL_z/dx = 0.039 \pm 0.003$).

The downstream evolution of the rms value of the velocity fluctuation at the maximum mean velocity location normalized by the local mean velocity is shown in Figure 3.61. Also plotted in this figure is a solid line corresponding to the free jet values. Downstream of x/d≈10 the measured turbulent intensity is lower than the corresponding value for the free jet. For x/d≥20 the wall jet values are 13% lower than for the free jet. Comparison with the free surface jet data at h/d=1 (Figure 3.46) show lower values of U_{rms}/U_m for the wall jet in the region $8<x/d<20$. Downstream of x/d≈20 the turbulent intensities are similar in both cases. As noted earlier the uncertainty of these measurements at x/d≈32 is ±0.05.

The profiles of the rms value of the velocity fluctuation normalized by the maximum mean velocity at each cross section are shown in Figure 3.62 for x/d =4 and 8, and in Figure 3.63 for x/d=16,24 and 32. In each figure plot (a) represents the profiles measured along the direction perpendicular to the wall and plot (b) represents the profiles measured in the direction parallel to the wall. The profiles in the direction perpendicular to the wall are terminated for negative values of z/L_z at the wall. For x/d≤8, Figure 3.62, the measured values of turbulent intensities are comparable with values in the free jet or the free-surface jet. On the other hand in Figure 3.63 (b) for x/d≥16 the rms velocity profile in the direction parallel to the wall shows a distinct plateau for $y/L_y = \pm 2$ which is not found in the free jet or free-surface jet results. This difference in the rms velocity profile and the much larger growth rate in this direction suggest a fundamental change in the turbulent structure of this flow compared to the free jet or the free-surface jet. This aspect of the wall jet will be discussed in Section IV.3.

CHAPTER IV

DISCUSSION

Perhaps the most interesting result of this investigation is the complex pattern of surface waves and motions produced by the underwater jet on the free surface. This surface pattern is driven by the underwater flow. The flow characteristics and scaling of this underwater flow are discussed first in Section IV.1. This is followed by the discussion of the free surface phenomena in Section IV.2. Finally in Section IV.3 a comparison of the free-surface jet and the wall jet is presented and discussed.

IV.1 Mean Flow Characteristics and Scaling of the Free Surface Jet

The jet flow structure was altered by the interaction of the jet with the free surface. The downstream evolution of the maximum mean velocity presented in Figure 3.42 is different from that of the free jet. The maximum mean velocity decays at a slower rate than for the free jet. The location of the maximum mean velocity approaches the surface in the downstream direction, Figure 3.43, and eventually the maximum velocity occurs at the surface. A simple model is proposed based on dimensional reasoning and similarity concepts which describes the scaling in the far field of the free surface jet. A schematic diagram of the model is shown in Figure 4.1. In this model the free surface is assumed to be a plane of symmetry (Novikov, 1988) for the flow with a momentum flux twice the momentum flux, J_o, of the corresponding free jet. It is further assumed that the dominant length scale is h the distance from the jet centerline to the free surface. The jet exit diameter plays an indirect role through its effect on the jet momentum J_o.

The similarity scaling in the far field of the turbulent axisymmetric jet has been discussed by several authors (e.g., Rajaratnam 1976, Tennekes and Lumley 1972 and Townsend 1956). If the jet momentum flux is constant, the linear growth of length scales with downstream distance implies that sufficiently far downstream compared to the jet exit diameter the mean centerline velocity, U_m, can be written as:

$$\sqrt{\frac{J_o}{\rho_o}}\ \frac{1}{U_m} = c_1(x - x_o) \qquad \text{(IV.1)}$$

where ρ_o is the fluid density and c_1, x_o are constants determined experimentally. In this investigation the value of c_1=0.162 was found for the free jet, (Figure 3.25). It follows that for the free surface jet at sufficiently large distance compared to the jet depth h, the maximum velocity U_m is given by

$$\sqrt{\frac{2J_o}{\rho_o}}\ \frac{1}{U_m} = c_1(x - x_o) \qquad \text{(IV.2)}$$

where the factor 2 is needed to account for the momentum of the image jet above the surface. The constant c_1 should be the same as for the free jet while the value of x_o depends on the geometry of the jet and consequently can not be expected to be the same as for the free jet.

Equation IV.2 can be written as

$$\frac{U_e\, d}{U_m\, h} = \frac{c_1}{\sqrt{2}}\left(\frac{x}{h} - \frac{x_o}{h}\right) \qquad \text{(IV.3)}$$

This equation is based on the assumption that J_o is a constant independent of x. As discussed by Kotsovinos (1976,1978) this fails to account for the momentum flux of the entrained fluid which tends to reduce the momentum flux as the flow evolves downstream. Also in the free-surface jet problem, surface waves generated at the interaction will carry momentum away from the jet which if sufficiently large will result in a lower effective value of J_o. Also the presence of surface active agents may contribute to a reduced

momentum flux. Not withstanding these observations the similarity argument suggests that: (i) the proper velocity scale for the free-surface axisymmetric jet in the far field is $U_e d/h$; (ii) the proper length scale is h the depth of the jet; and (iii) the maximum mean velocity is found at the free surface.

Figure 4.2 is a plot of $U_e d/U_m h$ as a function of x/h for all the free-surface jet data (h/d=1, 1.5, 2.5 and 3.5). It is apparent that the proposed similarity scaling results in good collapse of the data shown in Figure 3.42. The results for $x/h \geq 15$ seem to follow a straight line. A least squares fit to these data gives a slope of 0.099. This value is somewhat lower (14%) than the value calculated from $c_1/\sqrt{2} = 0.115$ using $c_1=0.162$ the value for the free jet. This result is somewhat striking since from the arguments presented above the various processes that can invalidate the assumption of constant momentum flux J_o will result in the reduction of momentum flux and consequently an increase of the slope of $U_e d/U_m h$ vs. x/h.

To further examine this question the mean velocity similarity profiles for various values of x/h are presented in Figures 4.3 and 4.4. In each figure, plot (a) presents the similarity profiles in the direction normal to the free surface and plot (b) presents the profiles parallel to the free surface. For a normalized distance of $x/h \approx 12$, Figure 4.3(a) shows a significant reduction of the mean velocity close to the free surface (the free surface is located at $z/L_z \approx 1$). Clearly this velocity profile is not consistent with the assumptions used to derive equation IV.3. Note that $x/h \approx 12$ is where the maximum mean velocity for the free-surface jet begins to deviate from the free jet line. Farther downstream at x/h=24 and 32 the mean velocity similarity profiles are given in Figure 4.4. The similarity profile in the direction perpendicular to the surface, Figure 4.4(a), at x/h=24 still shows the maximum velocity away from the surface. At x/h=32 the maximum occurs closer to the free surface. It follows that the scaling given by equation IV.3 can only be expected to be valid downstream of x/h=32. If in Figure 4.2 the last two points are used to estimate the

slope of $U_e d/U_m h$ vs. x/h the result is 0.114. This value is in good agreement with the value derived from the free jet result $c_1/\sqrt{2} = 0.115$.

The growth rate of the mean velocity profile were characterized by the half velocity width L_y and L_z in the direction parallel and perpendicular to the free surface. This half velocity width were determined with reference to the jet centerline. The arguments presented above suggest that while this definition is adequate for the direction parallel to the free surface, a more appropriate length scale in the direction perpendicular to the surface is the half velocity width measured from the free surface L'_z. The normalized half velocity widths L_y/h and L'_z/h are plotted in Figure 4.5 as a function of x/h for all values of h/d. The values of L'_z/h (open symbols) are along a line parallel to the L_y/h data but displaced by 1. This is simply a manifestation of the fact that because of the displacement of the centerline with respect to the free surface the jet cross section is enlarged with major axis in the direction perpendicular to the free surface. Both L_y and L'_z grow approximately linearly with x. The growth rates dL_y/dx and dL'_z/dx are very close to the value for the free jet. However for $x/h \geq 32$ the values of L_y and L'_z seem to converge toward each other.

It is interesting to note that the values of L_y and L'_z show small yet systematic deviations from the linear growth. For h/d=1 the difference $(L'_z - L_y)$ is smaller at $x/h \approx 12$ to 16, increases for $x/h \approx 20$ and 24 and decreases again for $x/h \geq 32$. A plausible explanation for this phenomenon is the change in the eccentricity of the jet cross section during its interaction with the free surface. A similar phenomenon has been reported by Ho and Gutmark (1985) for the growth rate of an elliptic jet. Axis switching between the major and minor axes occurred in the range of $x/d \leq 40$ due to the self-induction of the large scale vortical structures in the flow. Also the vortex ring experiments of Bernal and Kwon (1989) show an oscillation of the ring eccentricity during the interaction with a free surface.

The downstream evolution of the rms value of the velocity fluctuation normalized by the local mean velocity at the interaction point is shown in Figure 4.6. In this figure $U_e d/U_{rms} h$ is plotted as a function of x/h. This scaling was used because it reduces the

uncertainty of the results. The straight line in this plot represents the free jet case. Although the uncertainty in the measurements of U_{rms} at x/h=32 is rather large, there is an indication of a change in the slope of the curve compared to the free jet downstream of the point x/h=24. This point is far downstream of the point, x/h≈11 on Figure 4.2, for which the maximum mean velocity starts to deviate from the free jet behavior.

The frequency for maximum spectral energy on the jet centerline normalized with the proper free-surface jet scaling parameters, $fh^2/U_e d$, is plotted as a function of x/h in Figure 4.7 for all values of h/d. These normalization provides good collapse of the data even for values of x/h<10. Also shown in this figure is a straight line with slope -2 corresponding to the expected dependence of this frequency on x ($f \propto x^{-2}$).

The downstream evolution of the normalized mean surface velocity along the jet centerline, measured at a distance of approximately 2 mm below the surface, is shown in Figure 4.8. The mean surface velocity is very small for $x/h \leq 5$. The mean surface velocity reaches a maximum at x/h≈11 and decreases downstream of this point. The solid line in this plot represents a least squares curve fit through the normalized maximum mean velocity data presented in Figure 4.2. From Figure 4.8 it can be seen that the rate of decay of the surface velocity approaches the value for the maximum mean velocity in the downstream direction. It is rather interesting to note that the rate of decay of surface velocity is much slower than its initial rate of increase in the axial direction. Also from the point of view of velocity field the location of the maximum interaction point can be defined as x/h≈11.

IV.2 Surface Waves and Surface Motions

One of the main objectives of this investigation was to gain some understanding on the nature of the free surface motions caused by the interaction of turbulence in the underwater jet with the free surface. One of the important aspects of this interaction is the generation of the surface waves. These waves are produced by the large scale vortical

motion moving underneath and approaching the surface, initially deforming it and eventually 'breaking' the surface. The series of events leading to generation of surface waves observed on the motion pictures of the flow are illustrated in Figures 3.3 to 3.8. Additional evidence can be found in the results presented in Figures 4.9, 4.10 and Table 4.1. In Figure 4.9 the normalized frequency of the peak power spectral density of the surface deformation measured on the centerline (open symbols) and of the centerline velocity fluctuations (solid symbols) are plotted as functions of x/h for two typical conditions. Figure 4.10 is the plot of the normalized rms amplitude of the surface curvature plotted as a function of x/h for several flow conditions. Of course x/h is the proper normalization for this flow as shown above.

It is apparent from Figure 4.9 that the surface waves are initially produced with a frequency that corresponds to the underwater large scale motion at x/h≈5. At this point the mean surface velocity is very small as shown by Figure 4.8 while the surface curvature results in Figure 4.10 indicate significant amplitude of the surface deformation. It follows that this initial surface deformation is produced before the underwater vortical flow has reached the surface. This type of interaction has been investigated by Tryggvason and Wu (1988,1989).

Farther downstream (5< x/h <12) the frequency of the surface curvature fluctuations remains approximately constant while the frequency of the velocity fluctuations decreases. This result implies that the surface deformation is dominated by waves generated upstream propagating into this region. In this region the amplitude of the surface deformation increases and then decreases as shown in Figure 4.10. The normalized frequency at the maximum interaction point, $f_s h^2/U_e d$ and the location of the maximum interaction point, x_m/h, determined from the surface curvature results are given in Table 4.1. Also important in this region is the observation in Figure 4.8 that the surface velocity increases to a maximum and then decreases. Thus the waves propagating along the centerplane encounter an increase in the surface mean velocity followed by a reduction of

the surface mean velocity. This acceleration and deceleration of the surface flow implies straining of the surface.

In the absence of a mean surface deformation

$$\frac{\partial U_s}{\partial x} + \frac{\partial V_s}{\partial y} = 0 \qquad \text{(IV.4)}$$

Therefore in the region corresponding to $5<x/h<11$ on Figure 4.8, for which the surface flow is accelerating, $\partial U_s/\partial x>0$, there is stretching of the surface in the axial direction and contraction of the surface in the lateral direction. Farther downstream when the surface flow decelerates, $\partial U_s/\partial x<0$, there is contraction of the surface in the axial direction and stretching of the surface in the lateral direction.

The effect of the surface currents on the waves have been studied by Evans (1955), Taylor (1955), Hughes and Stewart (1961), Longuet-Higgins and Stewart (1961), Taylor (1962) and Peregrine (1976). Some of their results are summarized by Phillips (1966). They found that when waves propagate over a surface with non-uniform currents, the waves undergo changes in wavelength, amplitude and direction. The effect of increased surface velocity on the waves can be observed on Figure 3.5. The distance between the wave crests increases along the jet centerline. Also there is an indication of a decrease in the curvature of the crests and wave amplitude along this direction. It is proposed that surface straining prevents the propagation and generation of surface waves on the centerline region of the jet downstream of $x/h \approx 11$.

Farther downstream for $x/h > 11$, Figure 4.9 indicates that the surface curvature fluctuations occur at the same frequency as the underwater flow field. In this region then the surface motion follows the fluctuations of the underwater turbulence. The amplitude of the fluctuations monotonically decreases with downstream distance. A conspicuous feature of the interaction of the vortical structures with the surface are the dark spots associated with the vortex lines terminating at the free surface. Since the fluid at the free surface is initially irrotational, vorticity at the free surface must be the result of the interaction of the

vortical flow under the surface with the free surface. Figure 3.3 represents a typical photograph of this interaction, in which underwater vortex lines in the near field of the jet opens at the free surface. This type of interaction is important because not only imparts momentum to the surface but also because of the associated mass transport. These flow processes in the simpler case of a vortex ring have been investigated by Bernal and Kwon (1989) and Kwon (1989).

The waves generated by the underwater flow also propagate away from the centerline. The frequency of the waves obtained from the surface curvature measurements is approximately the same as the frequency obtained at the point of maximum rms surface curvature fluctuation along the jet centerline as shown by the results tabulated in Table 4.1. The fundamental frequency in the wave region, f_w, and at the point of maximum interaction, f_s, were obtained from the power spectrum of the surface curvature data. The results for various jet exit velocities and depths tabulated in Table 4.1 show good agreement between these two frequencies. The wavelength of the waves was calculated using the dispersion relation for the deep water waves with surface tension as well as gravity taken into account (Lighthill, 1978). The wavelengths obtained were approximately 1-7 cm in the capillary-gravity range. The Strouhal number corresponding to the cases for which the waves were generated in the near field of the jet was calculated to be $St = f_w\, d/U_e = 0.38$. This value of the Strouhal number falls within the range of St=0.24-0.64 corresponding to the preferred modes for jets reported in literature. (Gutmark and Ho, 1983). As the jet depth is increased the Strouhal number defined as $St=f_w\, h^2/U_e d$ is more appropriate. The values of this Strouhal number are given in Table 4.1. They are also within the same range of values as the preferred mode of the jet.

The propagation characteristics of the waves show a number of interesting features. The flow visualization and frequency results discussed earlier show that the waves are initially generated by the large scale vortical structures in the flow before they reached the free surface. It follows that the direction of propagation of the waves is determined by the

ratio of the advection speed of the large scale vortical structures in the flow to the speed of propagation of surface waves at the passage frequency of the large scale motion at the beginning of the interaction region (x/h≈5). Thus for a fixed depth, as the jet momentum is increased by increasing the jet exit velocity for example, the advection velocity of the large scale structures is increased which also results in an increase of the passage frequency of the large scale structures since the interaction region does not move in space. Consequently, for values of h larger than 1.74 cm which results in surface waves on the right side of the minimum of the dispersion relation, the effect of increase momentum is to reduce the wave speed. This results in an increase of the propagation angle relative to the downstream direction. These arguments are consistent with the flow visualization results of Section III.1 which shows a wave propagation angle of approximately 60 degrees for U_e = 50 cm/s and h/d=1 compared to 39 degrees for U_e=35 cm/s and h/d=1. The results of the surface curvature measurements (Figures 3.11 to 3.16) also show a steepening of the waves propagation angle with strength of the interaction.

The measurements of the surface curvature show an increase followed by a reduction of the amplitude of the surface curvature fluctuations with downstream distance (Figure 3.17 to 3.19 and 4.10). As the 'strength' of the interaction is increased, say by increasing the jet exit velocity keeping the other parameters constant, the maximum normalized value of the rms surface curvature fluctuation, V_{rms}/V_L, increases in magnitude. The location of this maximum x_m moves downstream. These changes are documented in Figures 4.11 and 4.12 for the maximum value of V_{rms}/V_L and x_m/h respectively. In both figures the strength of the interaction is characterized by the nondimensional parameter $U_e d/U_w h$ where $U_e d/h$ is the characteristic velocity scale for the free-surface jet and U_w is the minimum dispersion velocity of capillary-gravity waves. The relevance of U_w arises because at the conditions of the experiments reported here both capillary and gravity effects are important in the dynamics of the surface waves and motions. The results in Figure 4.11 show the increase in V_{rms}/V_L to be approximately like $(U_e d/U_w h)^2$. The downstream

displacement of the location of the maximum interaction point reaches $x_m/h=10$ for $U_e d/U_w h \approx 5.5$. It appears that x_m/h may not increase beyond $x/h=11$ where the maximum surface velocity is found.

IV.3 Comparisons of a Free-Surface Jet with a Wall Jet

Rajaratnam and Humphries (1984) noted similarities between the free-surface jet results and the wall jet results. Also in the wall jet literature (see for example the reviews by Launder and Rodi 1981, 1983) it is frequently argued that the apparent linear growth of $1/U_m$ with downstream distance is an indication of negligible skin friction at the wall. This scaling is confirmed by the detailed measurements of Davis and Winarto (1980) who found a rate of decay very similar to a free jet. If in fact the skin friction is negligible it follows that the free-surface jet and wall jet are indeed very similar and Rajaratnam and Humphries comparisons are justified. On the other hand, there are reasons to believe that these flow fields are not that similar based on vorticity dynamics at a free surface compared to a solid surface as noted in the introduction.

To address these issues the scaling arguments presented in Section IV.1 can be reworked for the wall jet. Figure 4.13 is a schematic diagram of the flow field for the wall jet which incorporates the image jet to the other side of the wall. The more important difference in comparison with the free-surface jet diagram in Figure 4.1 is the effect of skin friction at the wall τ_w which results in a reduction of the velocity to zero at the wall. Following the similarity argument, i.e. length scales increase linearly with downstream distance, x, equation IV.1 can be written as

$$\sqrt{\frac{J}{\rho_o}}\ \frac{1}{U_m} = c_1(x - x_o) \qquad \text{(IV.4)}$$

where c_1 is determined by the shape of the similarity velocity profiles and the growth rate of length scales in the flow. In this case the momentum flux J at a downstream station will

have to incorporate the excess momentum flux associated with confinement of the jet by the wall which is characterized by the image momentum flux J_o, as well as the reduction due to skin friction at the wall τ_w. Thus, the momentum flux at x, J, can be written as

$$J = 2J_o - 2 \int_0^x dx \int_{-\infty}^{\infty} \tau_w \, dy \qquad \text{(IV.5)}$$

It follows from these arguments that, if changes in the constant c_1 are neglected, the ratio of the slope of $1/U_m$ versus downstream distance x between the free jet and wall jet is given by $(J_o/J)^{1/2}$. If τ_w can be neglected as in the free-surface jet then $J=2J_o$ and the slope of $1/U_m$ is reduced by a factor of $(1/2)^{1/2}$ as already documented in Section IV.1. The effect of τ_w is to increase the slope of $1/U_m$ versus x. As the flow develops downstream the slope will increase as friction at the wall continuously reduce the momentum flux. It should be noted that at the downstream location where

$$J_o = 2 \int_0^x dx \int_{-\infty}^{\infty} \tau_w \, dy$$

the slope of $1/U_m$ will be equal to the slope for a free jet. Therefore the fact that the slope of $1/U_m$ is close to the value for a free jet should <u>not</u> be construed to indicate that the skin friction is negligible but to the contrary it may be an indication that it is large enough to balance the extra J_o due to the confinement of the jet. Although the local skin friction may be small compared to the local dynamic pressure, i.e $C_f<<1$ (Launder and Rodi, 1981), the integrated effect over the surface is the dynamically important parameter which can be expected to be of the order of J_o at some distance from the jet exit.

The assumption that c_1 is a constant may not be an accurate assumption for the wall jet. Two effects must be taken into account. First, the boundary layer on the wall results in a reduced momentum flux associated with the similarity velocity profiles. The effect of this reduced momentum flux is to lower the value of the constant c_1 for the wall jet and consequently to reduce the decay rate of U_m. Second, the different growth rates dL_y/dx and dL_z/dx of the wall jet compared to a free jet will also change the value of the constant

c_1. The results in Figure 3.60 indicate a much larger value of dL_y/dx and reduced value of dL_z/dx compared to the free jet. It is easily shown that

$$c_1 \propto \left(\frac{dL_y}{dx}\ \frac{dL_z}{dx}\right)^{1/2}$$

For the wall jet the effect of the growth rate length scales is to increase the value of the constant c_1 compared to the free jet. This implies a faster decay of U_m with downstream distance.

A second consequence of these scaling arguments is that the characteristic velocity scale for the wall jet is $U_e d/h$ and the characteristic length scale for the wall jet is h, the same as for the free-surface jet. Therefore direct comparisons can be made between the free-surface jet results and the wall jet results at h/d=1 to test these ideas.

Figure 4.14 is a plot of $U_e d/U_m h$ as a function of x/h for the wall jet, solid symbols, and the free-surface jet, open symbols. Also shown in this plot is a solid line which corresponds to the free jet data. For $8<x/h<30$ the maximum velocity for the wall jet is larger than for the free-surface jet. This is consistent with the observation that, although the image effect (confinement) is present in both cases, the velocity profiles for the wall jet must be zero at the wall resulting in less momentum flux which must be balanced by an excess centerline velocity. Farther downstream, x/h≈24, the slope of the wall jet data is greater than for the free-surface jet.

Comparison between the growth rate of the free-surface jet and the wall jet is presented in Figure 4.15. In this figure the normalized half velocity width for the free-surface jet was measured from the jet exit centerline. The wall jet half-velocity width was measured from the location of the maximum mean velocity. The solid line in Figure 4.15 is a least squares fit to the half velocity width data for the free jet. The growth rate of the free jet and the free-surface jet are very similar up to x/h≈32. In contrast the wall jet growth rate is much larger in the direction parallel to the surface (solid symbols) compared to the direction perpendicular to the wall. The wall jet growth rate in the transverse direction is

approximately 3.9 times higher that of the free jet. The growth rate in the vertical plane is 0.51 times the growth rate for the free jet. These results for the wall jet are in good agreement with the results of Davis and Winarto (1980). The mean growth rates of the free-surface jet have not changed as a result of the interaction with the free surface. This result is somewhat different from the growth rate results obtained by Rajaratnam and Humphries(1984). They found that the growth rate in the vertical direction is approximately the same as for the wall jet and the growth rate in the transverse direction is approximately half the value for the wall jet.

Significant differences between the wall jet results and the free-surface jet results also are found in the location of the maximum mean velocity. Figure 4.16 is a plot of the normalized distance to the wall or to the free surface of the maximum mean velocity as a function of x/h. In the wall jet case the displacement of the maximum mean velocity occurs much closer to the wall (x/h<20) than for the free-surface jet. In the far field, it is expected that for the wall jet z_m will continue the linear growth with x while, for the free-surface jet z_m is expected to be zero.

The difference in the growth rate between the wall jet and the free-surface jet is very significant and is consistent with the different dynamics of vorticity at a free surface compared to a solid wall. In the case of the free-surface jet the interaction of the vortical underwater flow with the free surface results in vortex lines terminating at the free surface as shown by the flow pictures. These vortex lines remain perpendicular to the main flow direction. In contrast, for the wall jet vortex lines can not terminate at the solid wall, where the normal component of the vorticity vector must be zero, and must rearrange to become parallel to the solid surface. This suggests the existence in the wall jet problem of a strong secondary flow on cross-sectional planes as first discussed by Launder and Rodi (1981). This secondary flow produces outward (away from the center plane) flow near the wall and inward flow at a distance from the wall. The pronounced shoulder of the measured

turbulent intensity profiles shown in Figure 3.63 (b) can be attributed to the presence of such secondary flow.

CHAPTER V

CONCLUSIONS

An experimental investigation of the interaction of a submerged turbulent round jet with the free surface was conducted. Flow visualization, surface curvature measurements and hot film velocity measurements were performed to study this problem. The results of the free-surface jet experiments were compared with the results of a wall jet experiment. A summary of the main conclusions of this investigation is presented below:

- Surface waves are produced as a result of the deformation of the surface caused by the vortical structures in the jet moving underneath the surface. The surface waves propagate at an angle to the downstream direction. Propagation in the downstream direction is suppressed by the surface currents produced by the jet flow.

- In the far field surface motions are driven by the local underwater turbulent eddies directly interacting with the surface. Vortex lines terminating at the free surface are a common occurrence in this region.

- The scaling parameters for the free-surface jet were determined. They are the jet depth, h, and the characteristic velocity at the interaction $U_e d/h$. The decay rate of maximum mean velocity in the far field is reduced by a factor of $2^{1/2}$ compared to the free jet. The mean growth rate of the free-surface jet is approximately the same as the free jet.

- The interaction of the jet with the solid wall results in a fundamentally different flow field compared to the free-surface jet case. There is a higher growth rate in the direction parallel to the solid surface and a lower growth rate in the direction perpendicular to the surface. This is a consequence of different vorticity dynamics at a solid wall which results in the development of a strong secondary flow. Also the maximum mean velocity decays at a higher rate compared to the free-surface jet. This is a consequence of the reduced momentum flux of the wall jet due to skin friction at the wall as well as the increased growth rate.

ACKNOWLEDGMENTS

We wish to thank our colleagues at Michigan for numerous helpful discussions during the course of this investigation, in particular Professors R.F. Beck, J.F. Driscoll, A.F. Messiter and W.W. Willmarth. This research was sponsored by the Office of Naval Research, Contract no. N000184-86-K-0684 under the U.R.I. Program for Ship Hydrodynamics.

APPENDIX A

ANALYSIS OF SURFACE CURVATURE MEASUREMENTS

A.1 Analysis

Visualization and quantitative measurements of the surface deformation was obtained by positioning a photographic plate or a photodiode above and close to the water surface illuminated from below by a collimated beam of light. The collimated beam is altered by refraction at the water/air interface. Local depression and elevation of the free surface has a lens-like effect on the light rays, with depression of the surface acting as a diverging lens and elevation of the surface as a converging lens. The following paragraphs describe the relation between the light intensity measured by the photodiode or recorded on the photographic film and the shape of the surface.

We consider a two dimensional surface deformation as indicated in Figure A.1, and use geometrical optics to analyze this optical system. The incoming light beam has intensity I_o. The deformed water surface is described by the distance $\eta(x)$ to the undisturbed (mean) surface. The photodiode or photographic plate is located a distance s to the undisturbed water surface.

We consider a ray of light that intersects the surface at x. We wish to determine the location, x', where the ray will intersect the film or photodiode plane. From the geometry of the system we find:

$$x' = x + (s - \eta) \tan\theta_d \qquad (A.1)$$

In order to determine the deflection angle θ_d we apply the law of refraction:

$$\theta_d = \theta_r - \theta_i \qquad (A.2)$$

where $\theta_i = \alpha$ with $\tan\alpha = d\eta/dx = \eta'(x)$. The refraction angle θ_r is given by:

$$n_a \sin\theta_r = n_w \sin\theta_i \tag{A.3}$$

where n_a and n_w are the indicies of refraction of air and water respectively. Then:

$$\sin\theta_r = N \sin\theta_i = N \frac{\tan\theta_i}{\sqrt{1 + \tan^2\theta_i}} \tag{A.4}$$

with $N = n_w / n_a$. It follows:

$$\tan\theta_r = \frac{N \tan\theta_i}{\sqrt{1 - (N^2-1)\tan^2\theta_i}} \tag{A.5}$$

also:

$$\tan\theta_i = \eta' \tag{A.6}$$

then:

$$\tan\theta_r = \frac{N\eta'}{\sqrt{1 - (N^2-1)\,\eta'^2}} \tag{A.7}$$

Note that $\eta' \leq 1/(N^2-1)^{1/2}$. The equal sign corresponds to the total reflection condition. Thus one can obtain the relationship:

$$\tan\theta_d = \eta'(x) \left\{ \frac{N - \sqrt{1 - (N^2-1)\eta'^2}}{\sqrt{1 - (N^2-1)\eta'^2} + N\eta'^2} \right\} \tag{A.8}$$

and:

$$x' = x + \{s - \eta(x)\}\, \eta'(x)\, H(x) \tag{A.9}$$

$$H(x) = \frac{N - \sqrt{1 - (N^2-1)\eta'^2}}{\sqrt{1 - (N^2-1)\eta'^2} + N\eta'^2} \tag{A.10}$$

The amount of light reaching the photographic film or photodiode in a small surface element dx' at location x' is given by:

$$I(x')\, dx' = I_0\, dx \tag{A.11}$$

where dx is the region in the incident beam where all rays going through dx' pass. Therefore:

$$\frac{I(x')}{I_o} = \left|\frac{dx}{dx'}\right| \qquad (A.12)$$

where the absolute value sign was added since both $I(x')$ and I_o are always positive.

A.2 Physical Interpretation

Equations (A.1) and (A.12) provide a simple description of this optical system. A plot of the location of the light ray on the image plane, x', against its corresponding location, x, on the water surface is shown in Figure A.2. The straight line in this Figure has slope unity and corresponds to an undisturbed water surface. If there is a disturbance on the surface the second term in the equation (A.1) also contributes and adds a deformation to the straight line shown in Figure A.2. The solid curve on Figure A.2 represents the case of small amplitude sinusoidal disturbances of the surface. In this case the slope dx'/dx is always positive and x is a single-valued function of x'.

As the amplitude of the disturbance is increased the second term in the equation can result in a negative slope of x' versus x in certain regions as shown in Figure A.2 by the dotted curve. In this case x is no longer a single-valued function of x', i.e. light rays from two or more points in the object/incoming beam pass through the same point in the image plane. This corresponds to focussing of the incoming beam to a point. Furthermore, in this case there are points for which $dx'/dx = 0$. At these points according to equation (A.12) the light intensity becomes very large. These points form characteristic bright lines or caustics in the images obtained using this technique.

A.3 Practical Considerations

In order to obtain quantitative data using this technique the formation of caustics and focussing must be avoided. For a given surface deformation these effects can be minimized by reducing the distance s from the water surface to the image plane. However,

for sufficiently large deformations of the surface the formation of caustics and focussing may not be avoided.

In the limit of small surface deformations $\eta << s$ and $\eta'(x) << 1$ we can linearize equations (A.9) and (A.10) to obtain:

$$x' = x + s\,\eta'(x)\,(N-1) + \cdots \tag{A.13}$$

and using equation (A.12) one obtains:

$$\frac{I(x')}{I_o} = \left|\frac{dx}{dx'}\right| = \frac{1}{1 + s\,\eta''(x)\,(N-1) + \cdots} \tag{A.14}$$

i.e.

$$\frac{I(x')}{I_o} = 1 - s\,(N-1)\,\eta''(x) \tag{A.15}$$

Thus, the intensity at the measurement plane contains a fluctuating component proportional to the second derivative of the surface deformation. This is the motivation to use the phrase "surface curvature measurements". Note also that in regions where $\eta(x)$ is a maximum $\eta''(x) < 0$ and $I(x')$ will be larger than I_o resulting in a bright region, and where $\eta(x)$ is a minimum $I(x')$ is smaller than I_o resulting in a dark region.

REFERENCES

Abramovitz, G.N. (1963) The theory of turbulent jets, M.I.T. Press,Cambridge,Mass.

Batchelor G.K. (1967) An introduction to fluid dynamics, Cambridge University Press

Bernal, L.P. and Kwon, J.T. (1989) "Vortex ring dynamics at a free surface", Physics of Fluids, A1 (3), 449-451

Berry, M.V. and Hajnal, J.V. (1983) "The shadows of floating objects and dissipating vortices", Optica Acta, Vol. 30, No. 1, 23-40.

Bradshaw, P., Ferriss, D.H. and Johnson, R.F. (1964) "Turbulence in the noise-producing region of a circular jet" J. Fluid Mech., Vol. 19, Part 4, 591-625.

Browand, F.K. and Laufer, J. (1975) "The role of large scale structures in the initial development of circular jets", Proc. 4th Symp. on Turbulence in Liquids, University of Missouri-Rolla, edited by Zakin, J.L., Patterson, G.K.

Chandrasekhar Swamy, N.V. and Bandyopadhyay, P., (1975) "Mean and turbulence characteristics of three-dimensional wall jets", J. Fluid Mech., Vol. 71, 541.

Davis, M.R. and Winarto, H. (1980) "Jet diffusion from a circular nozzle above a solid plane", J. Fluid Mech., Vol. 101, Part 1, 201-221.

Dimotakis, P.E., Maike-Lye, R.C. and Papantoniou, D.A. (1983) "Structures and dynamics of round turbulent jets", Physics of Fluids, Vol. 26, No.11,3185-3192.

Evans, J.T. (1955) "Pneumatic and similar breakwaters", Proc. Royal Society A, 231,457-466.

Gutmark, E. and Ho, Chih-Ming (1983) "Preferred modes and spreading rates of jets", Physics of Fluids, Vol. 26, No.10, 2932-2938.

Hughes, B.A. and Stewart R.W. (1961)"Interaction between gravity waves and shear flow", J. Fluid Mech., Vol.10,Part 3, 385-400.

Kotsovinos, N.E. (1976), "A note on the spreading rate and virtual origin of a plane turbulent jet", J. Fluid Mech., Vol. 77, 305-311

Kotsovinos, N.E. (1978), "A note on the conservation of the axial momentum of a turbulent jet", J. Fluid Mech., Vol. 87, 55-63.

Kwon, J.T. (1989) "Experimental study of vortex ring interaction with a free surface", Ph.D. Thesis, University of Michigan.

Launder, B.E. and Rodi, W. (1981) " The turbulent wall jet", Prog. Aerospace Sci., Vol.19, pp. 81-128.

Launder, B.E. and Rodi, W. (1983) "The turbulent wall jet - Measurements and modeling, Annual Review of Fluid Mechanics , Vol. 15.

Lighthill, J. (1978) Waves in Fluids, Cambridge University Press.

Longuet-Higgins, M.S. and Stewart, R.W. (1961)"The changes in amplitude of short gravity waves on steady non-uniform currents", J. Fluid Mech., Vol.10, Part 4, 529-549.

Munk, W.H., Scully-Power, P. and Zachariasen, F. (1987) "THE BAKERIAN LECTURE 1986: Ships from space," Proc. Royal Society A, Vol. 412, 231-254.

Newman, B.G., Patel, R.P., Savage, S.B. and Tjio, H.K. (1972),"Three dimensional wall jet originating from a circular orifice", Aero. Quart., 23, 188-200

Novikov, E.A. (1988) "Generation of surface waves by three-dimensional vortex structures", Physics Letters A, Vol.130, No.3.

Peregrine, D.H. (1976) "Interaction of water waves and currents", Advances in Applied Mechanics, Vol.16, 9-117.

Phillips, O.M.(1966) The dynamics of the upper ocean, Cambridge University Press.

Rajaratnam, N. and Pani, B.S. (1974) "Three dimensional turbulent wall jets", Proc. ASCE, J. Hyd. Div., Vol. 100, 69-83.

Rajaratnam, N. (1976) Turbulent Jets, Elsevier Scientific Publishing Company.

Rajaratnam, N. and Humphries, J.A. (1984) "Turbulent non-buoyant surface jets", J. of Hydraulic Research, Vol. 22, No.2, 103-115.

Ramberg, S.E., Swean, T.F., Plesnia, M.W. (1989) "Turbulence near a free surface in a plane jet", Naval Research Laboratory Memorandum Report 6367.

Ricou, F.P. and Spalding, D.B. (1961) "Measurements of entrainment by axisymmetrical turbulent jets", J. Fluid Mech., Vol. 11, 21-32.

Schlichting, H. (1955) Boundary Layer Theory, McGraw-Hill, New York.

Schneider, W. (1985) " Decay of momentum flux in submerged jets", J. Fluid Mech., Vol. 154, 91-110.

Sforza, M.P. and Herbst, G. (1970), "A study of three-dimensional, incompressible turbulent wall jets.", AIAA J., 8, 276.

Sterling, M.H., Gorman,M., Widmann, P.J., Coffman, S.C., Strozier, J. and Kiehn, R.M. (1987) "Why are these disks dark? The optics of Rankine vortices", Physics of Fluids, Vol. 30, No. 11, 3624-3626.

Taylor, G.I. (1955) "The action of a surface current used as a breakwater", Proc. Royal Soc. A, 231, 466-478.

Tennekes, H. and Lumley, J.L. (1972) The first course in turbulence, MIT Press, Cambridge, Massachusetts.

Townsend, A.A., (1956) The structure of turbulent shear flow, Cambridge University Press.

Tryggvason, G., (1988) "Deformation of a free surface as a result of vortical flows", Physics of Fluids, Vol. 31, 955-957.

Tso, J., Kovasznay, L.S.G. and Hussain, A.K.M.F. (1981) "Search for large scale coherent structures in the nearly self-preserving region of a turbulent axisymmetric jet", Transactions of ASME, J. Fluid Engr., Vol. 103, 503-508.

Willmarth,W.W. (1977) "The effect of cross flow and isolated roughness elements on the boundary layer and wall pressure fluctuation on circular cylinders", The University of Michigan Dept. of Aerospace Engr. Report # 014439-01, 4.

Wygnanski, I. and Fiedler, H.E. (1969) "Some measurements in the self-preserving jet", J. Fluid Mech., 38, Part 3, 577-612.

Yule, A.J. (1978) "Large-scale structure in the mixing layer of a round jet", J. Fluid Mech., Vol. 89, No.3, 413-432.

TABLES

Jet Exit Diame (cm)	Length (cm)	Width (cm)	Height (cm)	Nozzle Radius (cm)	Nozzle Length (cm)
0.64	76.20	53.34	30.48	1.27	1.27
1.27	50.80	29.20	19.05	1.27	1.27
2.54	76.20	53.34	30.48	2.54	2.54

Table 2.1 - Geometrical characteristics of the jet tanks

d (cm)	U_e (cm)	δ_1 (mm)	θ (mm)	$Re_{\delta 1}$
0.64	50.0	0.133	0.051	255
0.64	100.0	0.094	0.036	360
0.64	150.0	0.077	0.030	450
0.64	200.0	0.066	0.026	513
1.27	50.0	0.154	0.059	295
1.27	100.0	0.109	0.042	420
1.27	150.0	0.089	0.034	510
2.54	10.0	0.487	0.188	188
2.54	25.0	0.308	0.119	297
2.54	30.0	0.281	0.108	324
2.54	35.0	0.261	0.101	353
2.54	50.0	0.218	0.084	420

Table 2.2 - Characteristics of the free shear layer at the jet exit

U_e (cm/s)	h/d	d (cm)	x_m/h	$f_s h^2/U_e d$	$f_w h^2/U_e d$	x_w/d	y_w/d	$\frac{U_e d}{U_w h}$
50	1.0	0.64	4.0	0.38	0.38	12.0	8.0	2.16
50	1.0	1.27	8.0	0.38	0.38	12.0	6.0	2.16
100	1.5	1.27	6.67	0.29	0.29	16.0	8.0	2.87
100	2.5	1.27	5.20	0.40	0.48	16.0	6.0	1.72
100	2.5	0.64	4.80	0.40	0.40	32.0	12.0	1.72
100	3.5	0.64	5.71	0.47	0.50	32.0	12.0	1.23
150	2.5	0.64	6.40	0.27	0.27	32.0	12.0	2.59
150	3.5	0.64	6.86	0.42	0.42	28.0	12.0	1.85
200	2.5	0.64	8.0	0.24	0.20	32.0	12.0	3.45
200	3.5	0.64	6.86	0.31	0.31	24.0	12.0	2.46

Table 4.1 - Summary of Surface motion and wave data

FIGURES

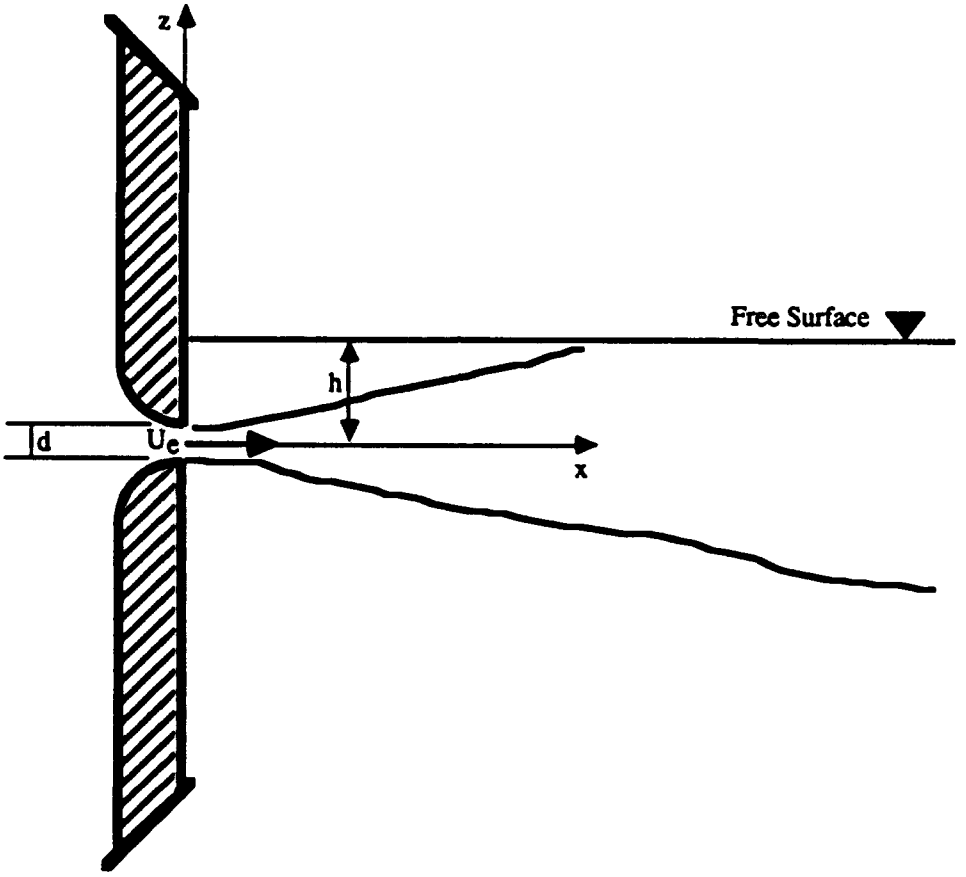


Figure 1.1 - Schematic diagram of the flow geometry.

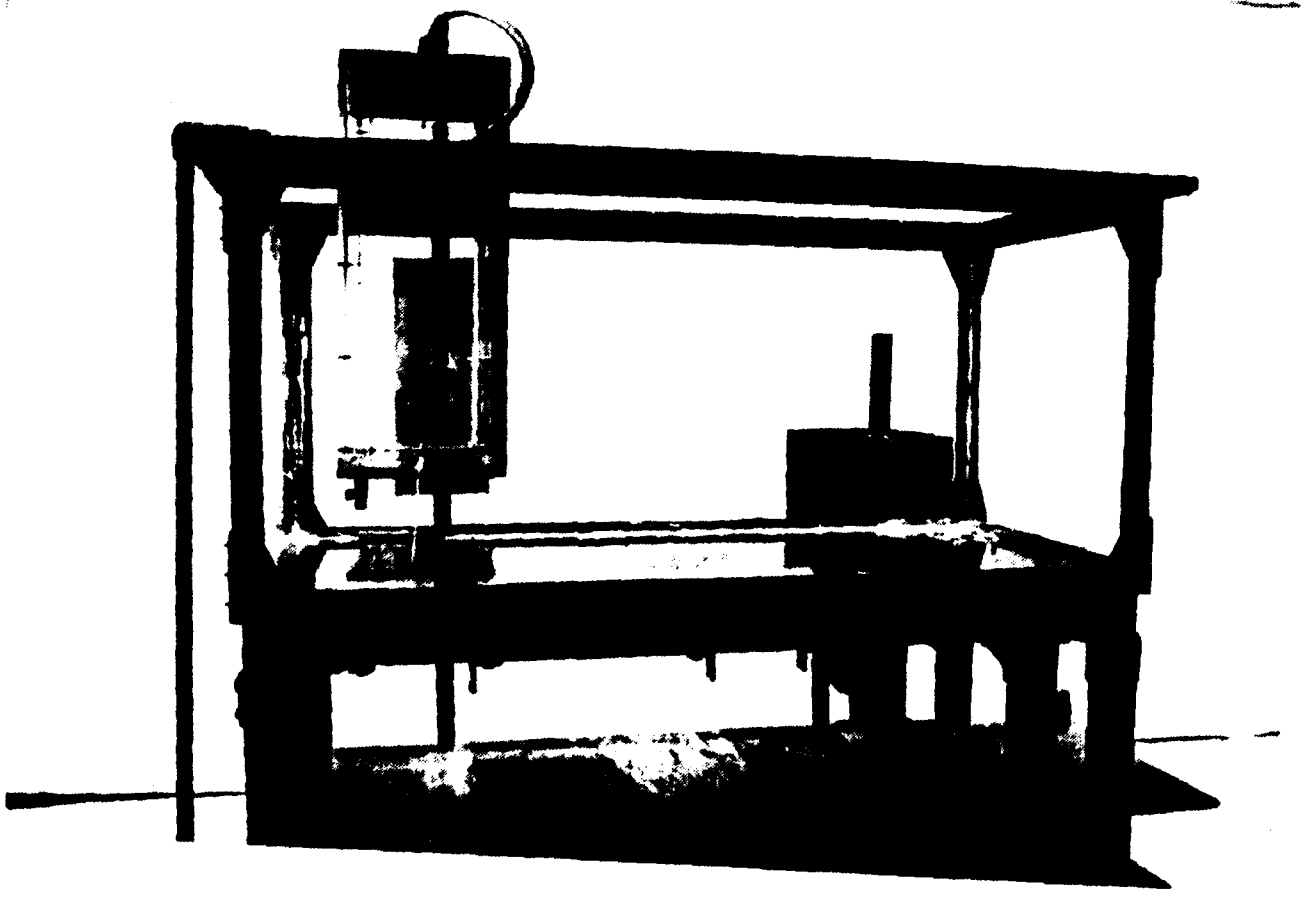
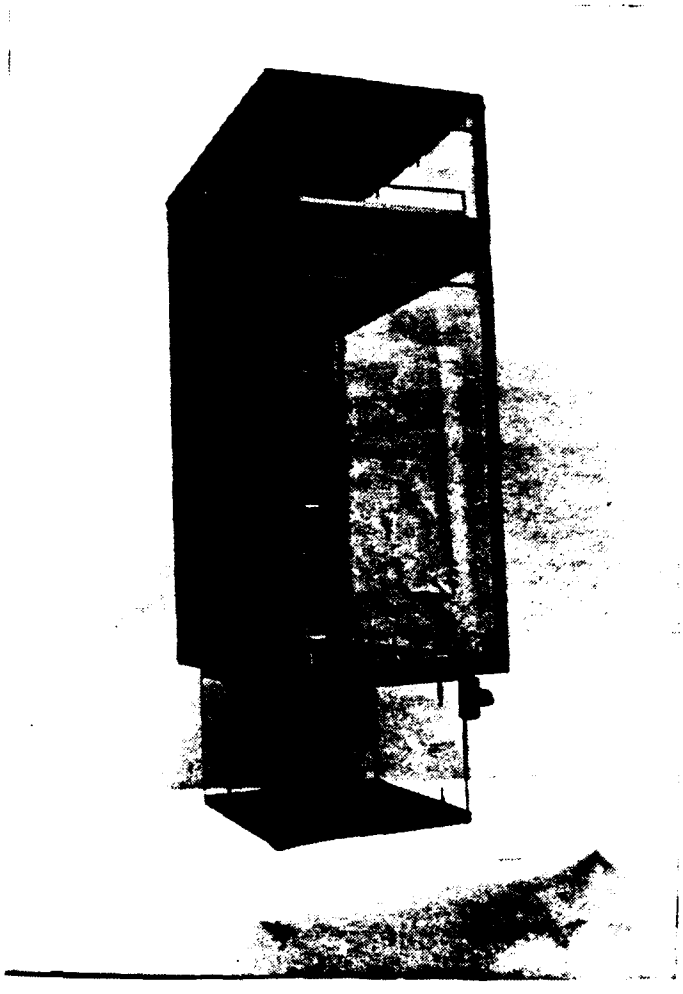
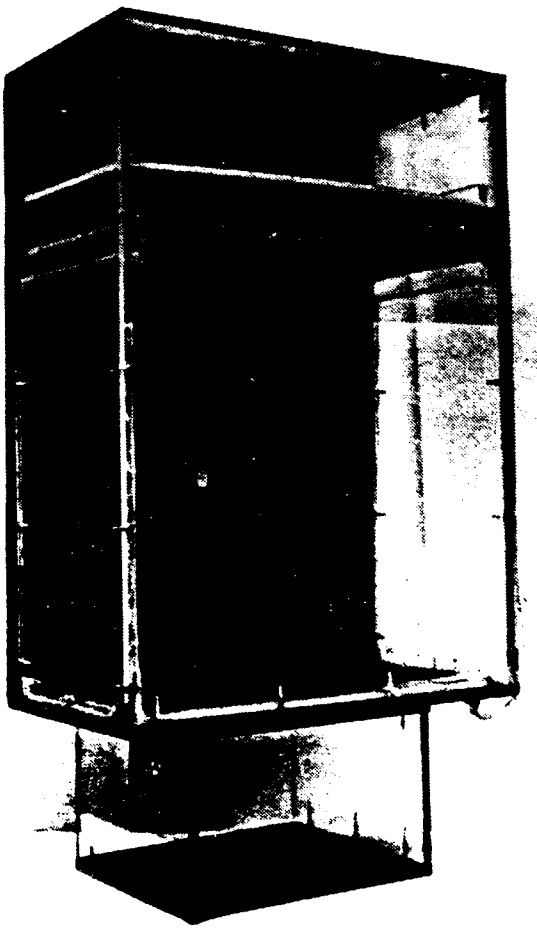


Figure 2.1 - Photograph of the experimental facility.



(a)

Figure 2.2a - Photograph of the jet tank.
(a) View from the front. (b) View from the back.



(b)

Figure 2.2b - Photograph of the jet tank.
(a) View from the front. (b) View from the back.

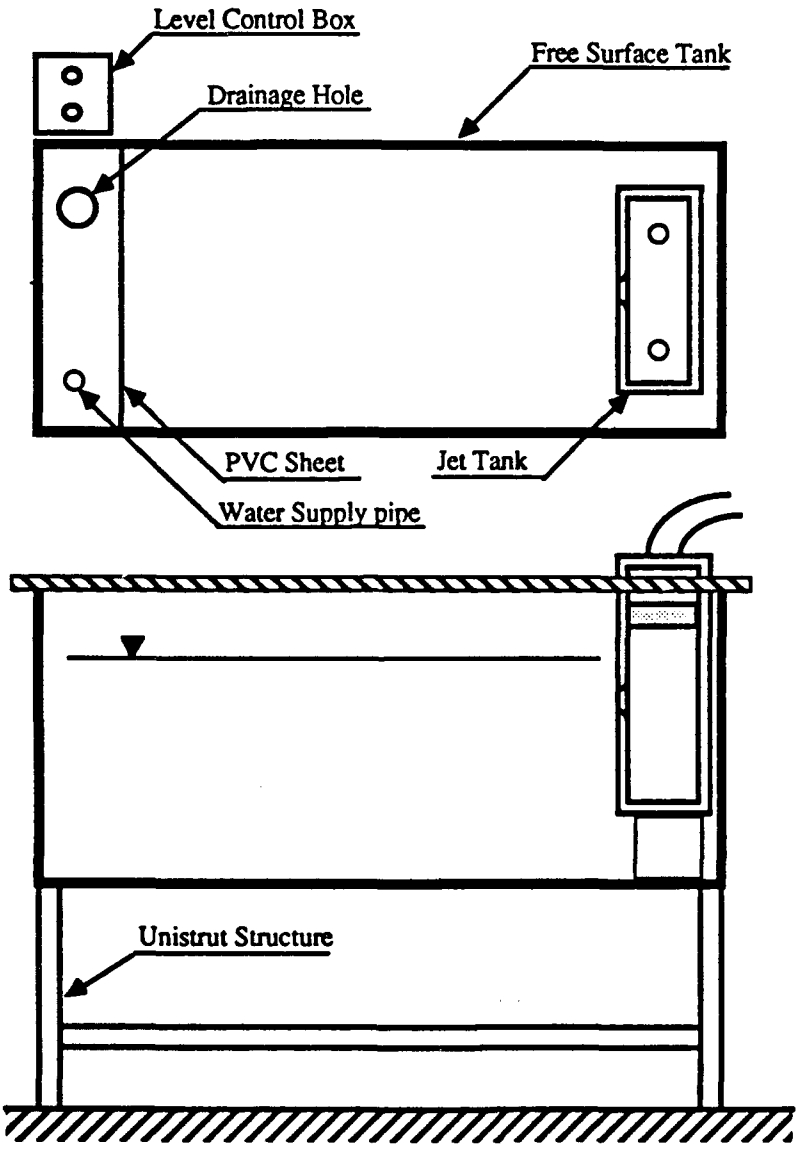


Fig. 2.3 - Schematic diagram of the free surface tank with jet tank inside.

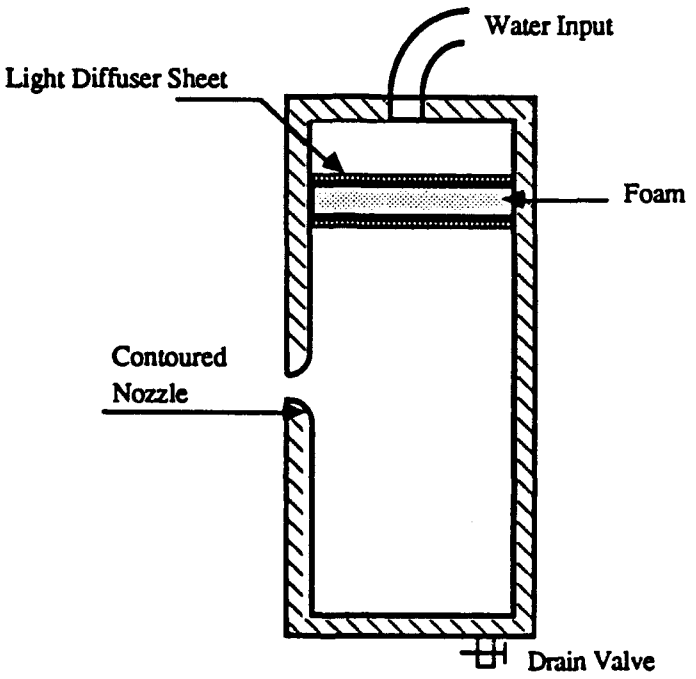


Fig. 2.4 - Schematic diagram of the jet tank.

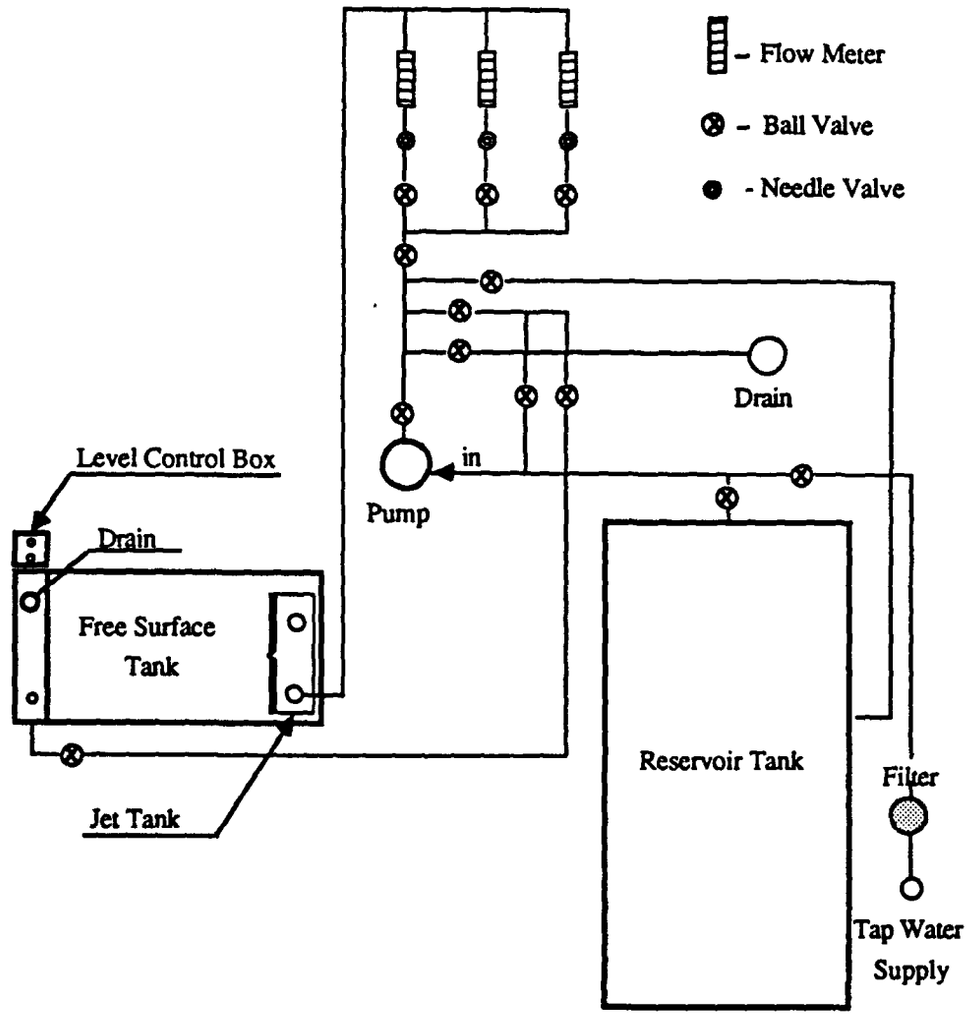


Fig. 2.5 - Schematic diagram of piping system.

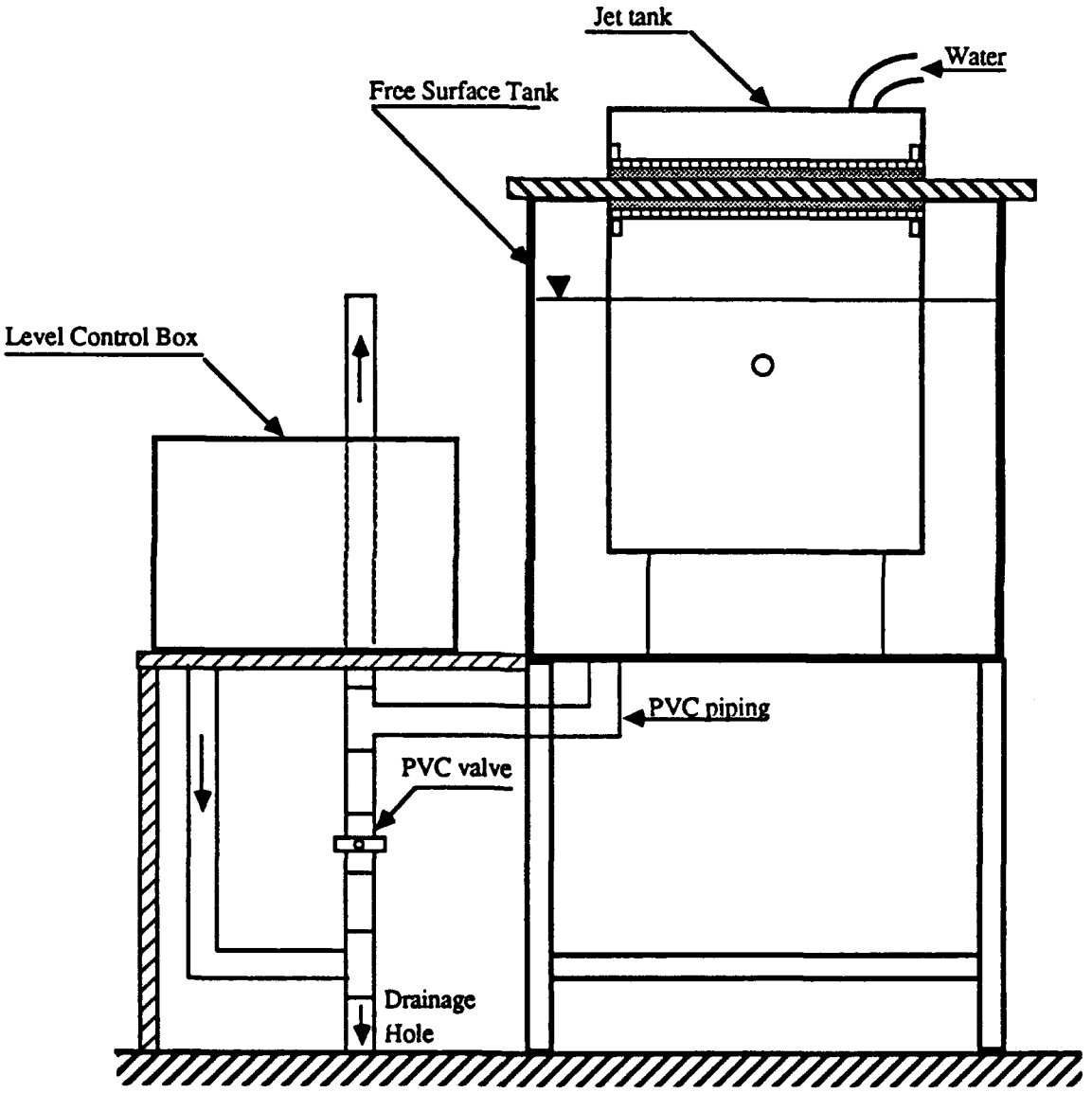


Fig. 2.6 - Schematic diagram of the level control apparatus.

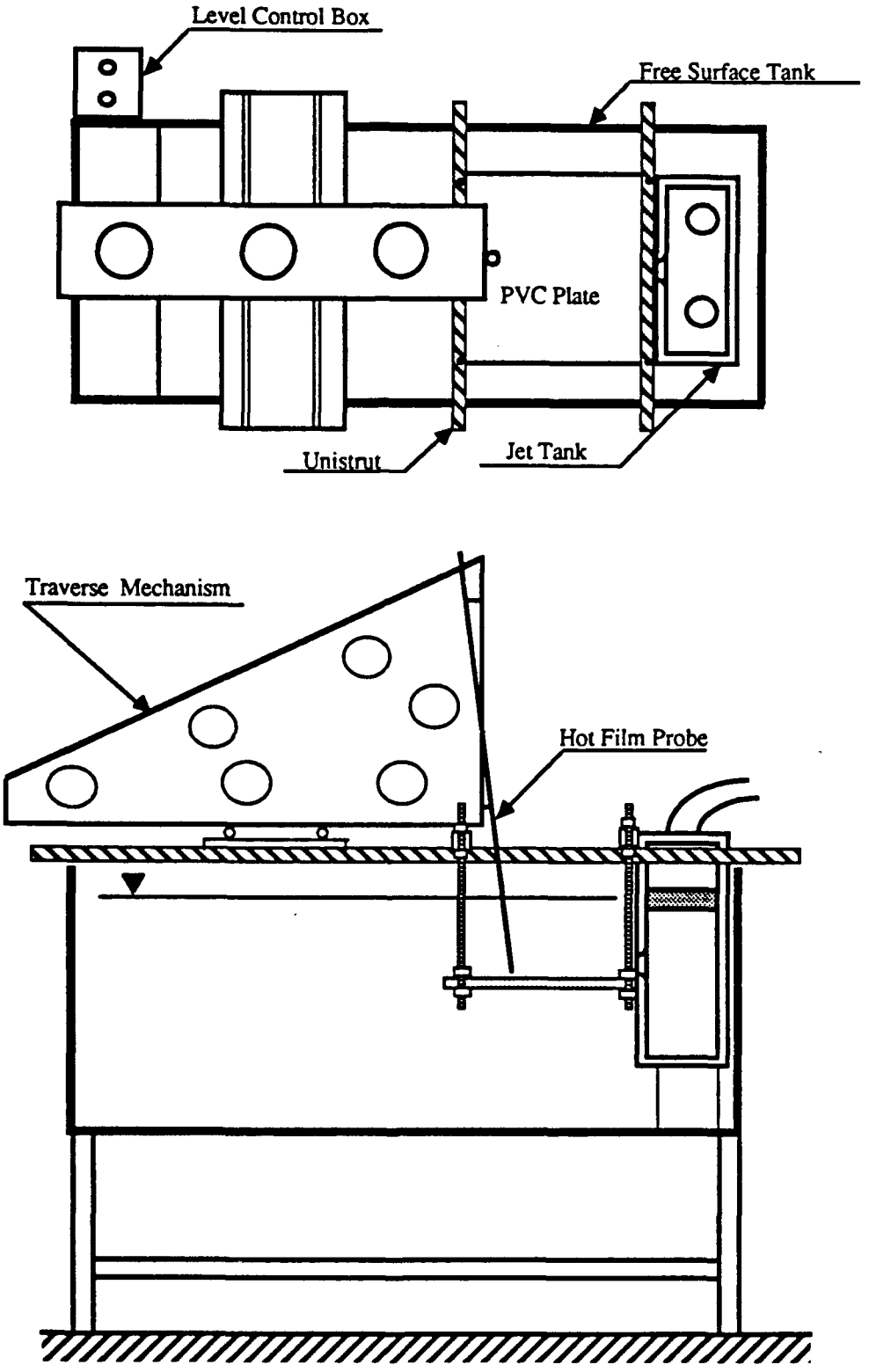


Fig. 2.7 - Schematic diagram of the apparatus used for the wall jet velocity measurements.

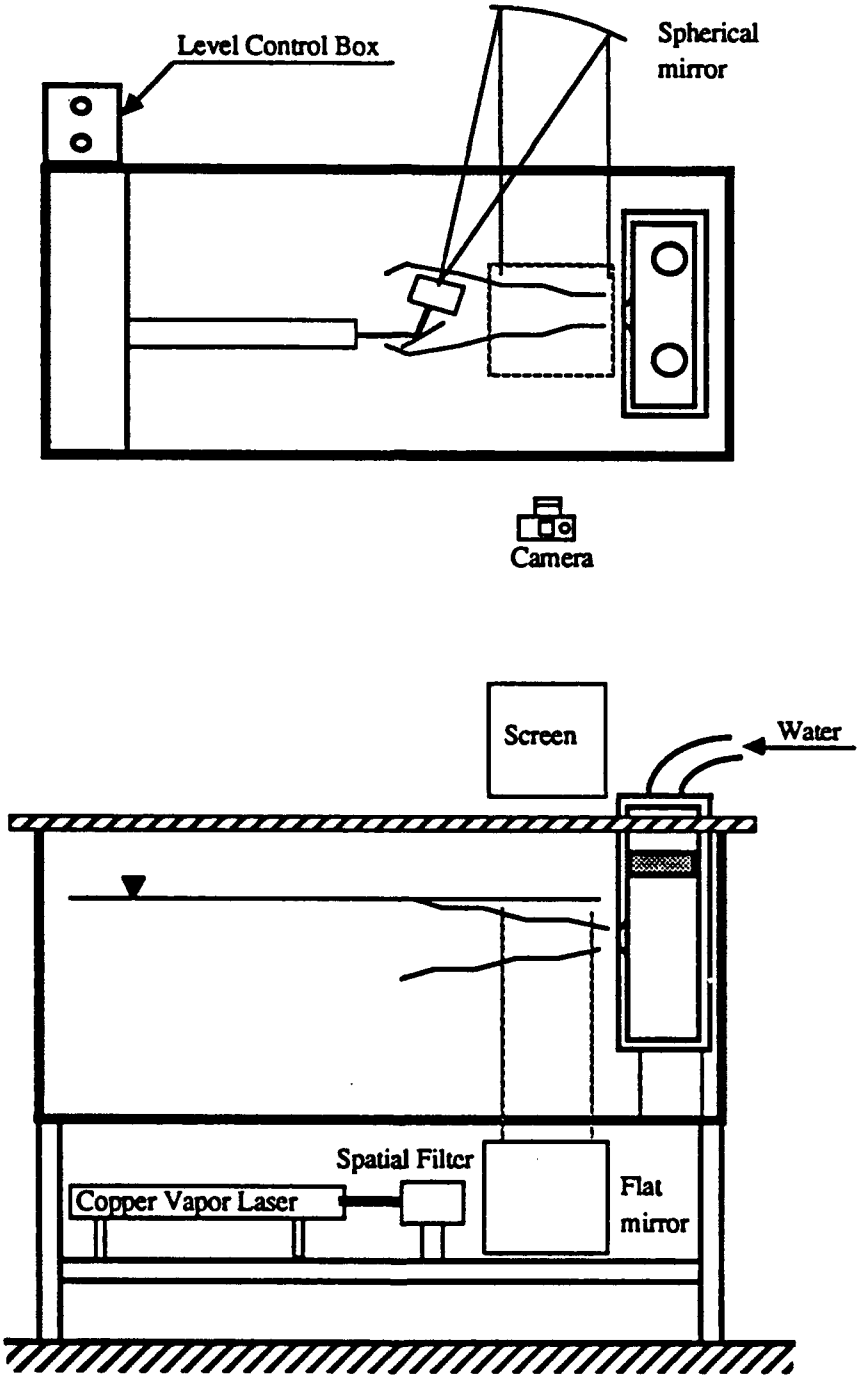


Fig. 2.8 - Schematic diagram of the apparatus used for shadowgraph flow visualization.

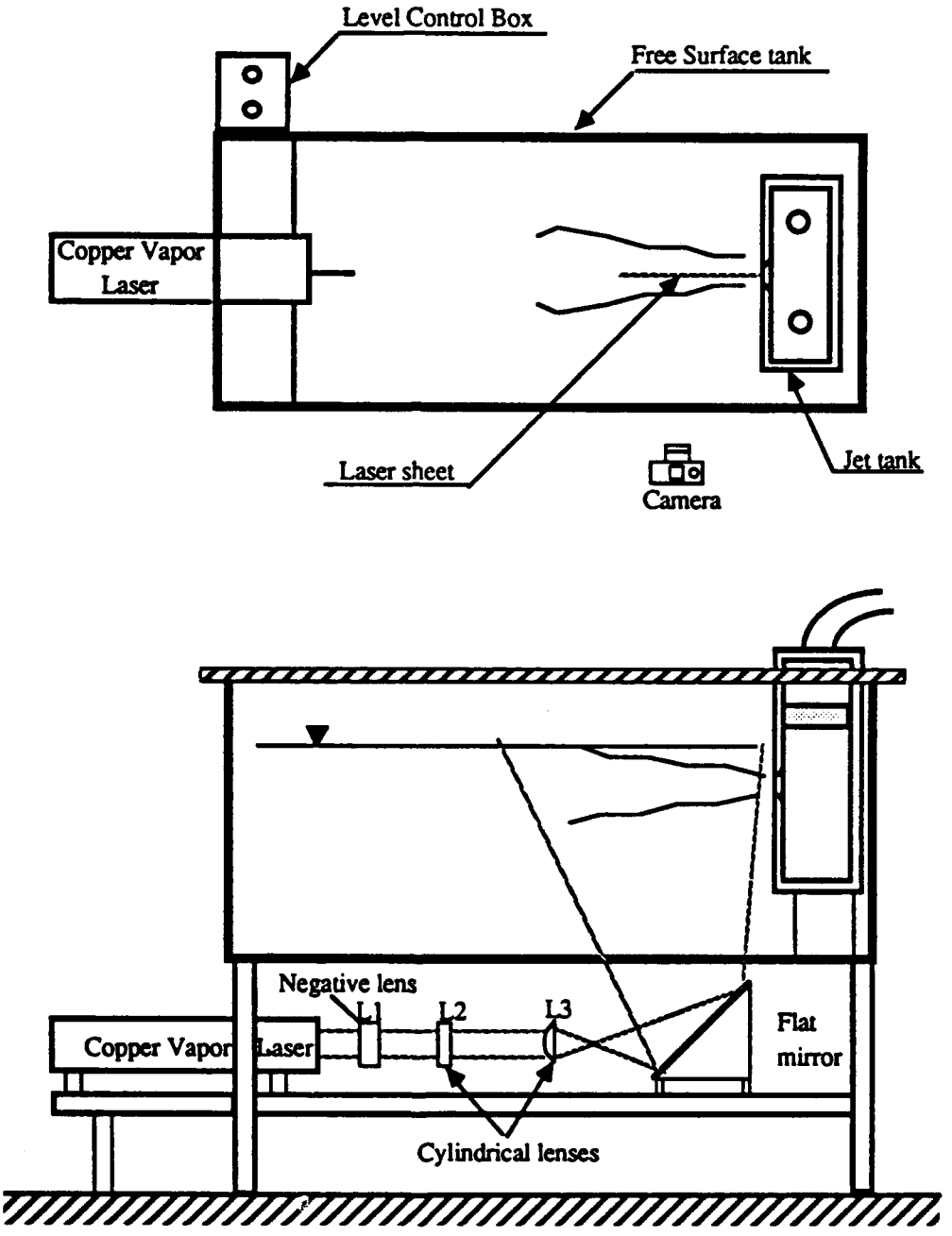


Fig. 2.9 - Schematic diagram of the apparatus used for LIF flow visualization technique.

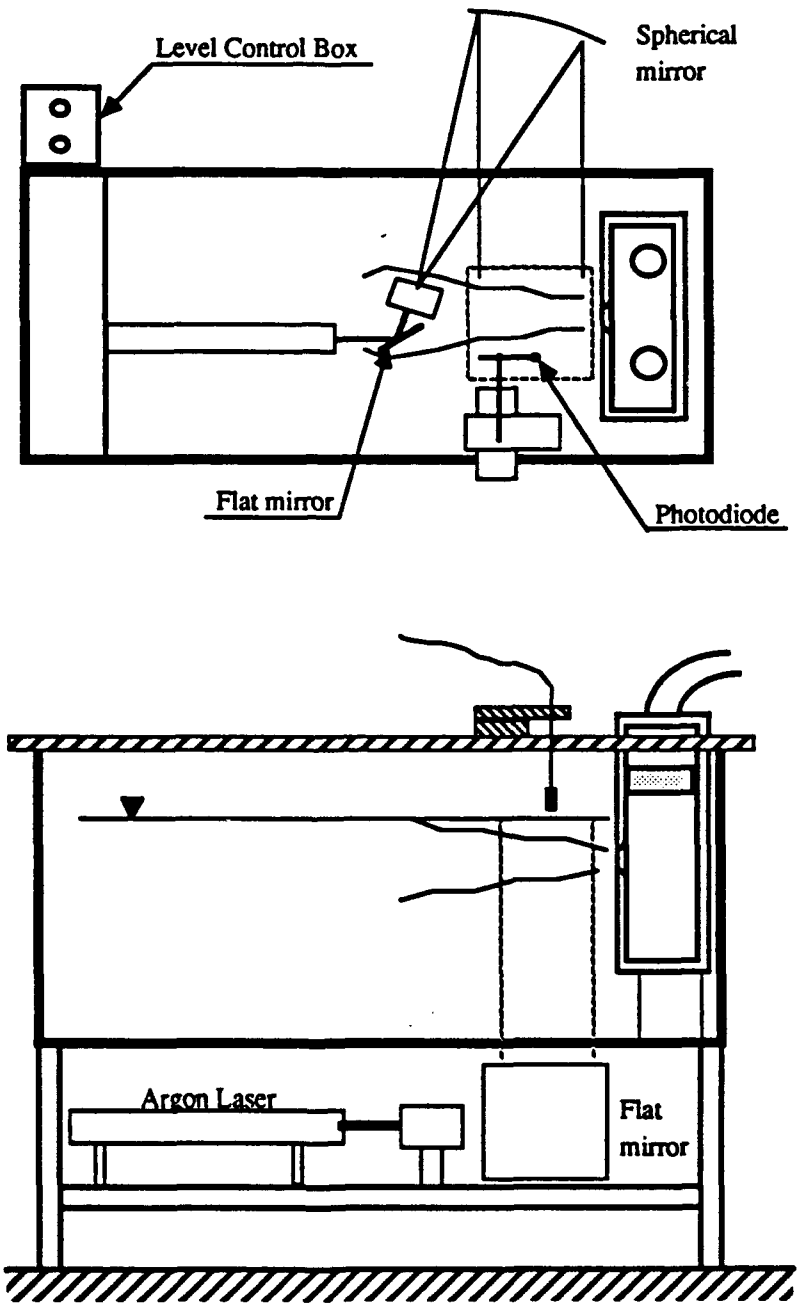


Fig. 2.10 - Schematic diagram of the apparatus used for surface curvature measurements.

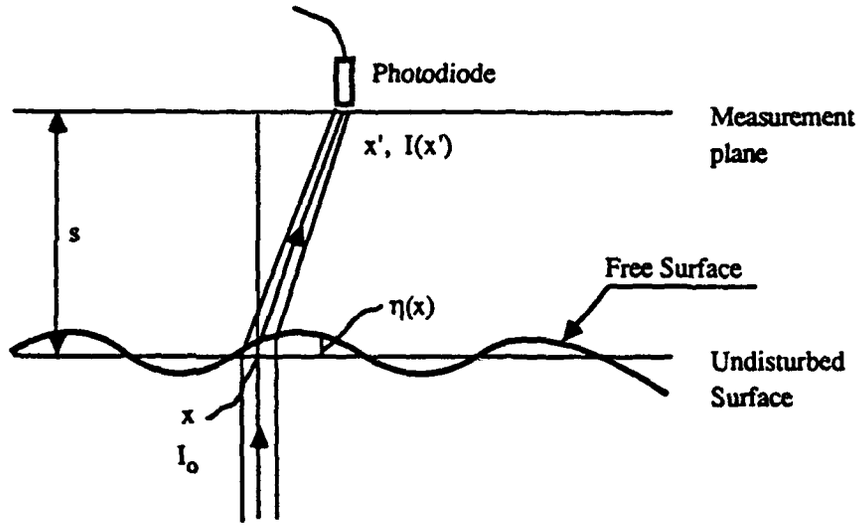


Fig. 2.11 - Schematic diagram of surface curvature measurement technique.

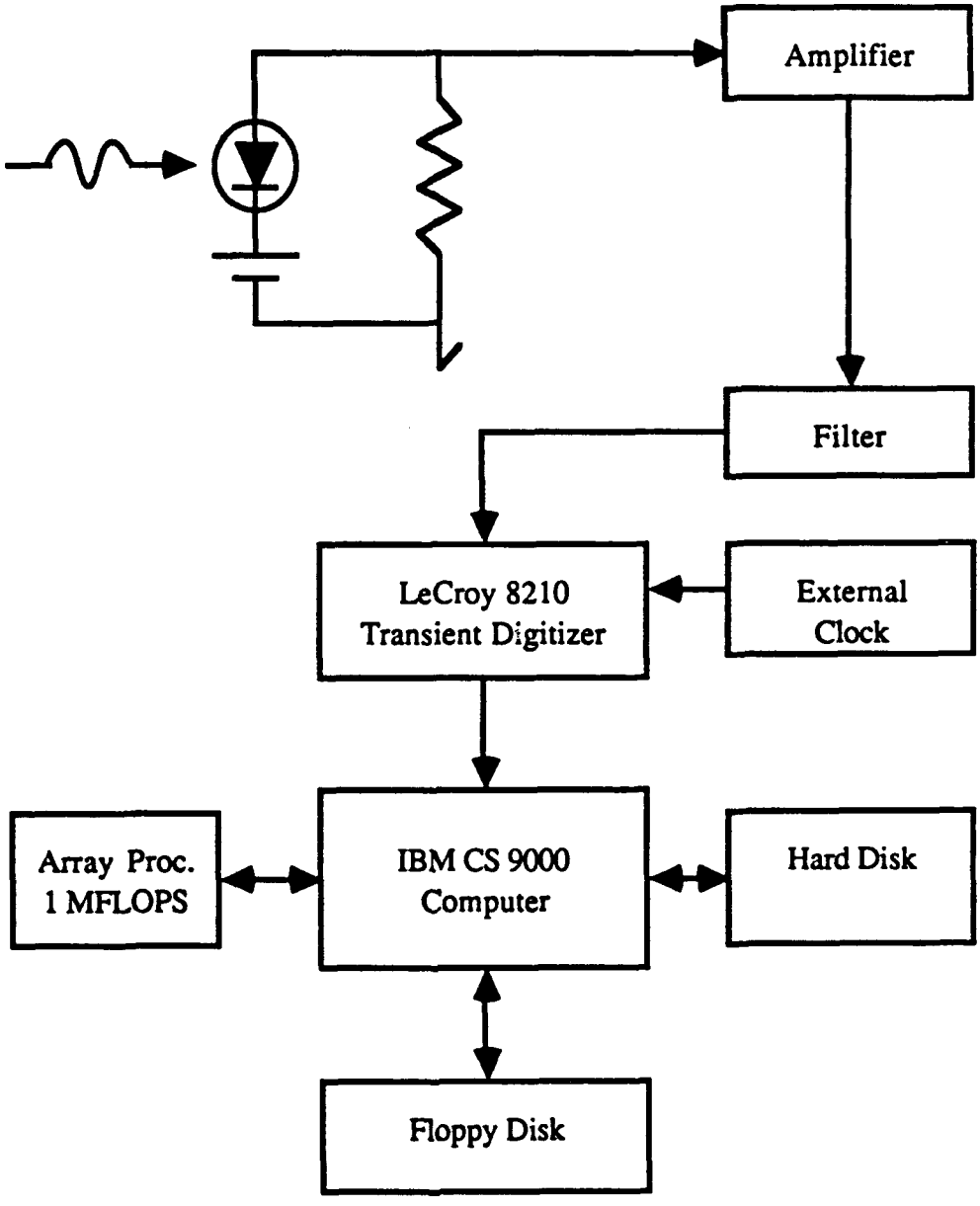


Fig. 2.12 -Block diagram of the data acquisition and storage apparatus for surface curvature measurements.

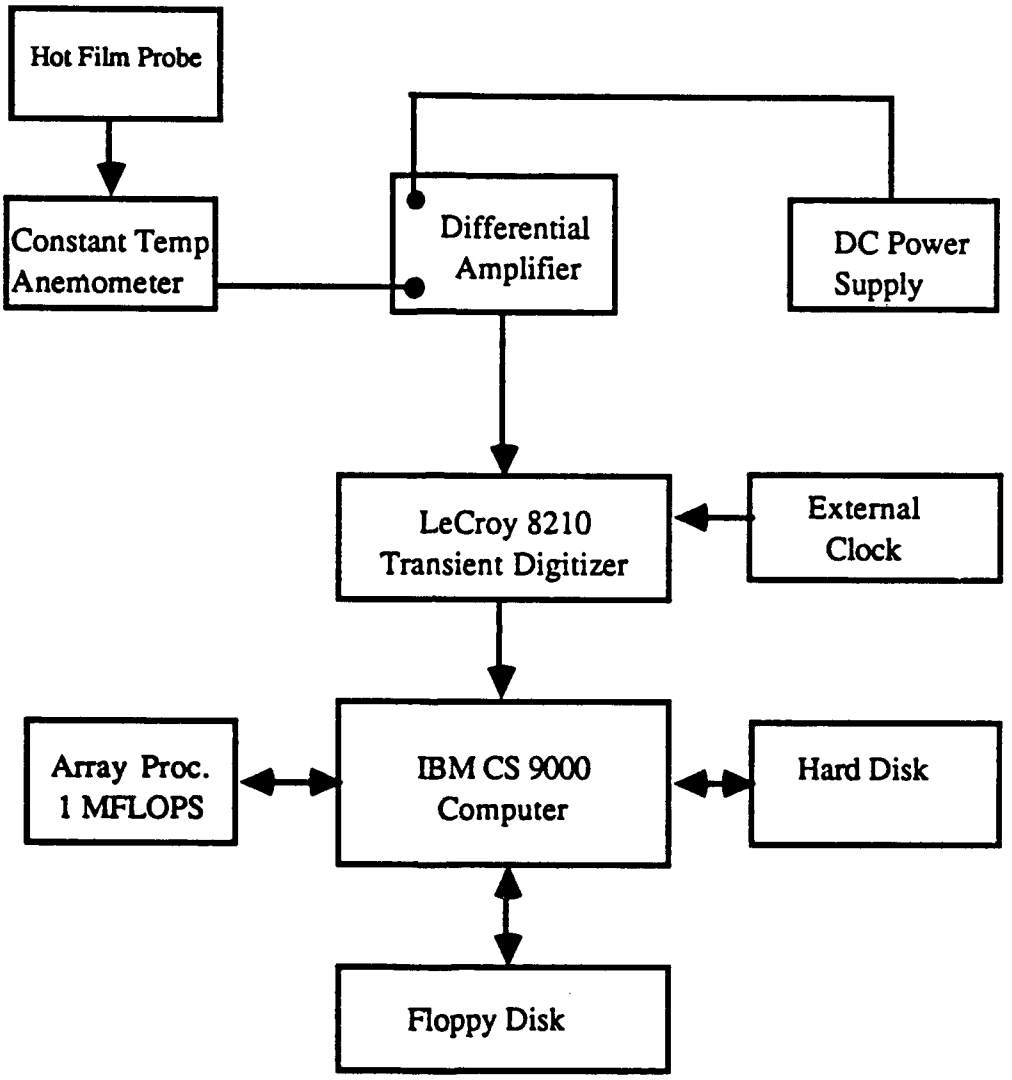


Fig. 2.13 - Block diagram of the data acquisition and storage apparatus for hot film velocity measurements.

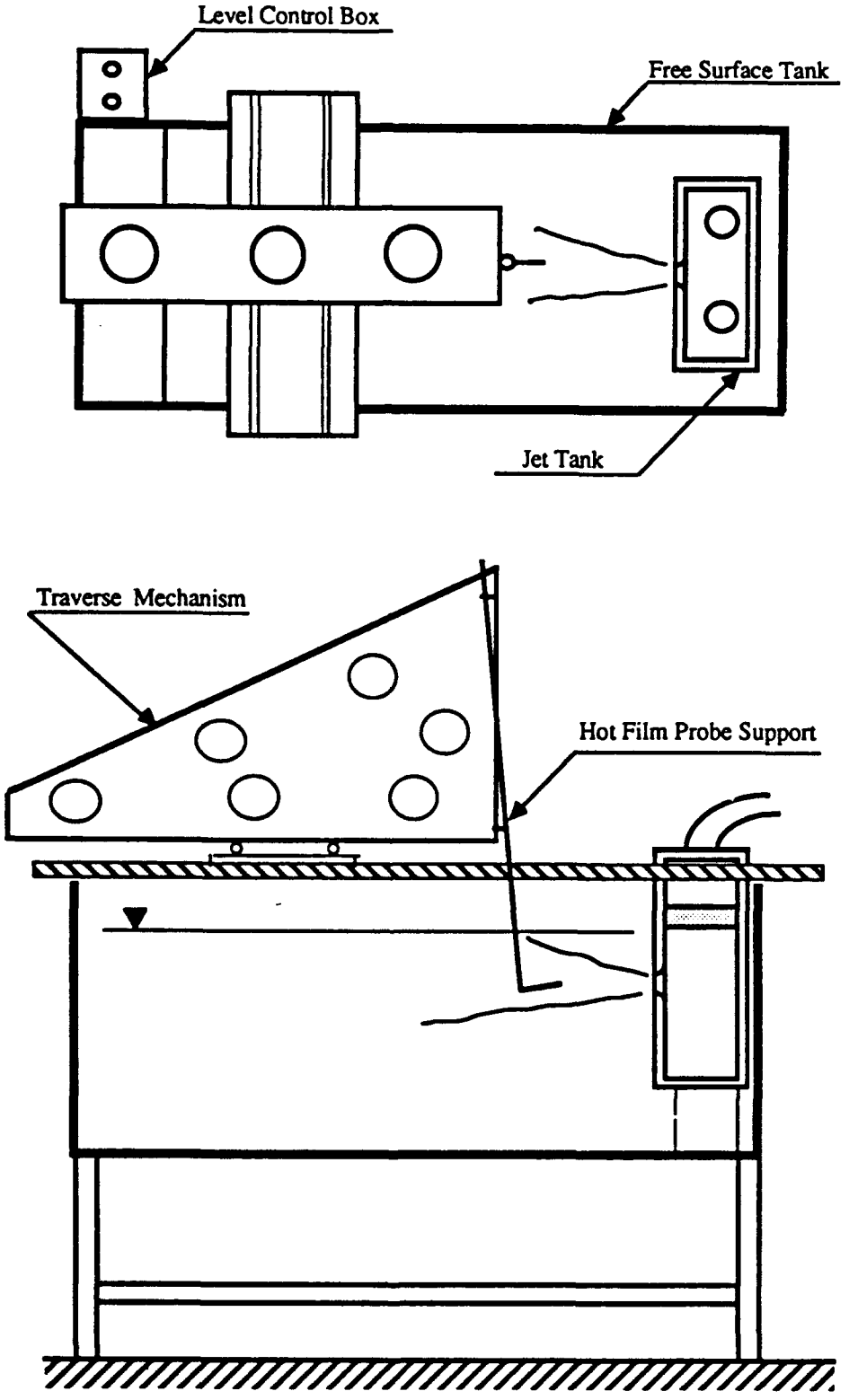


Fig. 2.14 - Schematic diagram of the apparatus used for hot film velocity measurements.

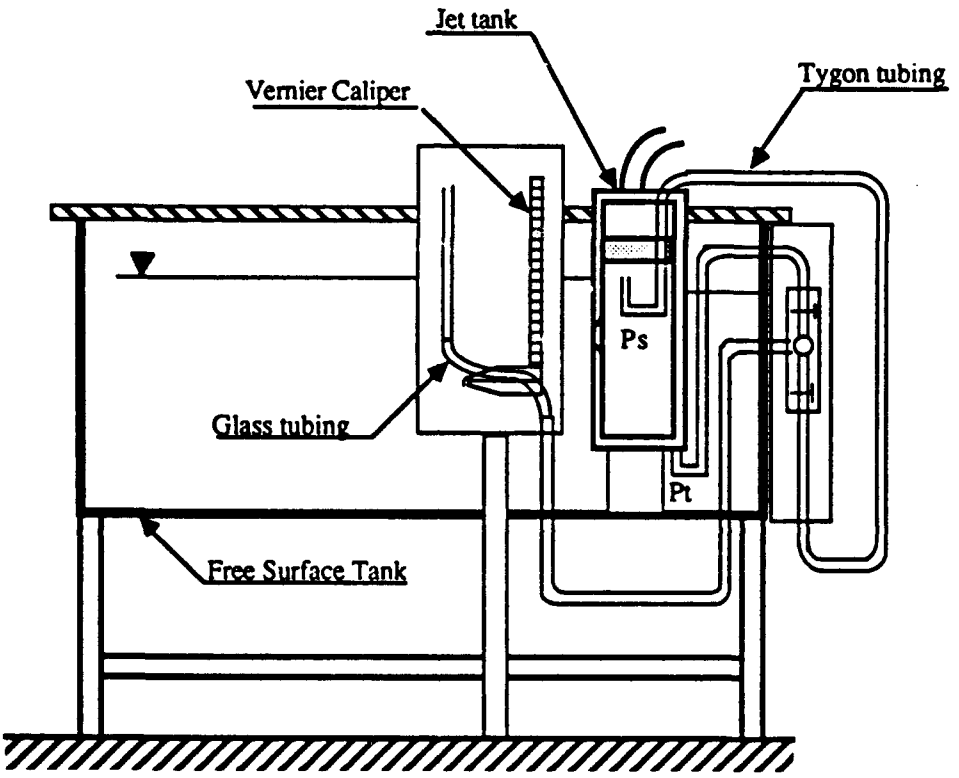


Fig. 2.15 - Schematic diagram of the pressure manometer used for measurements of jet exit velocity.

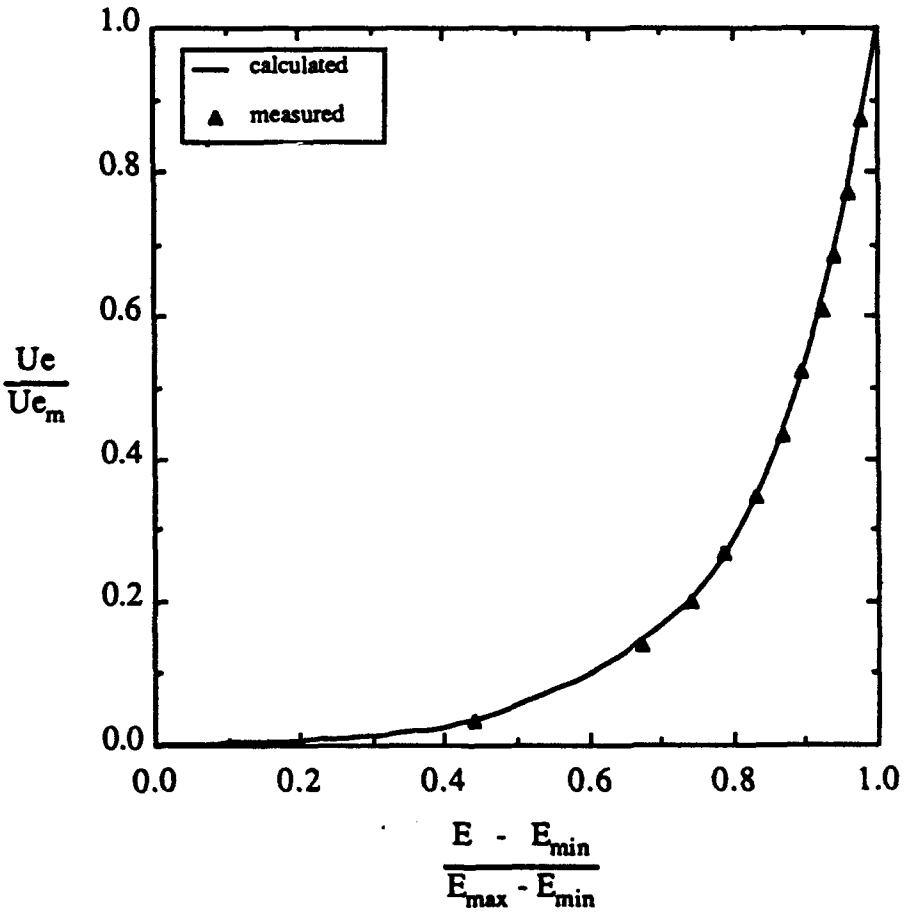


Figure 2.16 - Plot of measured and calculated calibration velocity data.



Figure 3.1- LIF photograph of submerged jet flow. U_e = 10 cm/s,
Reynolds number 2.5×10^3, h/d=1. Region covered 0<x/d<10.



Figure 3.2- LIF photograph of submerged jet flow. U_e = 35 cm/s,
Reynolds number 8.9×10^3, h/d=1. Region covered 0<x/d<10.



Figure 3.3- Shadowgraph picture of underwater jet flow. U_e = 25 cm/s, Reynolds number 6.3×10^3, h/d=1. Region covered $1<x/d<10$.



Figure 3.4 - Shadowgraph picture of underwater jet flow. U_e = 35 cm/s, Reynolds number 8.9×10^3, h/d=1. Region covered $1<x/d<10$.



Figure 3.5 - Shadowgraph picture of underwater jet flow. U_e = 50 cm/s, Reynolds number 1.3×10^4, h/d=1. Region covered $1<x/d<10$.

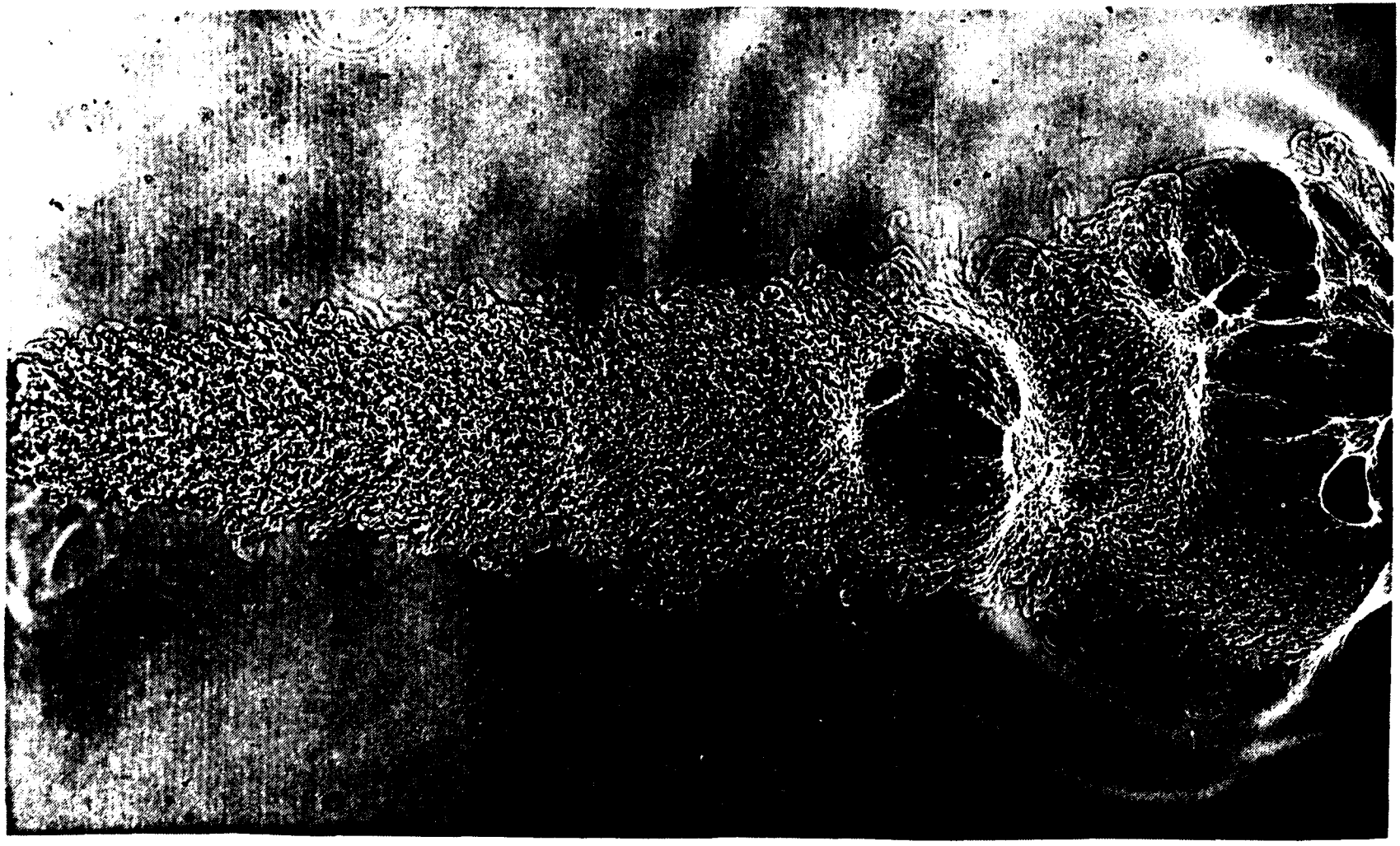


Figure 3.6 - Shadowgraph picture of underwater jet flow. U_e = 100 cm/s,
Reynolds number 1.27×10^4, h/d=3.5. Region covered 4<x/d<24.

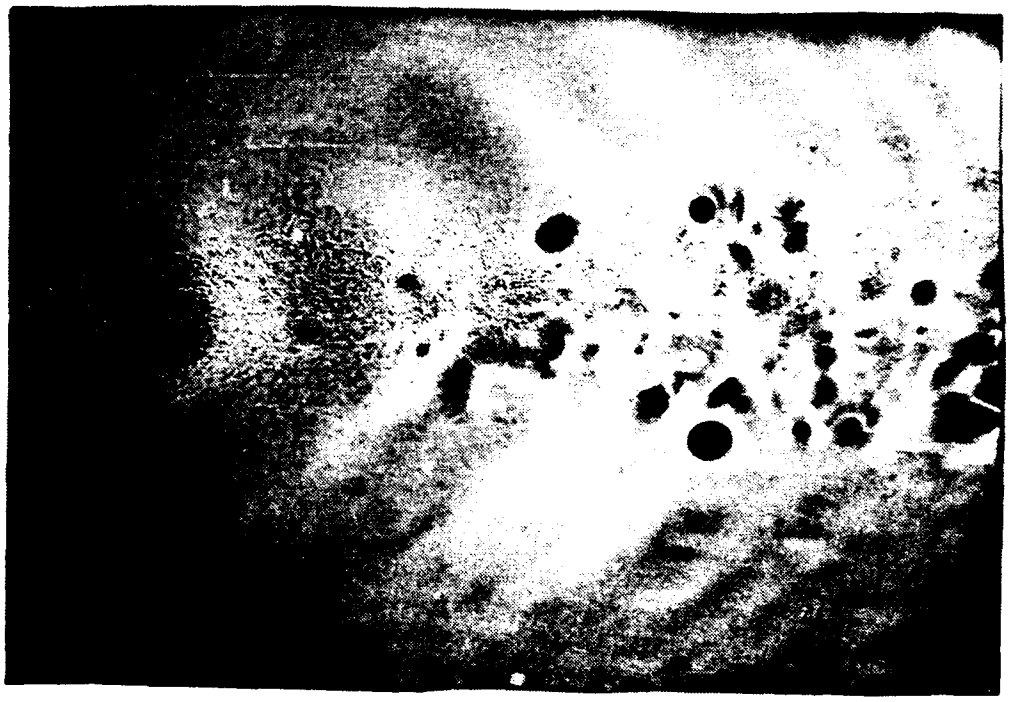


Figure 3.7 - Shadowgraph picture of underwater jet flow. U_e = 150 cm/s, Reynolds number 9.5×10^3, h/d=5.5. Region covered 14<x/d<52.



Figure 3.8 - Shadowgraph picture of underwater jet flow. U_e = 250 cm/s, Reynolds number 1.6×10^4, h/d=5.5. Region covered 14<x/d<52.

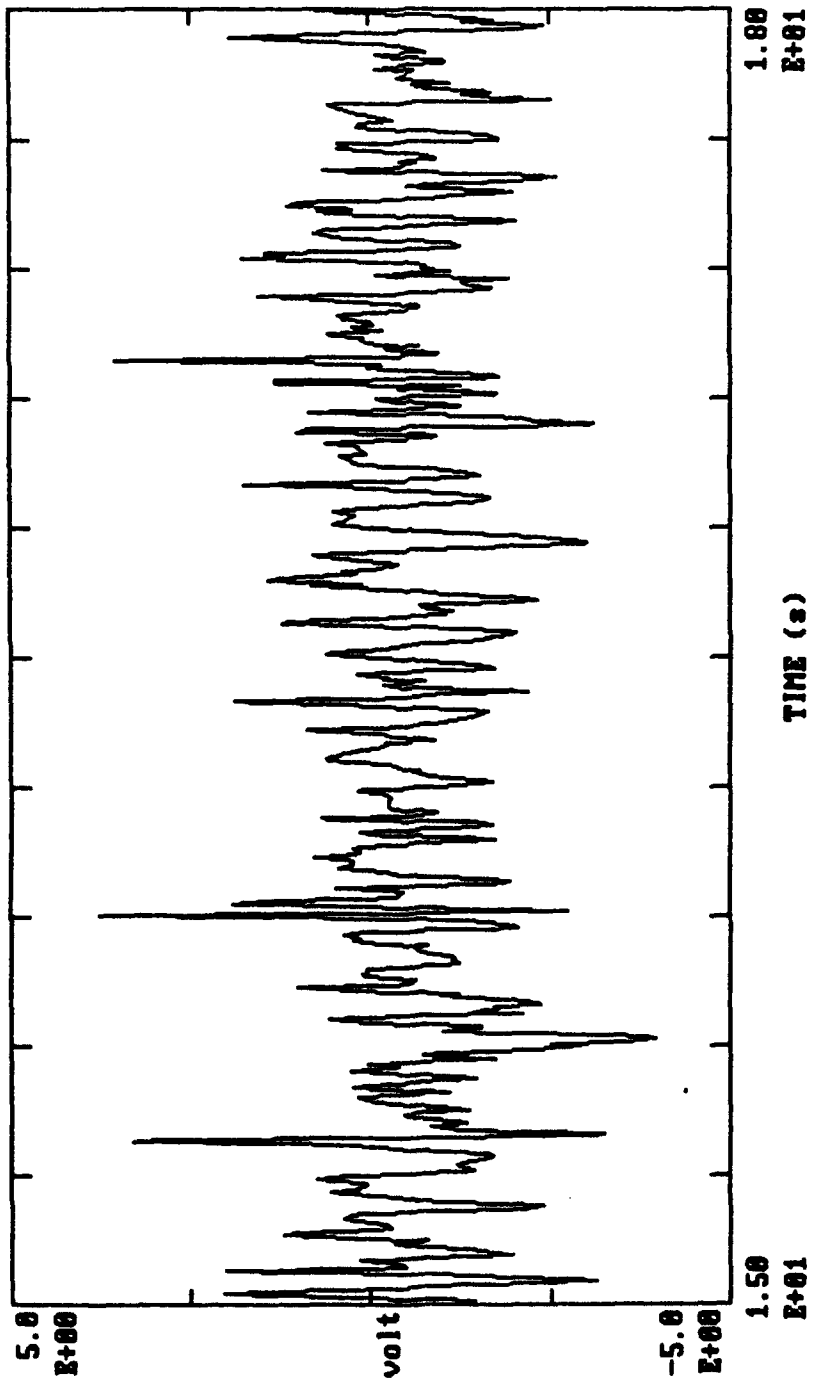


Figure 3.9 - Photodiode output signal at x/d=20, y/d=0.
U_e = 150 cm/s, Re = 9.5×10^3, h/d=2.5.

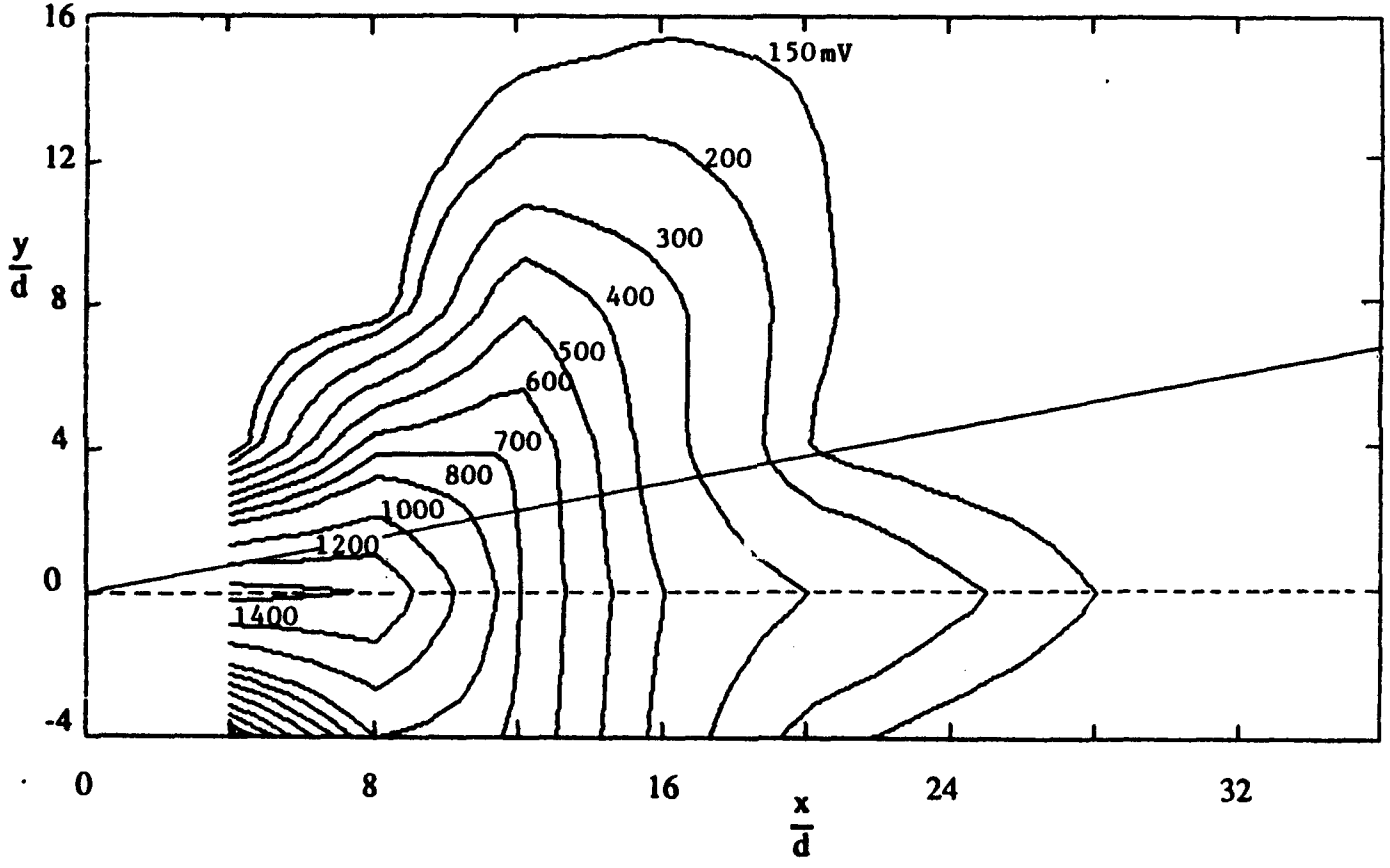


Figure 3.10 - Contour plot of rms value of photodiode output.
U_e = 50 cm/s, Re = 3.2×10^3, h/d=1.

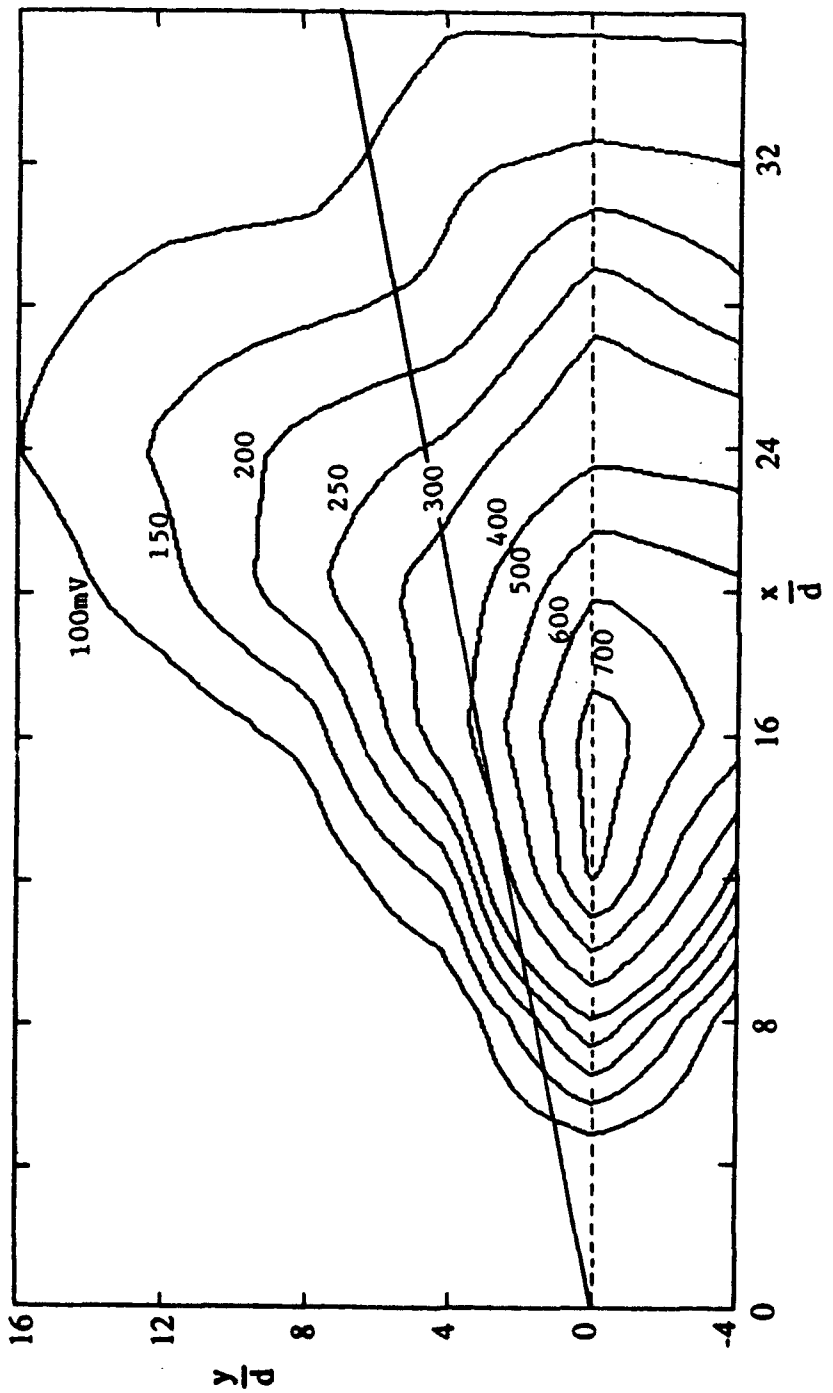


Figure 3.11 - Contour plot of rms value of photodiode output.
U_e = 100 cm/s, Re = 6.4×10^3, h/d=2.5.

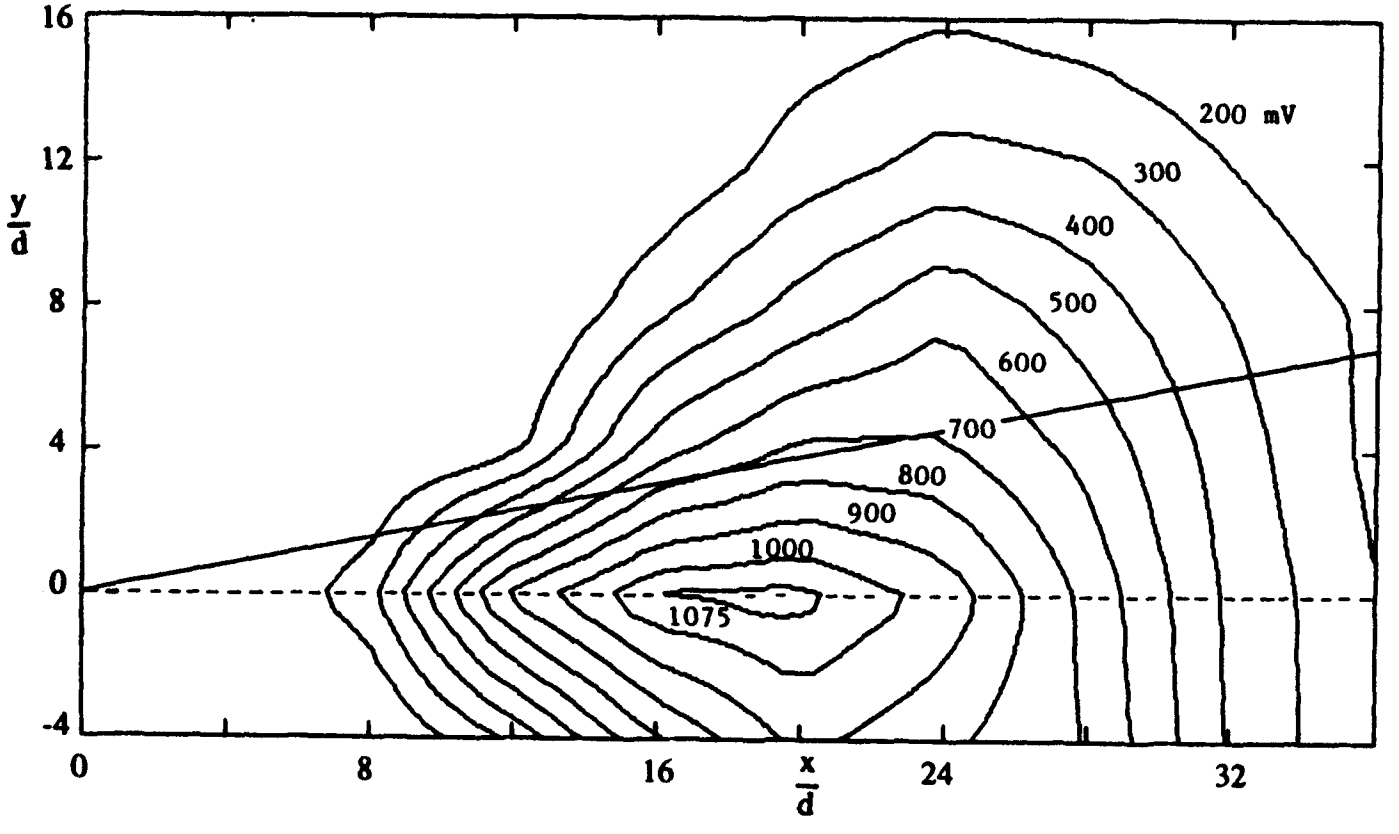


Figure 3.12 - Contour plot of rms value of photodiode output.
U_e = 150 cm/s, Re = 9.5×10^3, h/d=2.5.

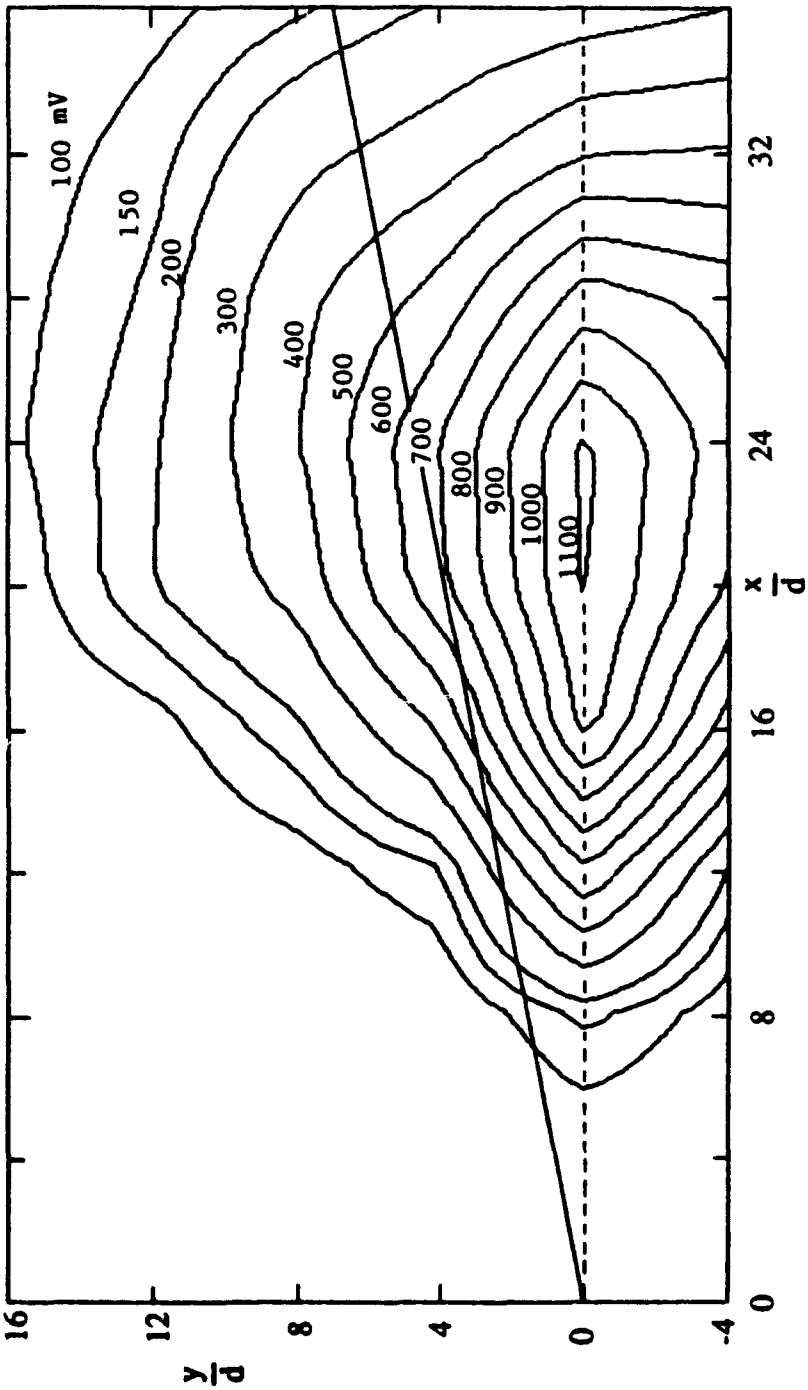


Figure 3.13 - Contour plot of rms value of photodiode output.
U_e = 200 cm/s, Re = 1.27×10^4, h/d=2.5.

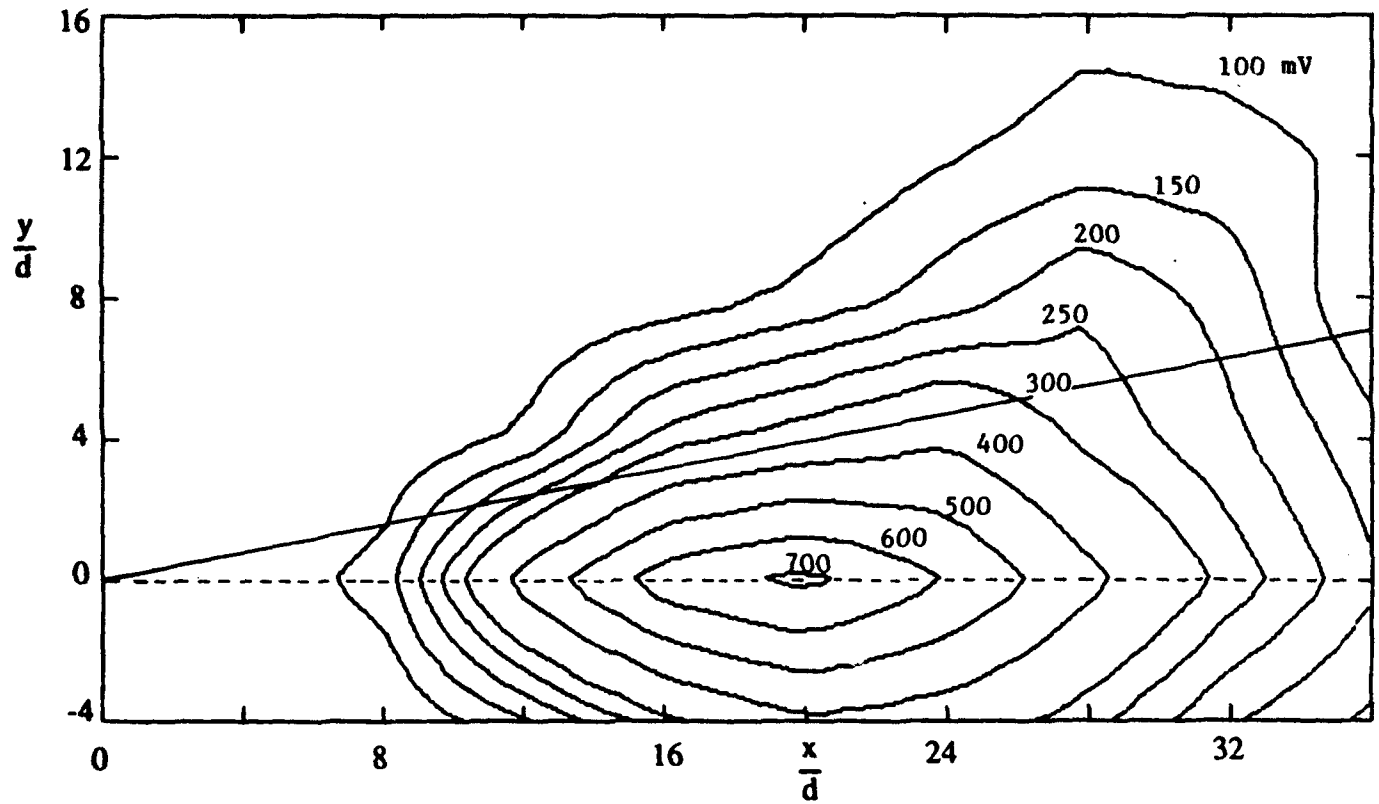


Figure 3.14 - Contour plot of rms value of photodiode output.
U_e = 100 cm/s, Re = 6.4×10^3, h/d=3.5.

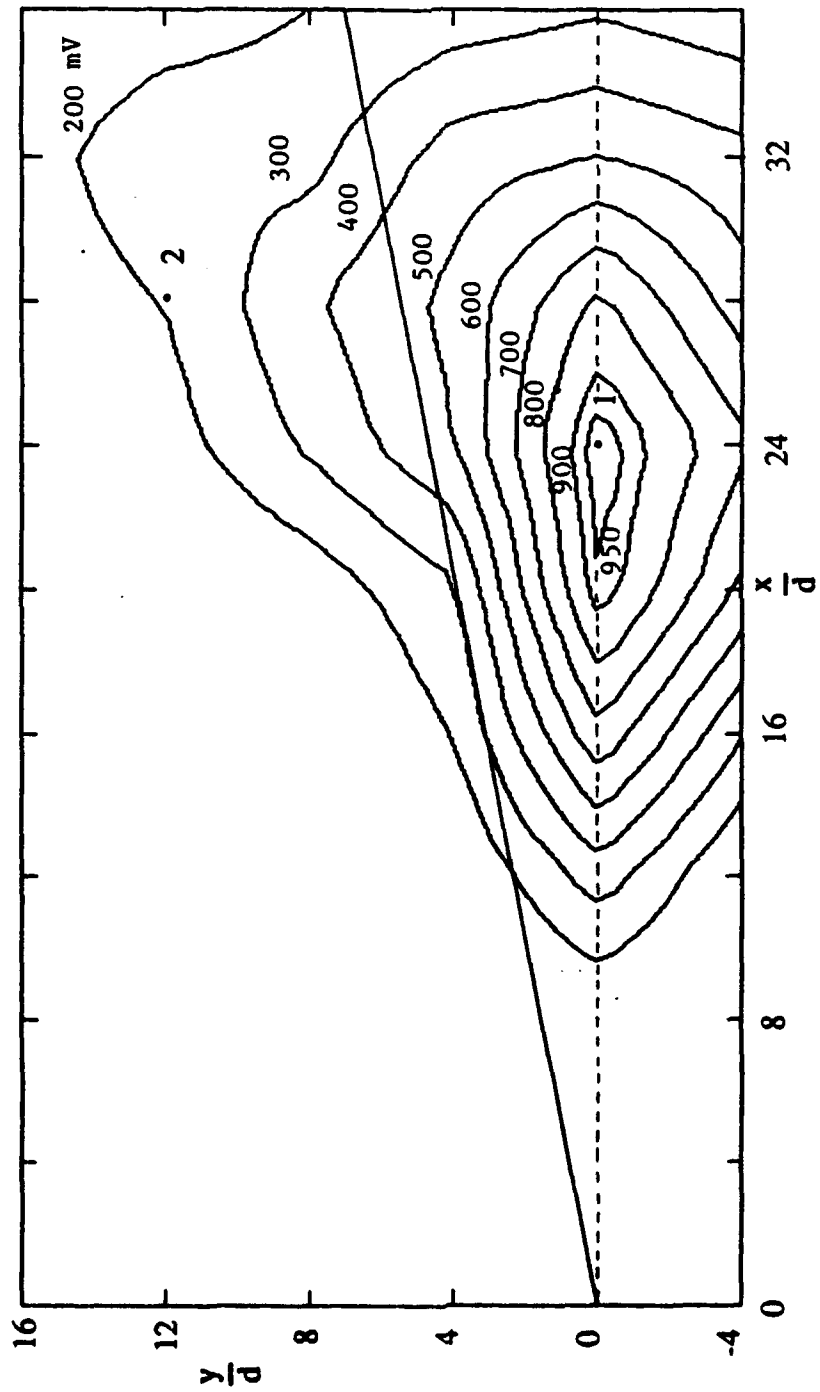


Figure 3.15 - Contour plot of rms value of photodiode output.
U_e = 150 cm/s, Re = 9.5x10^3, h/d=3.5.

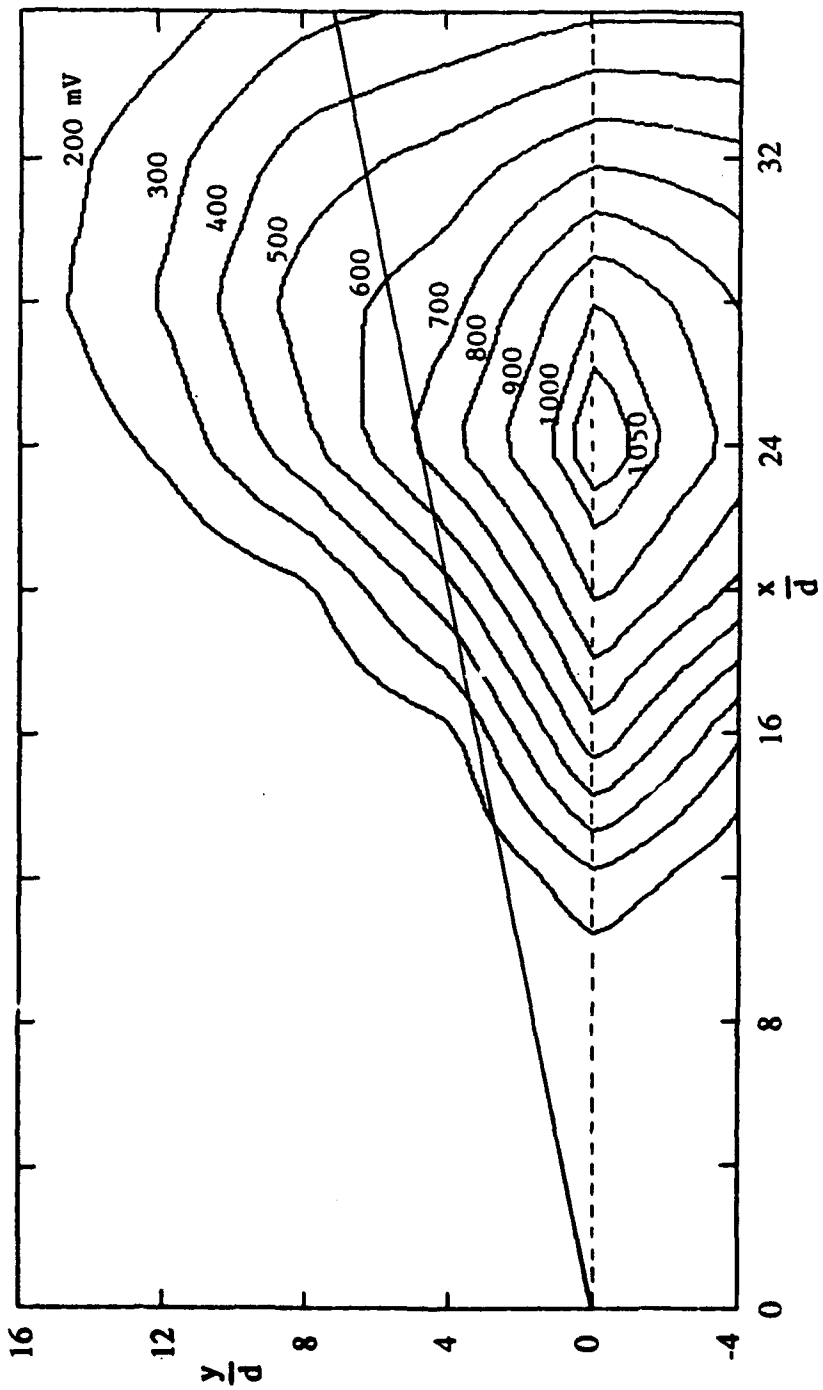


Figure 3.16 - Contour plot of rms value of photodiode output.
U_e = 200 cm/s, Re = 1.27×10^4, h/d=3.5.

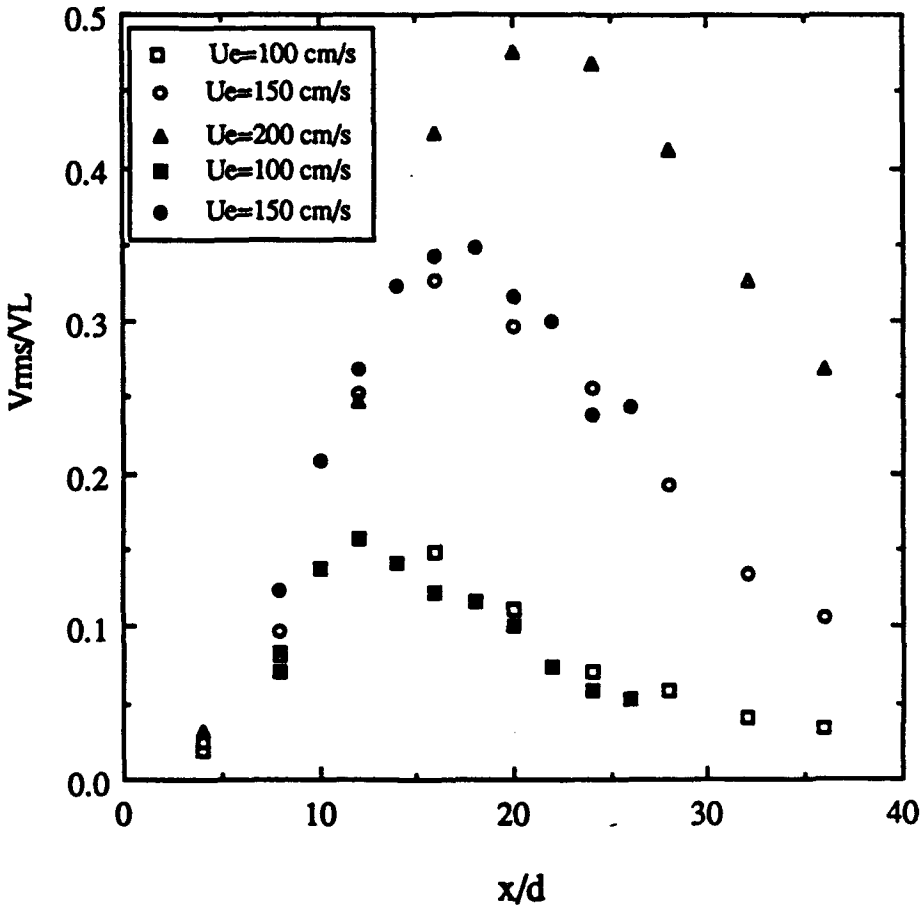


Figure 3.17 - Downstream evolution of the rms value of the surface curvature fluctuation along the jet centerline. Solid symbols d=1.27 cm. Open symbols d=0.64 cm. h/d=2.5 for all cases.

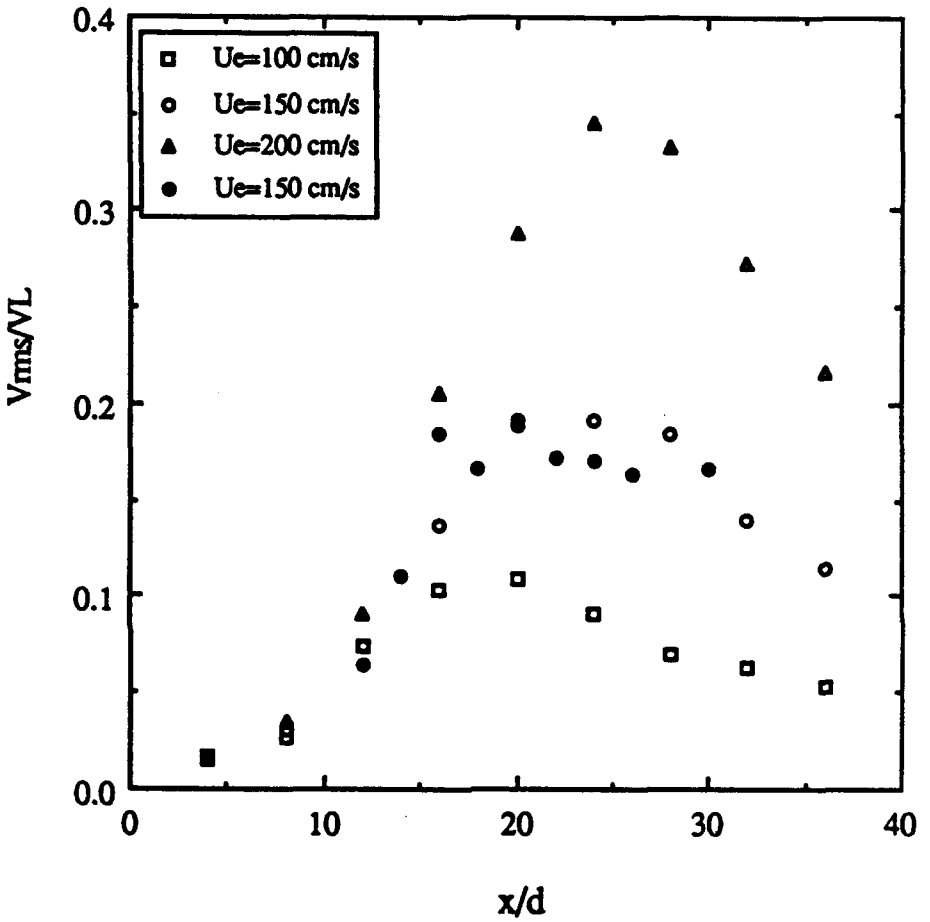


Figure 3.18 - Downstream evolution of the rms value of the surface curvature fluctuation along the jet centerline. Solid symbols d=1.27 cm. Open symbols d=0.64 cm. h/d=3.5 for all cases.

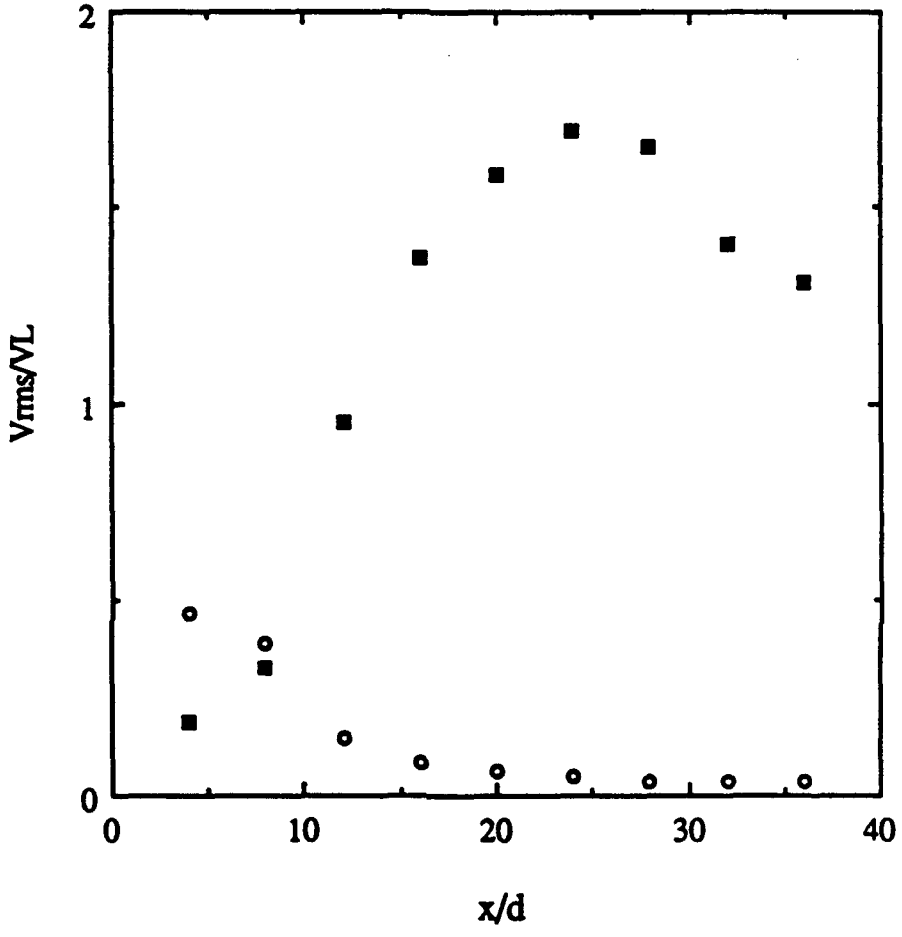


Figure 3.19 - Downstream evolution of the rms value of the surface curvature fluctuation along the jet centerline. Solid symbol U_e=200 cm/s, h/d=1.5. Open symbol U_e=50 cm/s, h/d=1.

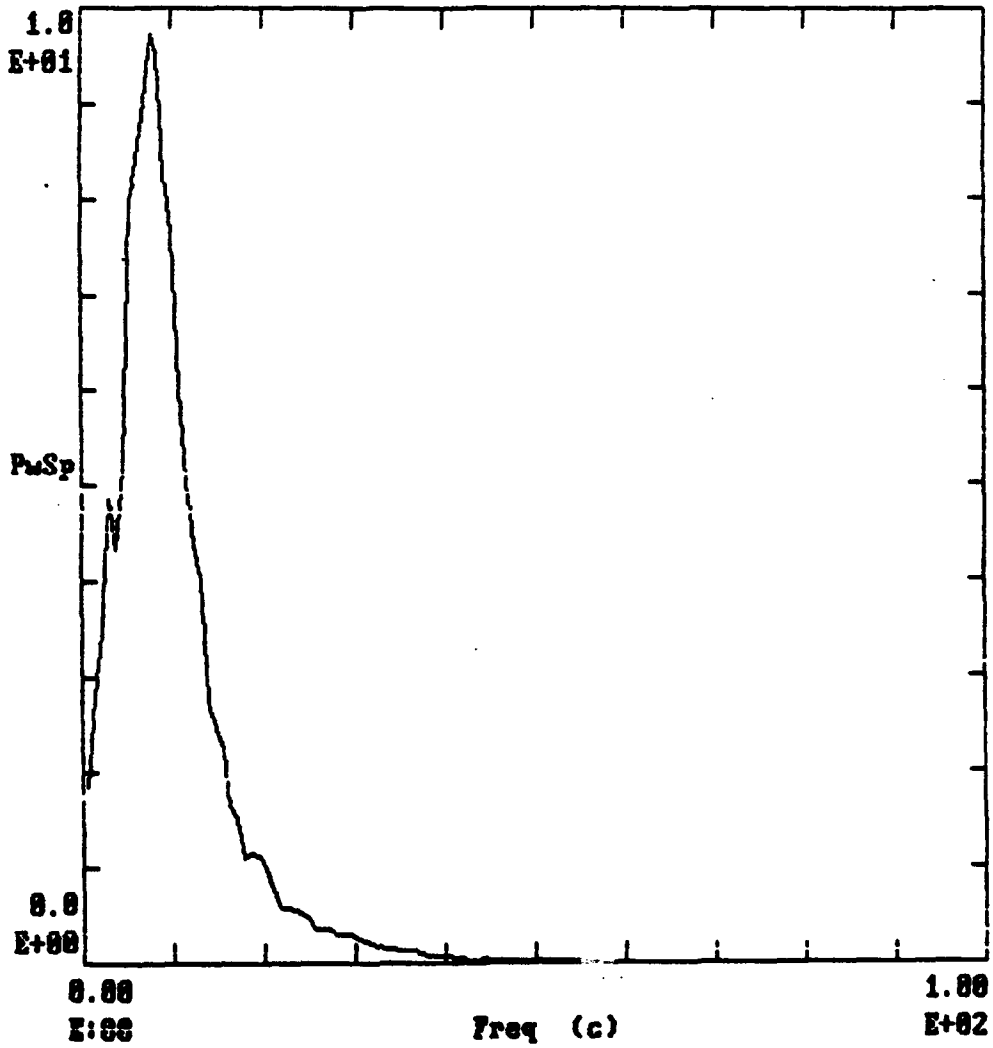


Figure 3.20 - Power spectrum of the surface curvature fluctuation at x/d=24, y/d=0. U_e=150 cm/s, Re = 9.5×10^3, h/d=3.5.

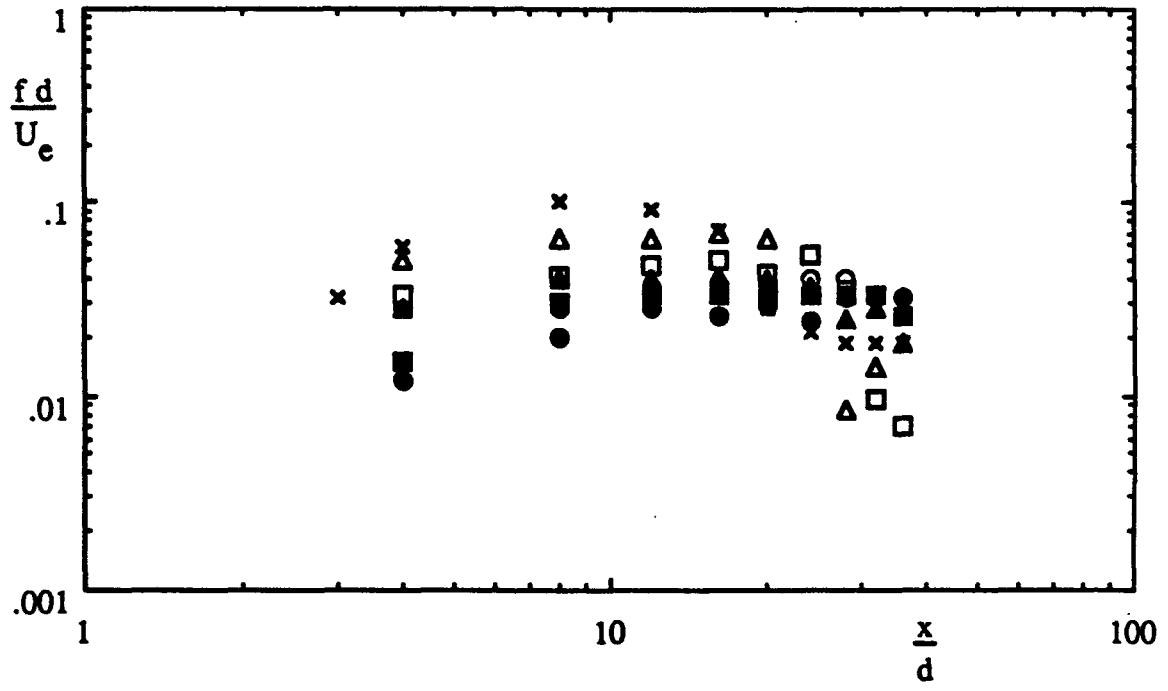


Figure 3.21 - Downstream evolution of normalized frequency corresponding to surface curvature fluctuation along the jet centerline. Solid symbols h/d=3.5. Open symbols h/d=2.5. Symbol, x - Ue = 200 cm/s, h/d=1.5. Jet exit diameter d=0.64 cm.

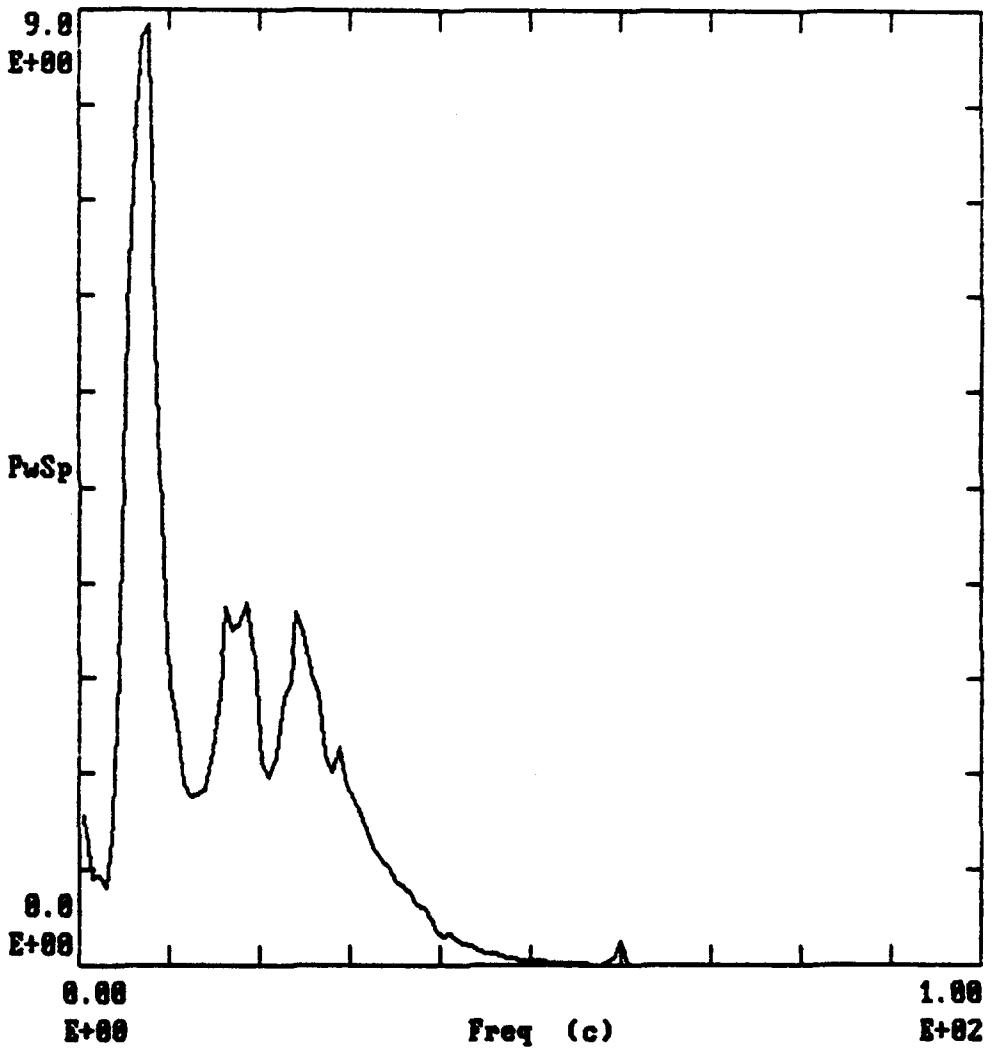


Figure 3.22 - Power spectrum of the surface curvature fluctuation in the wave region at x/d=28, y/d=12. U_e=150 cm/s, Re = 9.5×10^3, h/d=3.5.

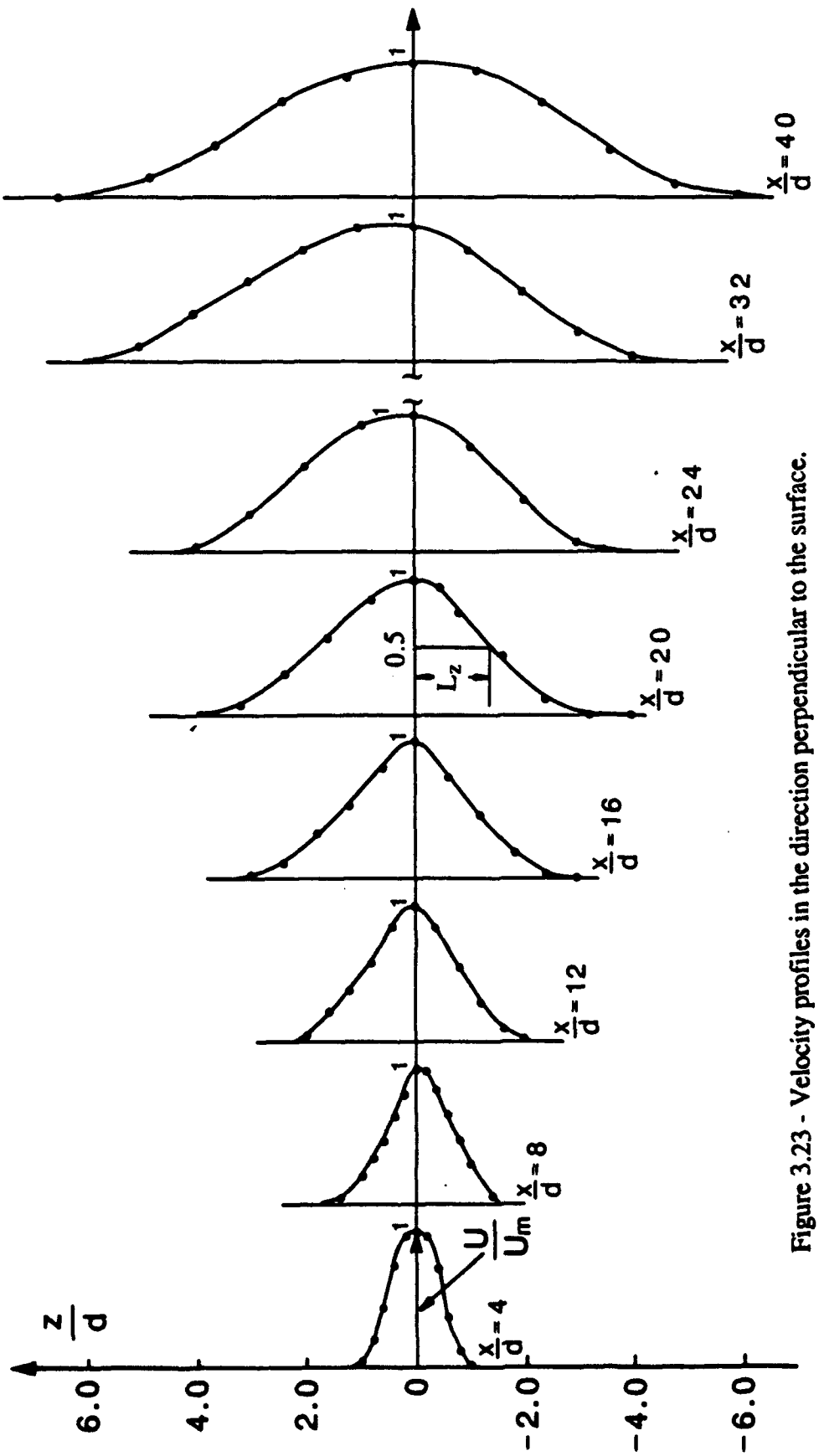


Figure 3.23 - Velocity profiles in the direction perpendicular to the surface.
U_e = 200 cm/s, Re = 1.27×10^4, h/d=24.

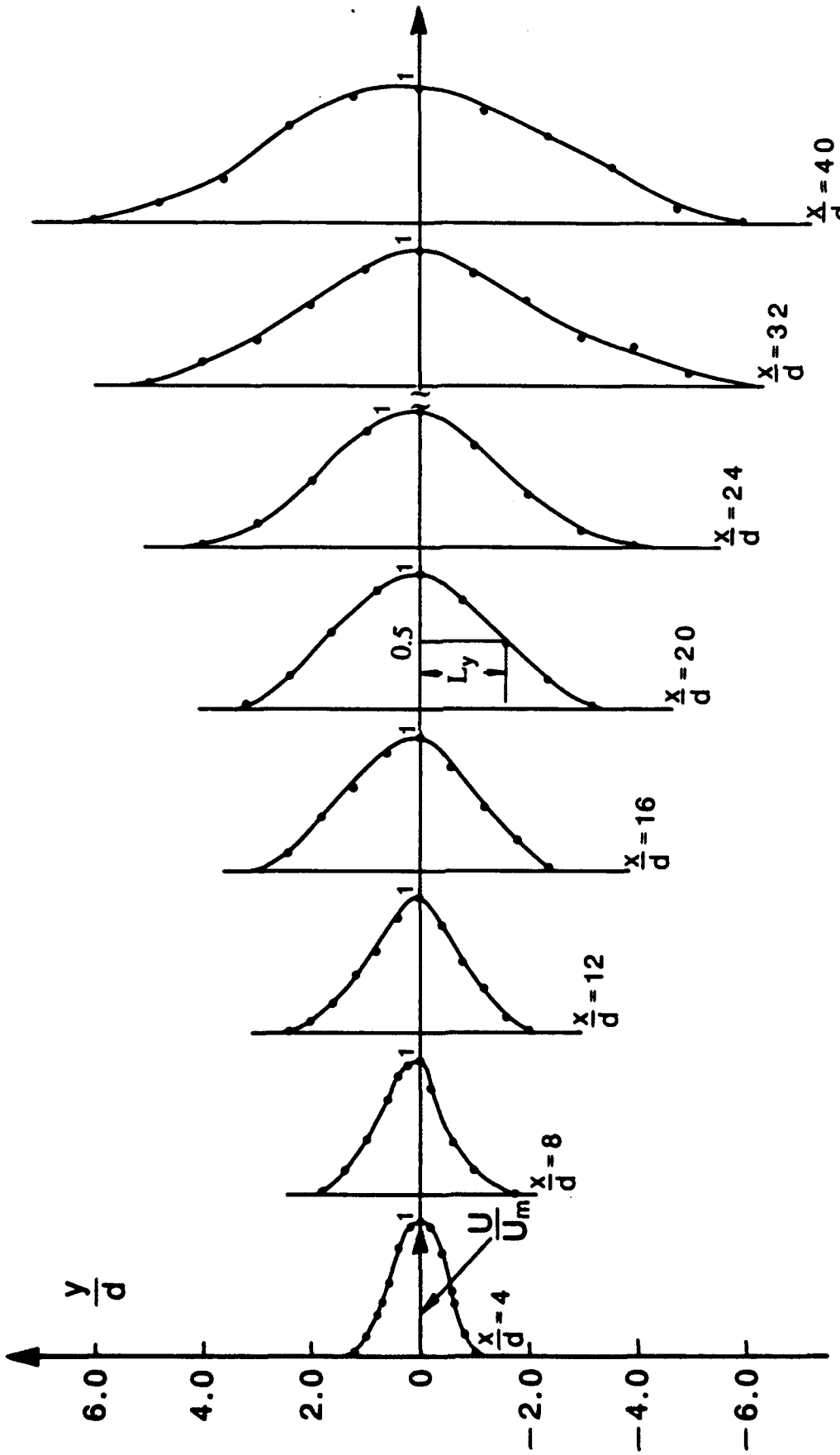


Figure 3.24 - Velocity profiles in the direction parallel to the surface.
U_e = 200 cm/s, Re = 1.27×10^4, h/d=24.

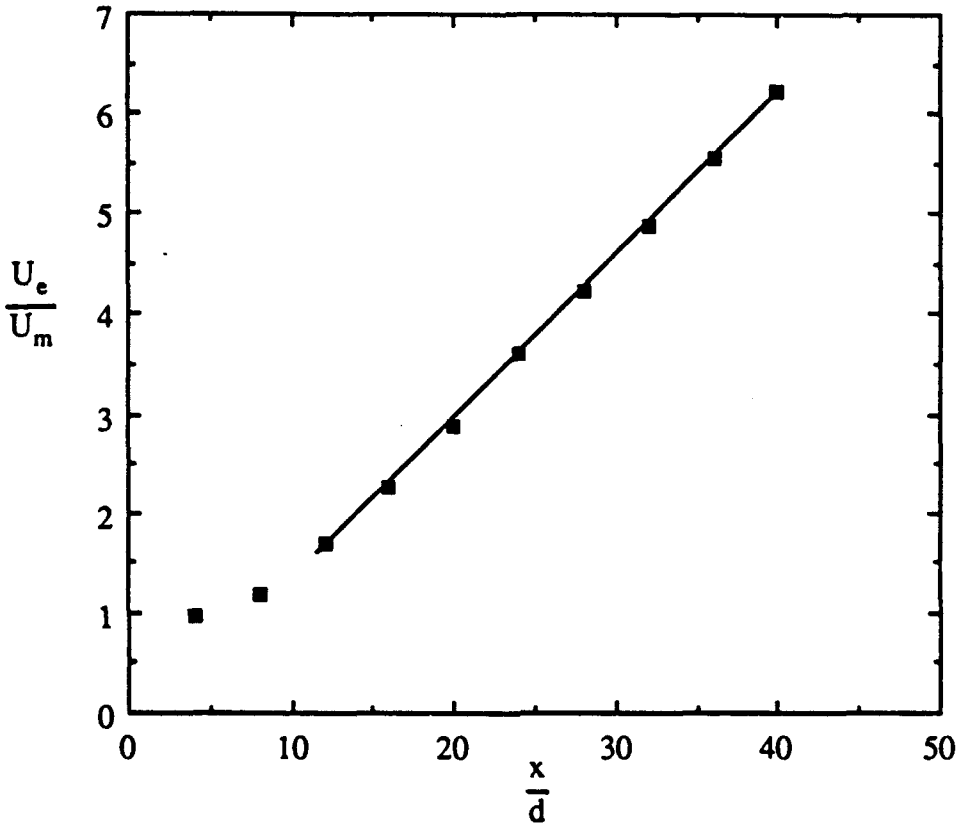


Figure 3.25 - Downstream evolution of maximum mean velocity for the free jet. ____ , least sqaures fit to the data Ue = 200 cm/s, h/d=24, Re=1.27 x 10^4.

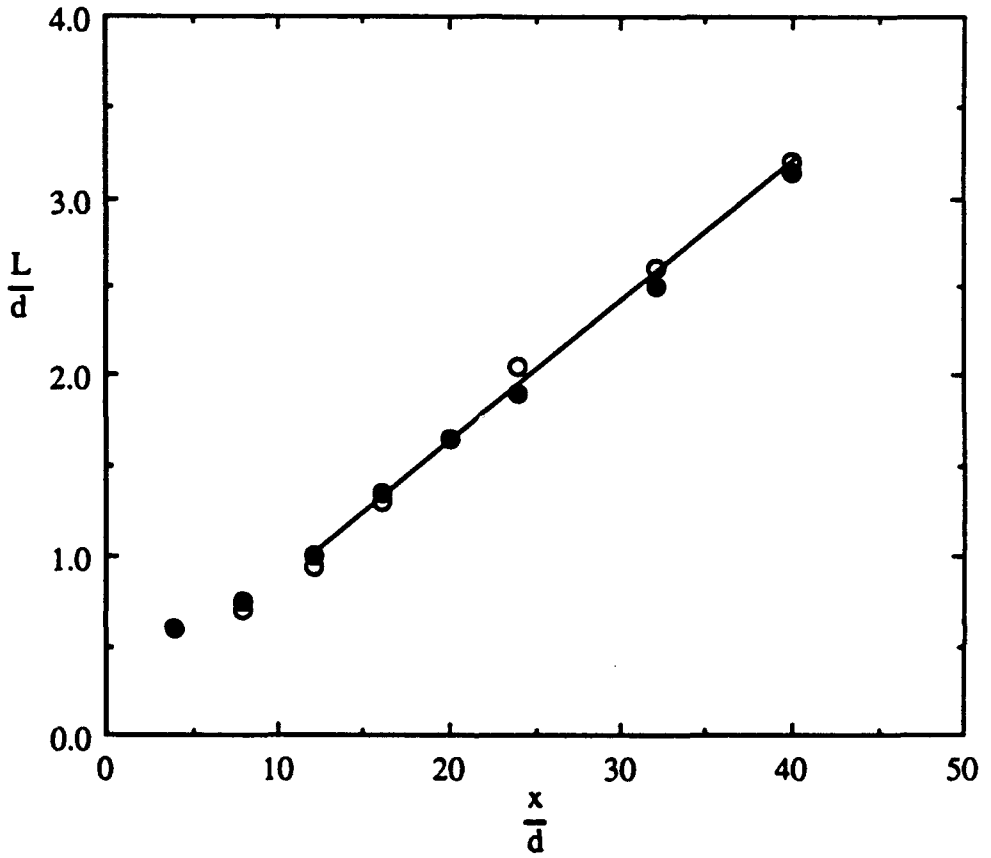


Figure 3.26 - Downstream evolution of half velocity width of the mean velocity profiles for the free jet. Solid circles, width parallel to the free surface. Open circles, width perpendicular to the free surface. ____, least squares fit to the data. Ue = 200 cm/s, Re = 1.27×10^4, h/d=24.

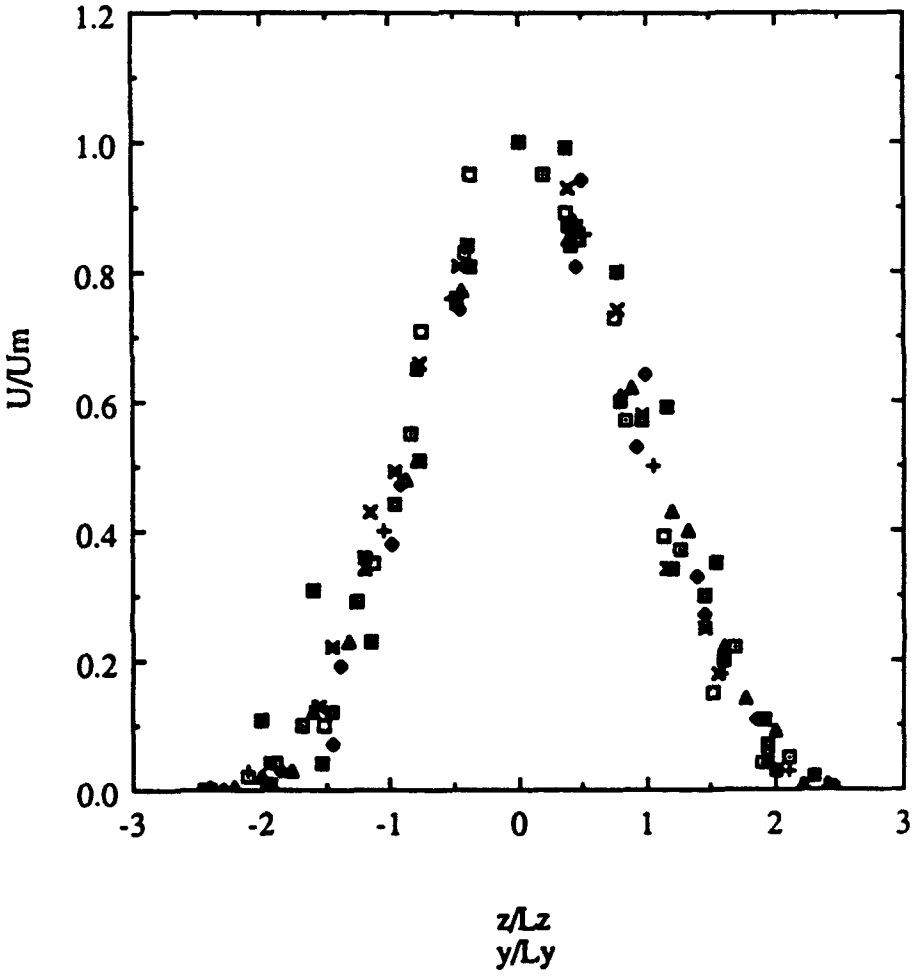


Figure 3.27 - Similarity mean velocity profiles in the y and z directions for the free jet. U_e=200 cm/s, Re=1.27x10^4, h/d=24.

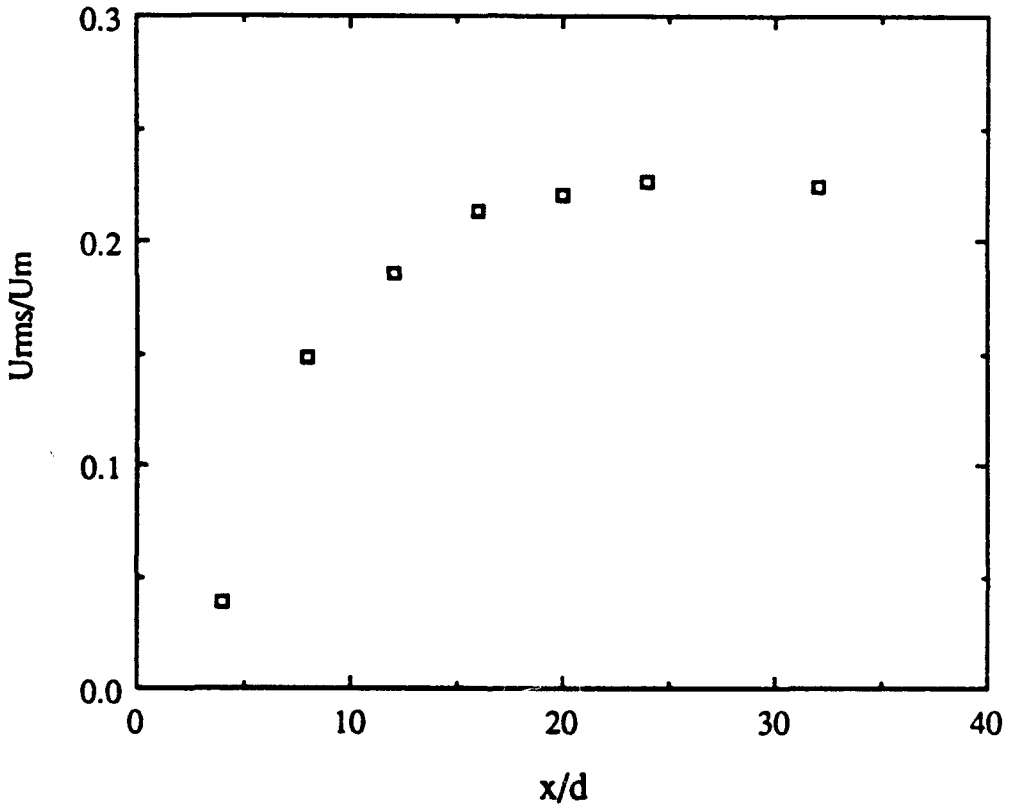


Figure 3.28 - Downstream evolution of normalized rms value of the velocity fluctuation on the jet centerline. U_e=200 cm/s, Re=1.27x10^4, h/d=24.

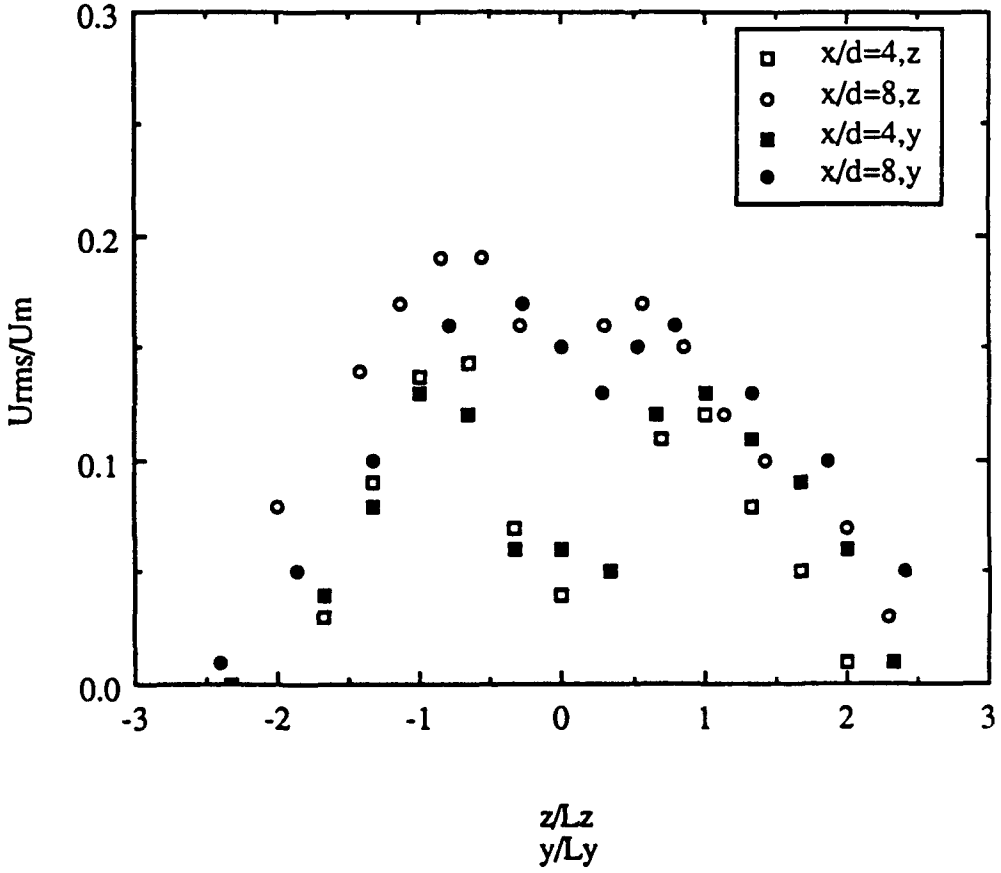


Figure 3.29 - Profiles of the rms value of the velocity fluctuation normalized by the local maximum mean velocity on the jet centerline, U_m. Open symbols vertical direction (z). Closed symbols horizontal direction (y). U_e=200 cm/s, Re=1.27x10^4, h/d=24, x/d=4, 8.

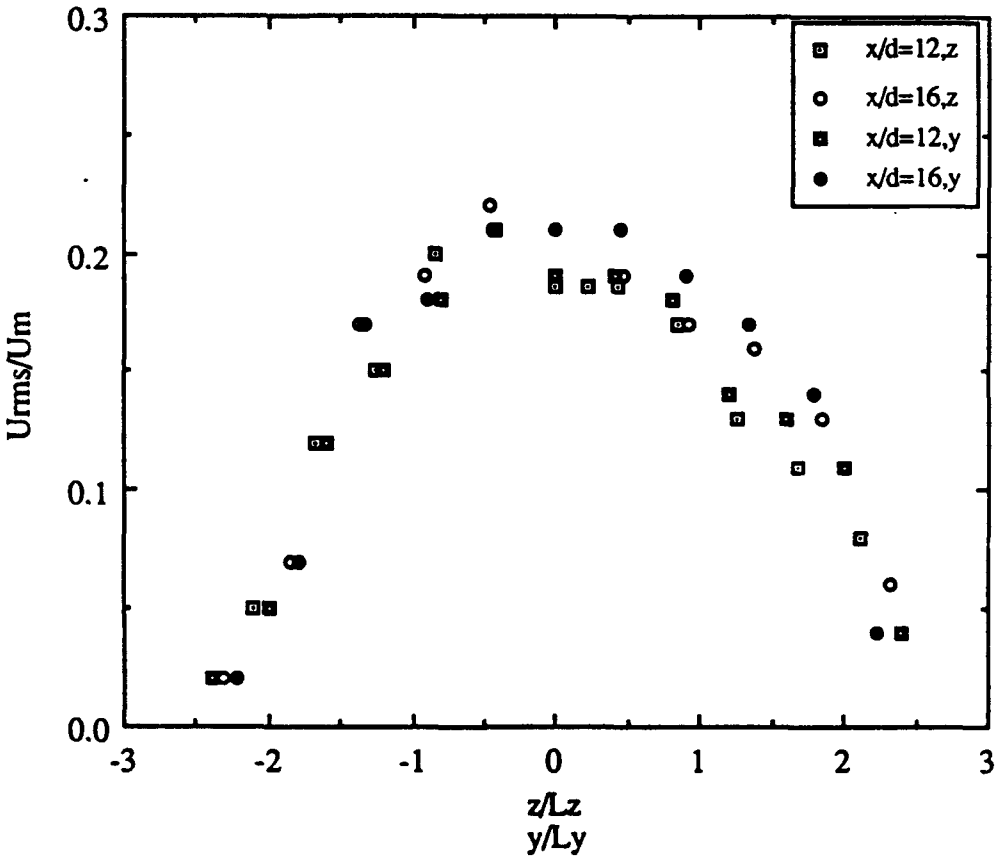


Figure 3.30 - Profiles of the rms value of the velocity fluctuation normalized by the local maximum mean velocity on the jet centerline, U_m. Open symbols vertical direction (z). Closed symbols horizontal direction (y). U_c=200 cm/s, Re=1.27x10^4, h/d=24, x/d=12, 16.

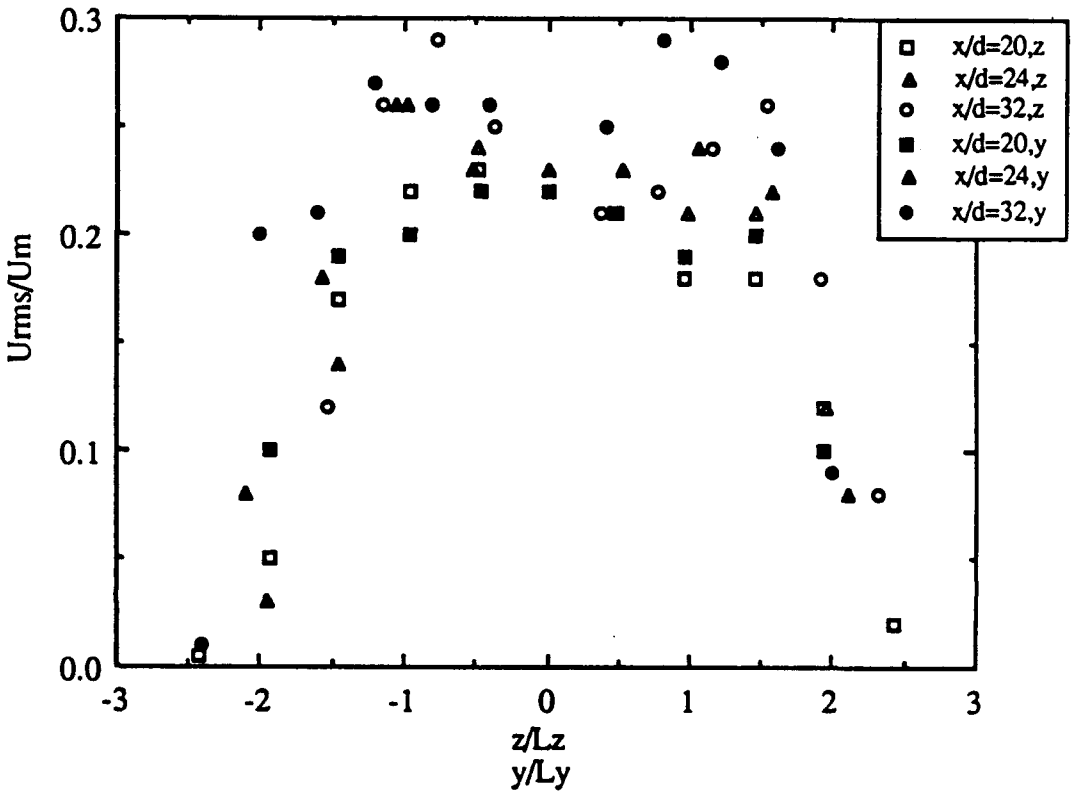


Figure 3.31 - Profiles of the rms value of the velocity fluctuation normalized by the local maximum mean velocity on the jet centerline, U_m. Open symbols vertical direction (z). Closed symbols horizontal direction (y). U_e=200 cm/s, Re=1.27x10^4, h/d=24, x/d=20, 24, 32.

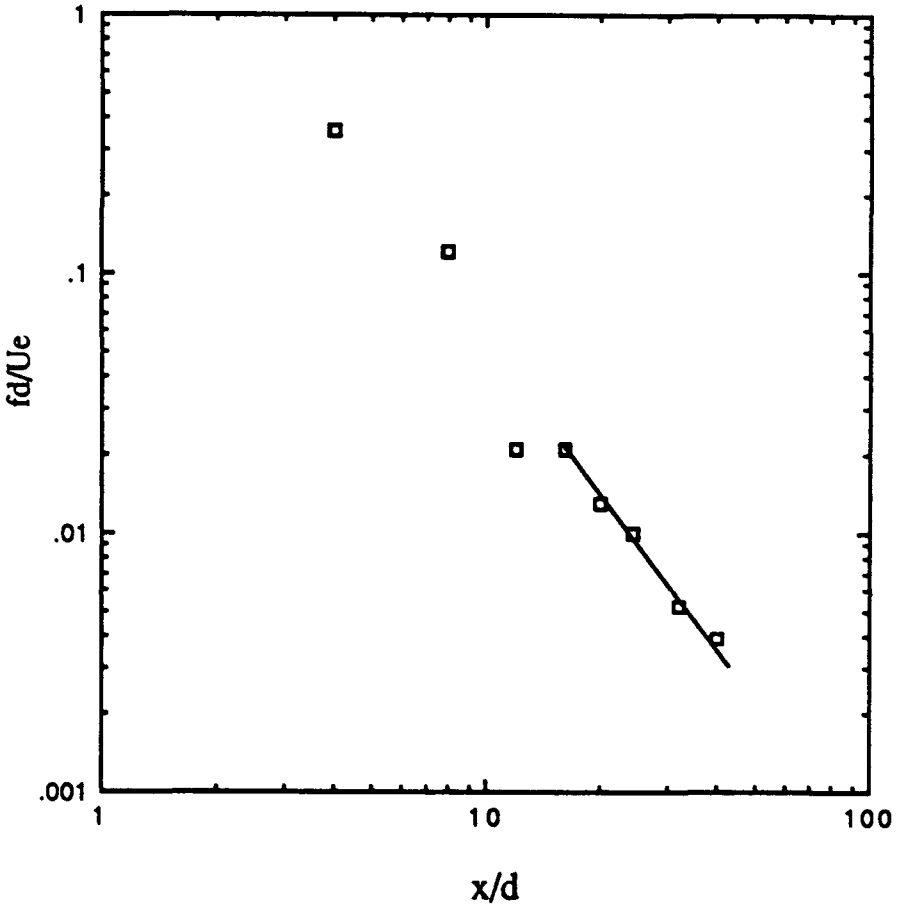


Figure 3.32 - Downstream evolution of the normalized frequency of the velocity fluctuations along the jet centerline. Straight line is a least squares fit to the data for x/d≥12. Slope = -2. U_e=200 cm/s,Re=1.27x10^4, h/d=24.

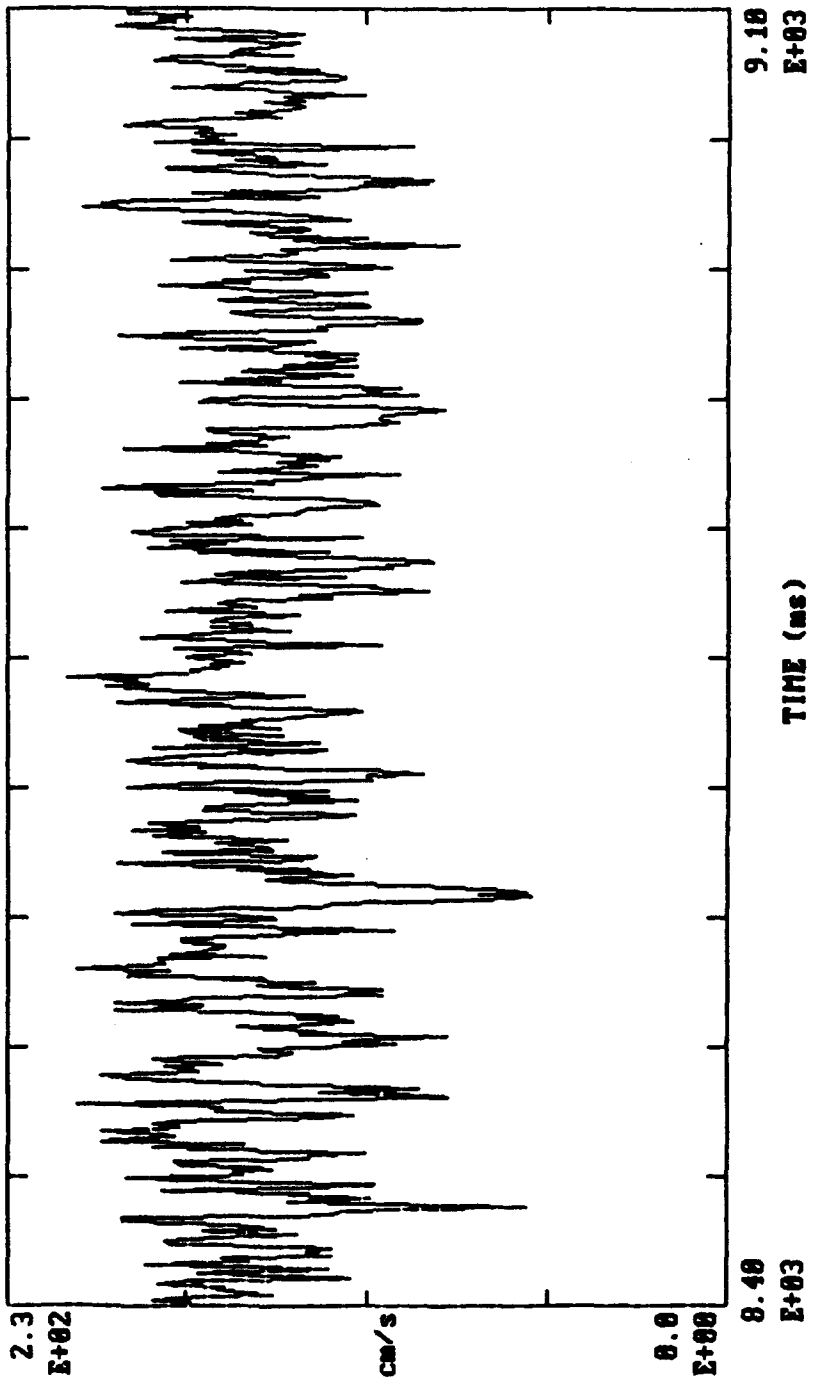


Figure 3.33 - Time trace of the calibrated hot film velocity signal along the jet centerline at x/d=8. U_e = 200 cm/s, Umean = 157.4 cm/s, U_{rms} = 27.25 cm/s, Re = 1.27×10^4, h/d=1.

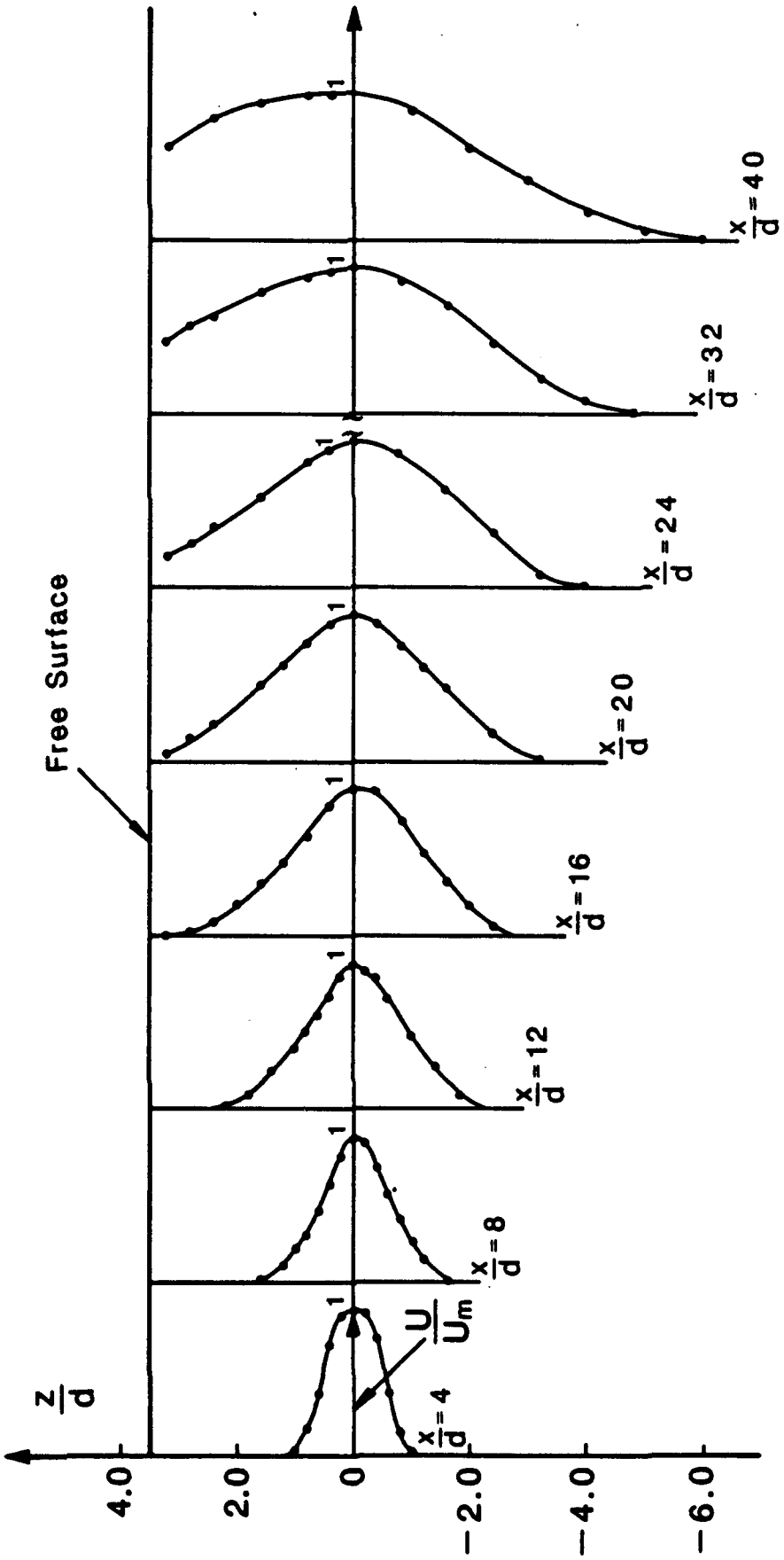


Figure 3.34 - Velocity profiles in the direction perpendicular to the surface.
U_e = 200 cm/s, Re = 1.27x10^4, h/d=3.5.

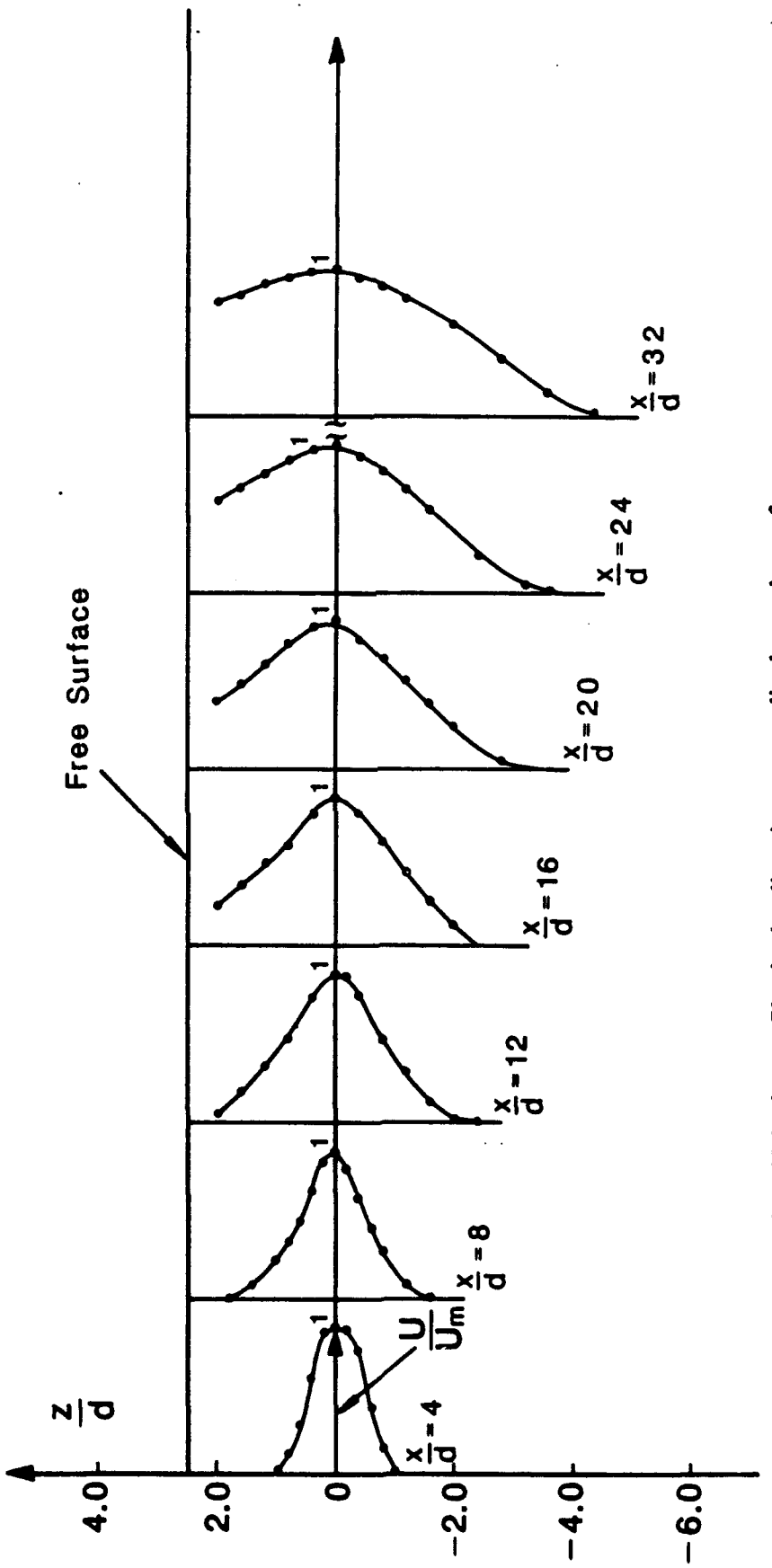


Figure 3.35 - Velocity profiles in the direction perpendicular to the surface.
U_e = 200 cm/s, Re = 1.27×10^4, h/d=2.5.

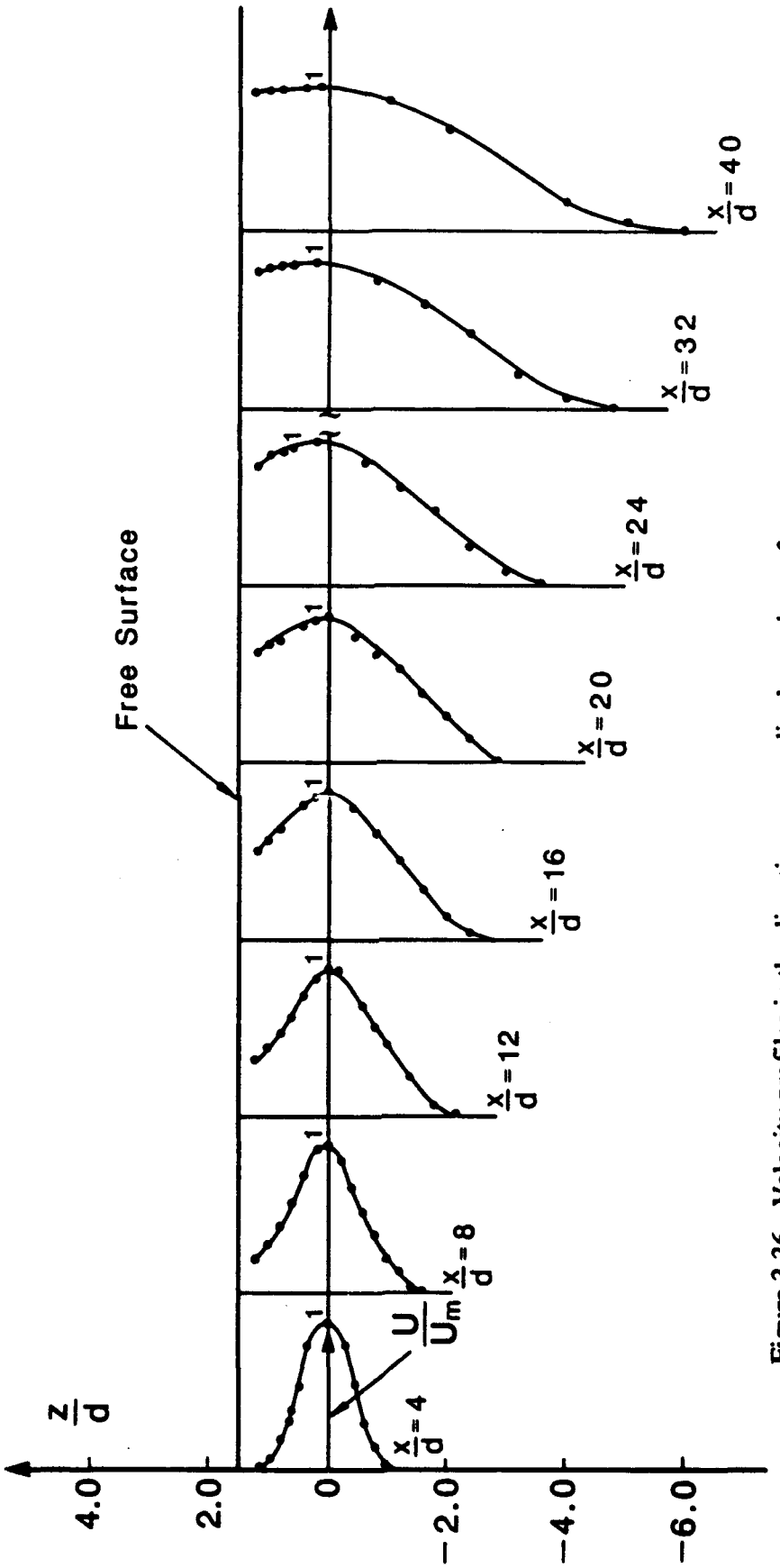


Figure 3.36 - Velocity profiles in the direction perpendicular to the surface.
U_e = 200 cm/s, Re = 1.27×10^4, h/d=1.5.

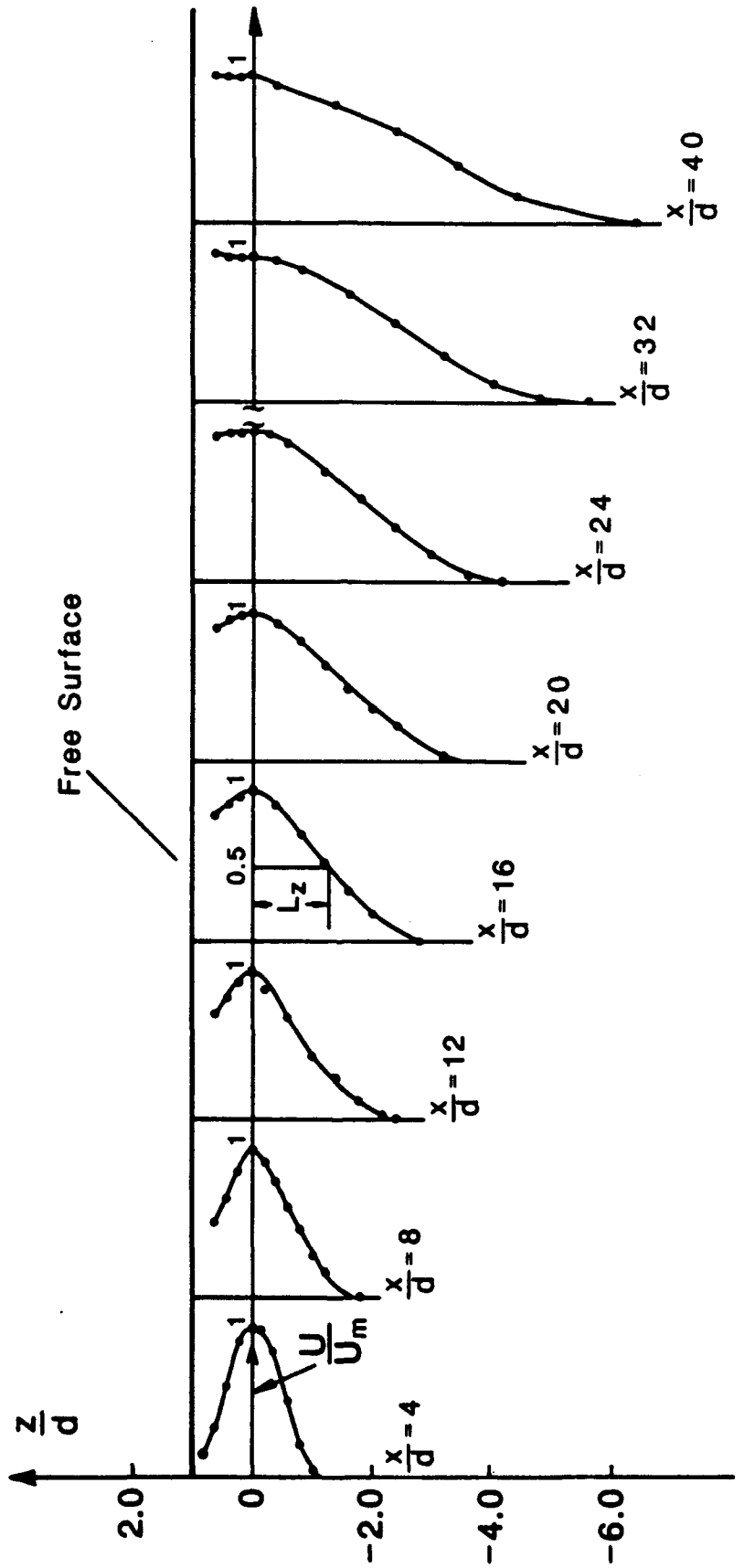


Figure 3.37 - Velocity profiles in the direction perpendicular to the surface.
U_e = 200 cm/s, Re = 1.27×10^4, h/d=1.

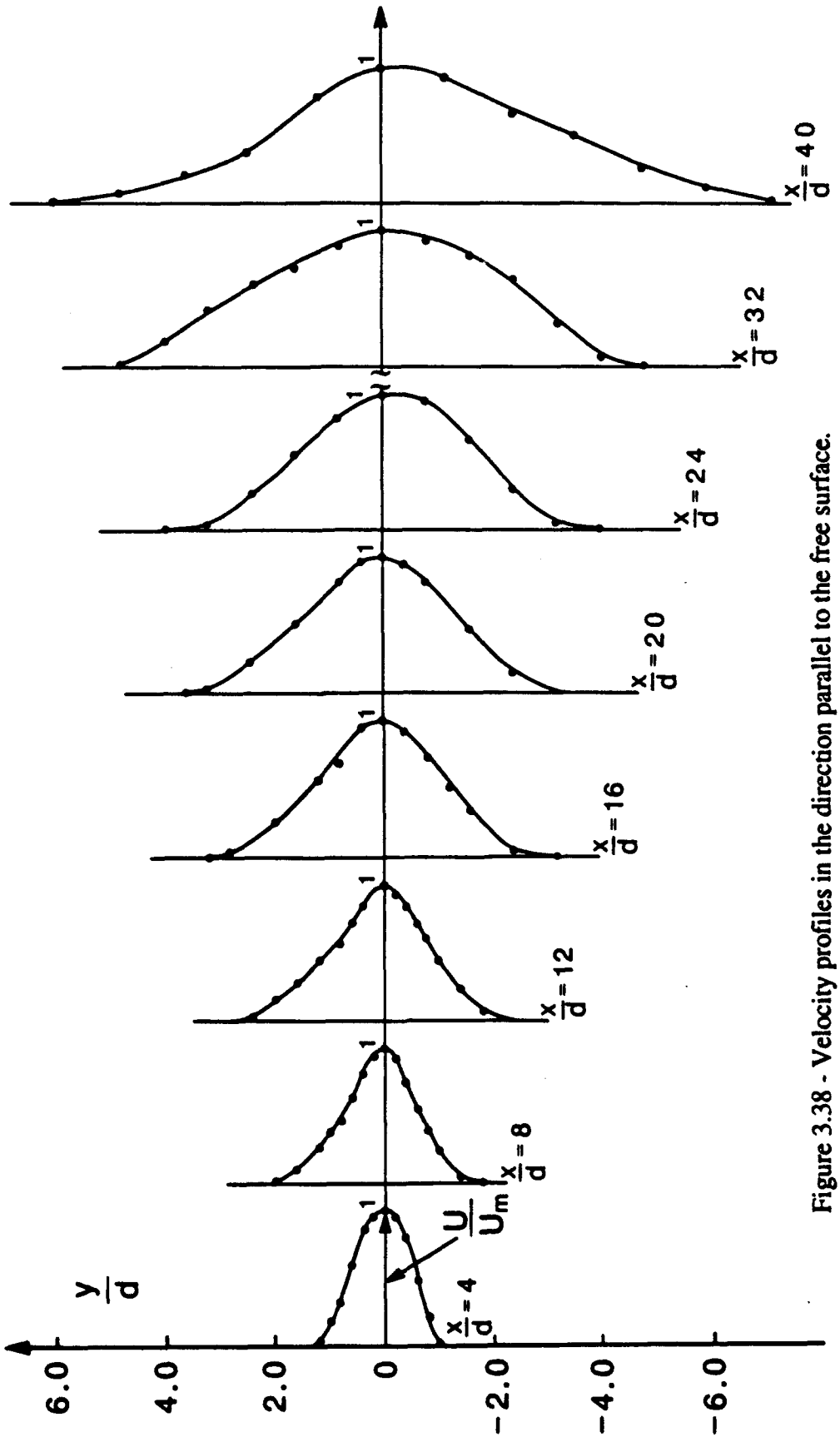


Figure 3.38 - Velocity profiles in the direction parallel to the free surface.
U_e = 200 cm/s, Re = 1.27×10^4, h/d=3.5.

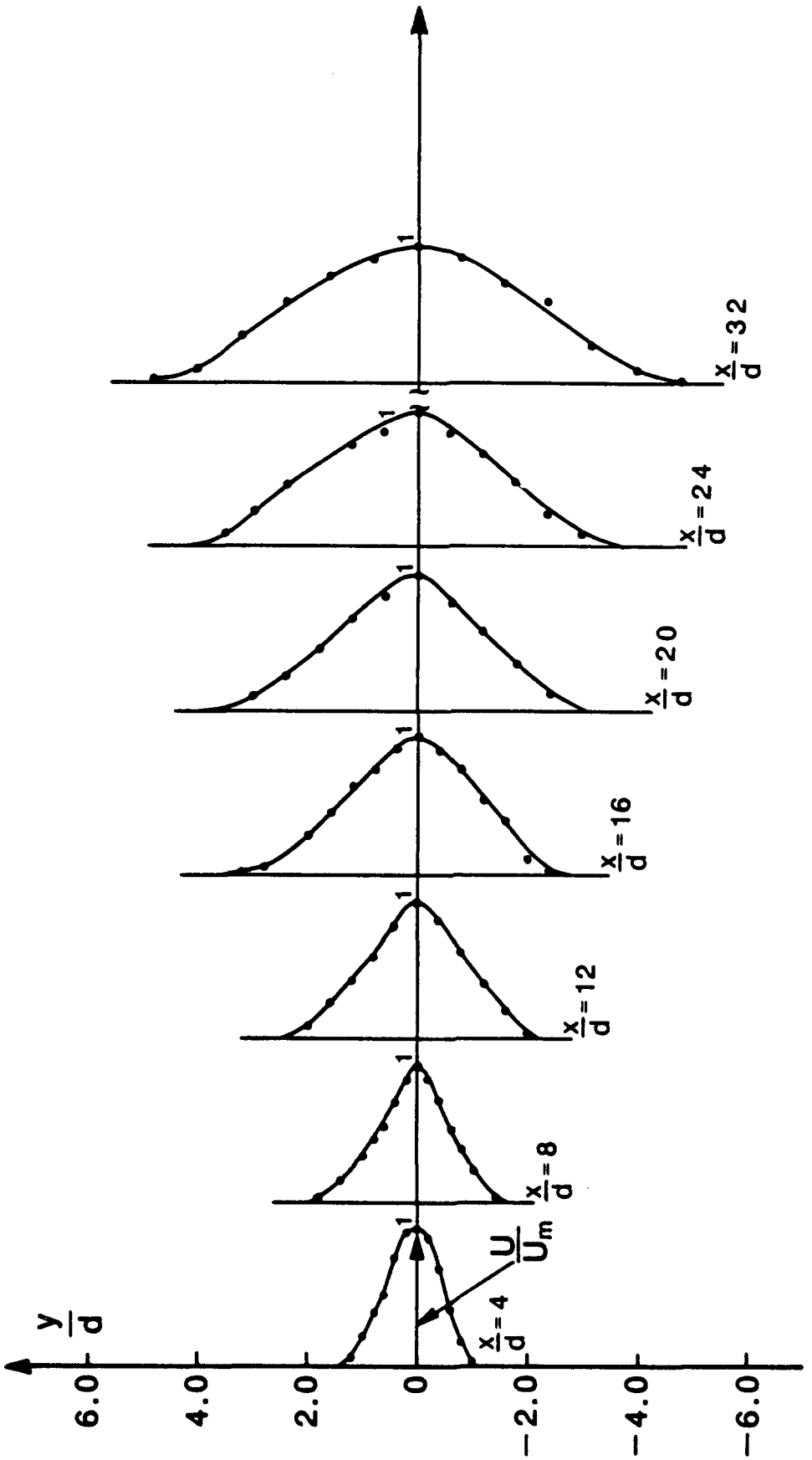


Figure 3.39 - Velocity profiles in the direction parallel to the free surface.
U_e = 200 cm/s, Re = 1.27×10^4, h/d=2.5.

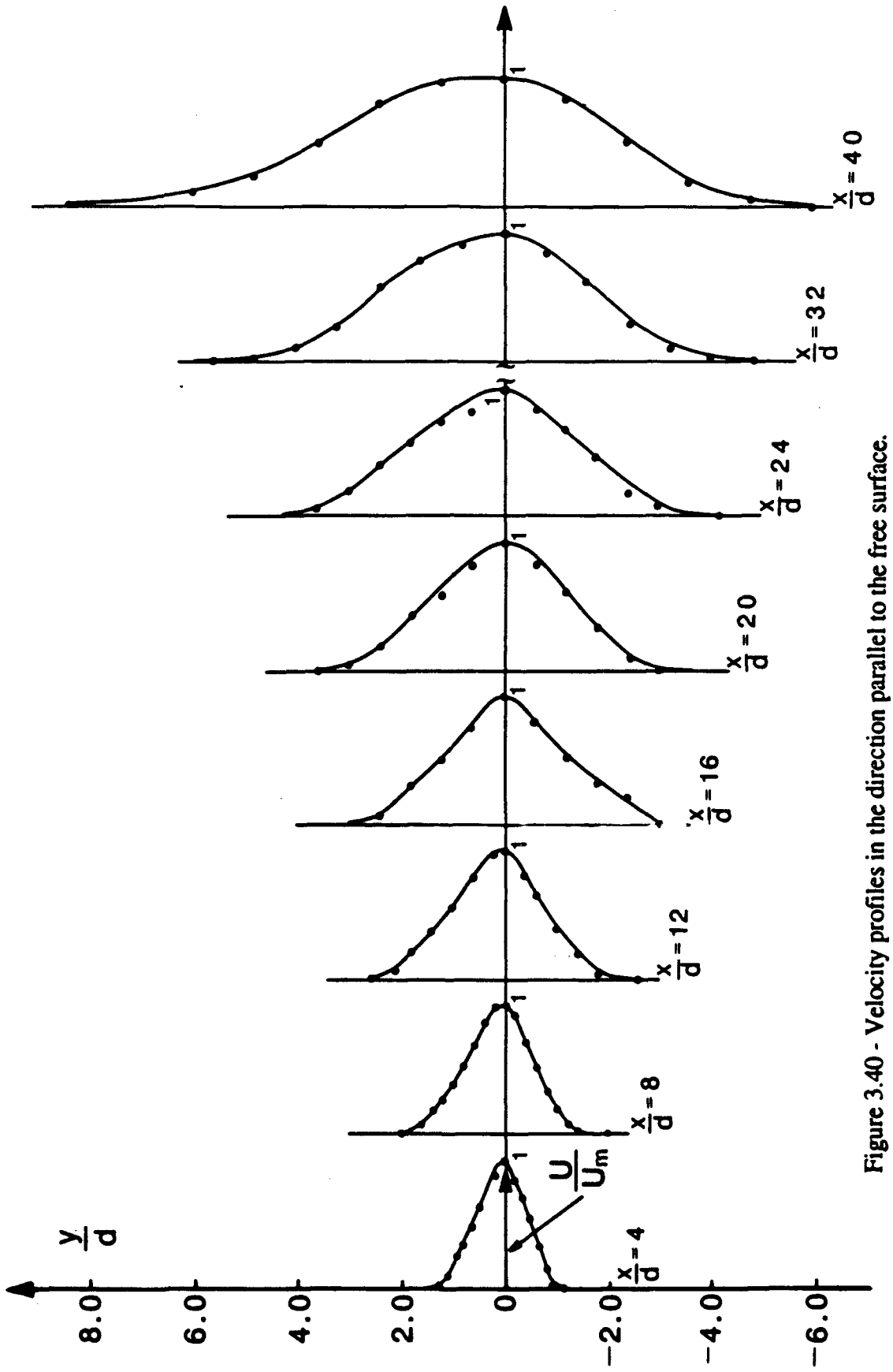


Figure 3.40 - Velocity profiles in the direction parallel to the free surface.
U_e = 200 cm/s, Re = 1.27×10^4, h/d=1.5.

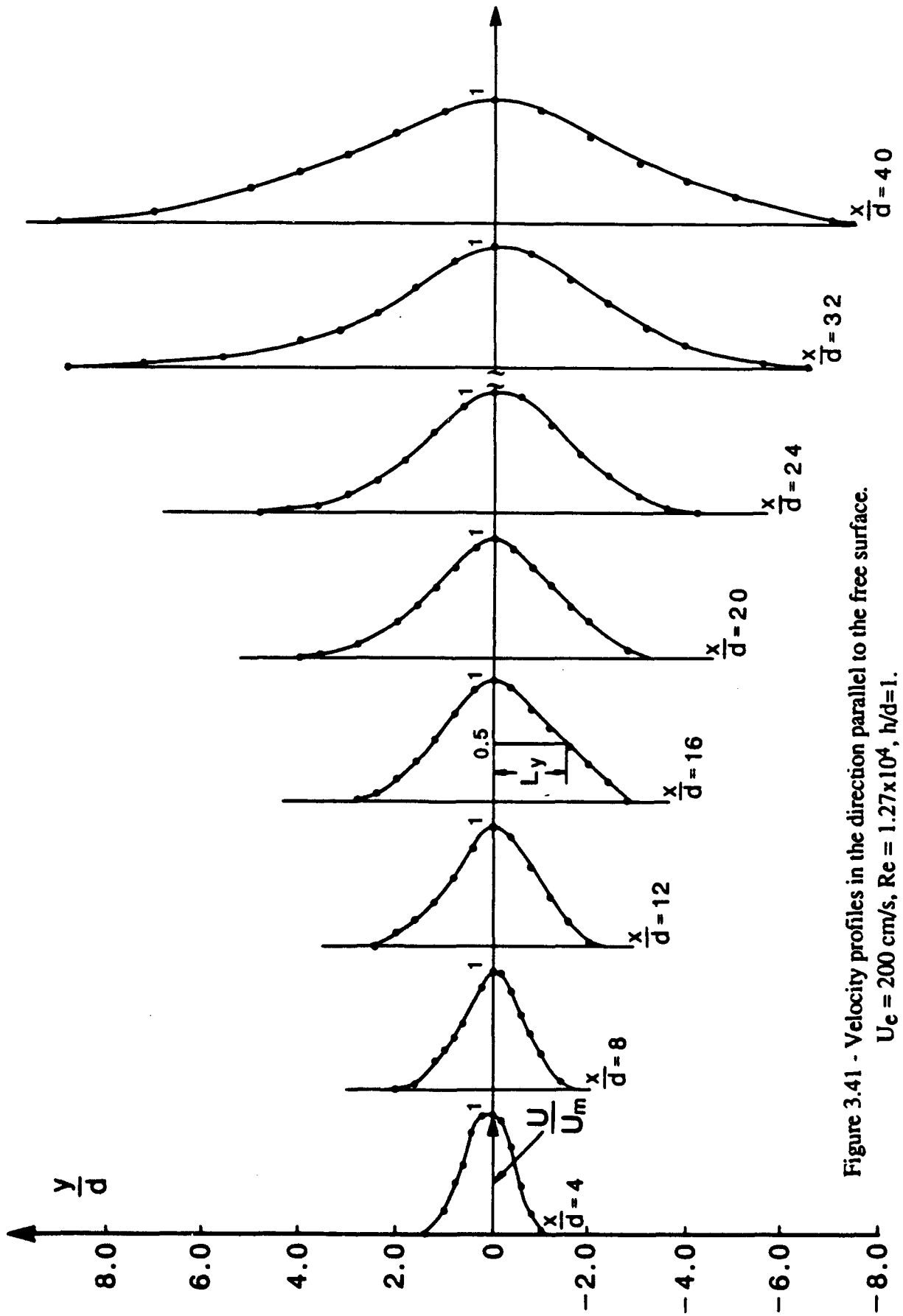


Figure 3.41 - Velocity profiles in the direction parallel to the free surface.
U_e = 200 cm/s, Re = 1.27×10^4, h/d=1.

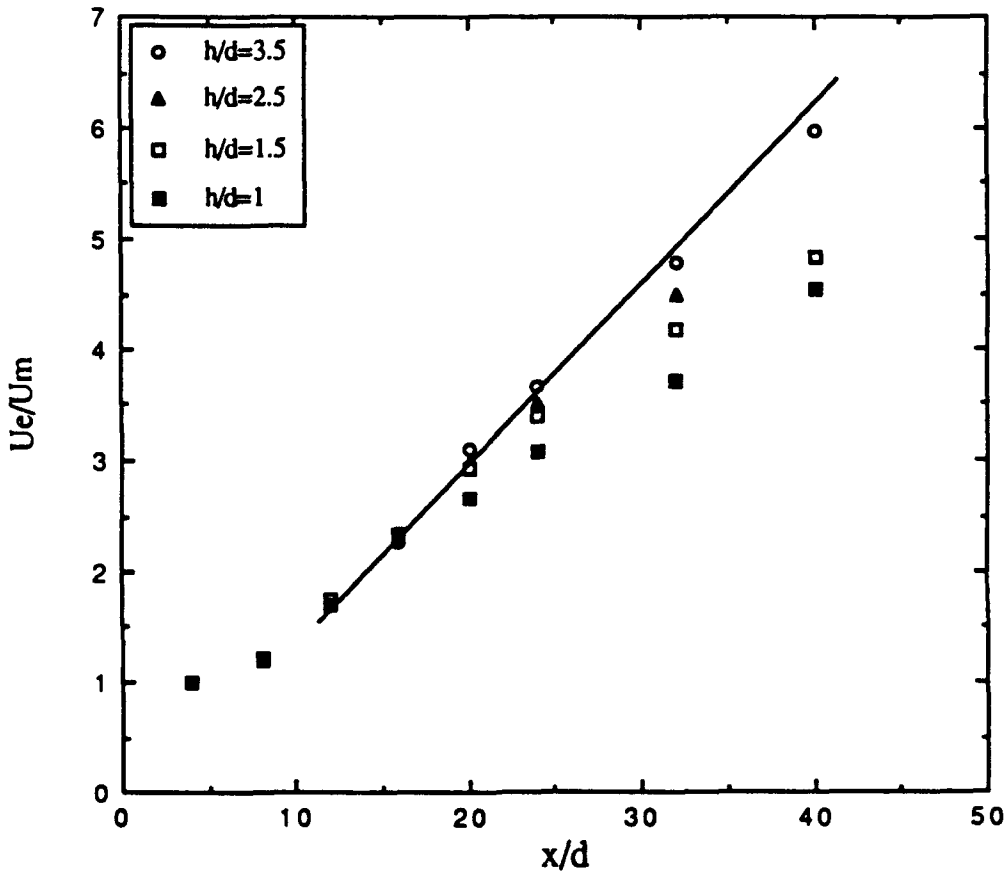


Figure 3.42 - Downstream evolution of maximum mean velocity for the free-surface jet. ___, least squares linear fit to the free jet data. U_e=200 cm/s, Re=1.27x10^4.

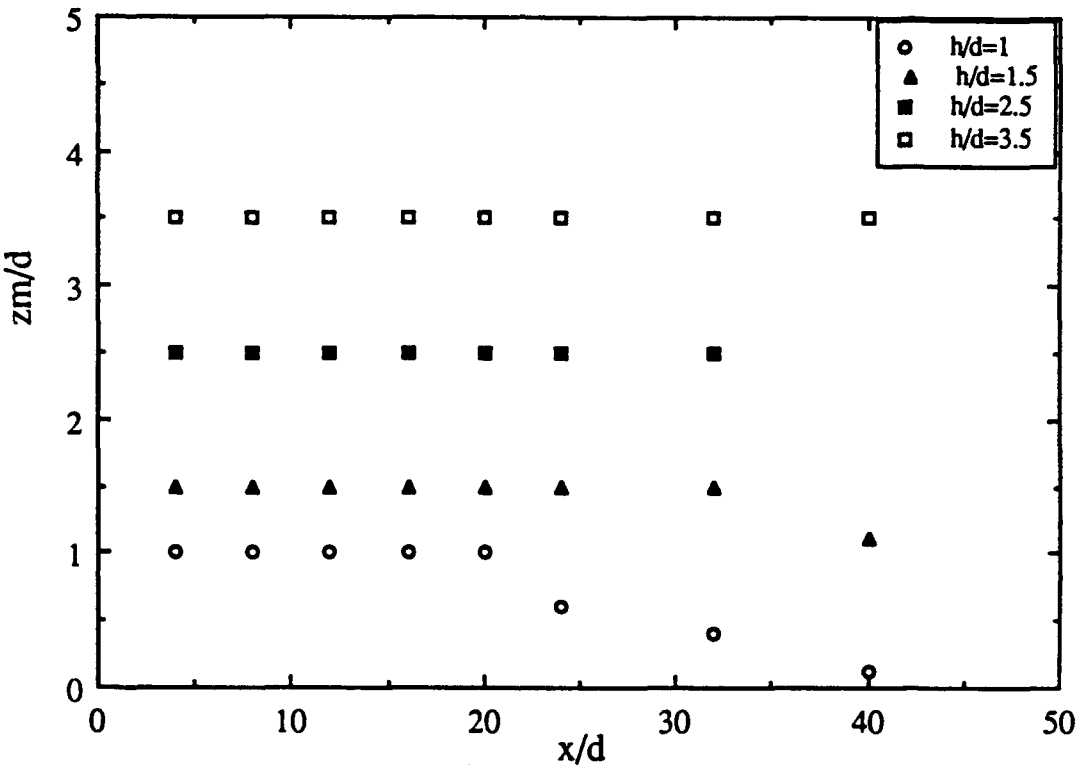


Figure 3.43 - Location of the maximum mean velocity as a function of x/d. U_e=200 cm/s, Re=1.27x10^4.

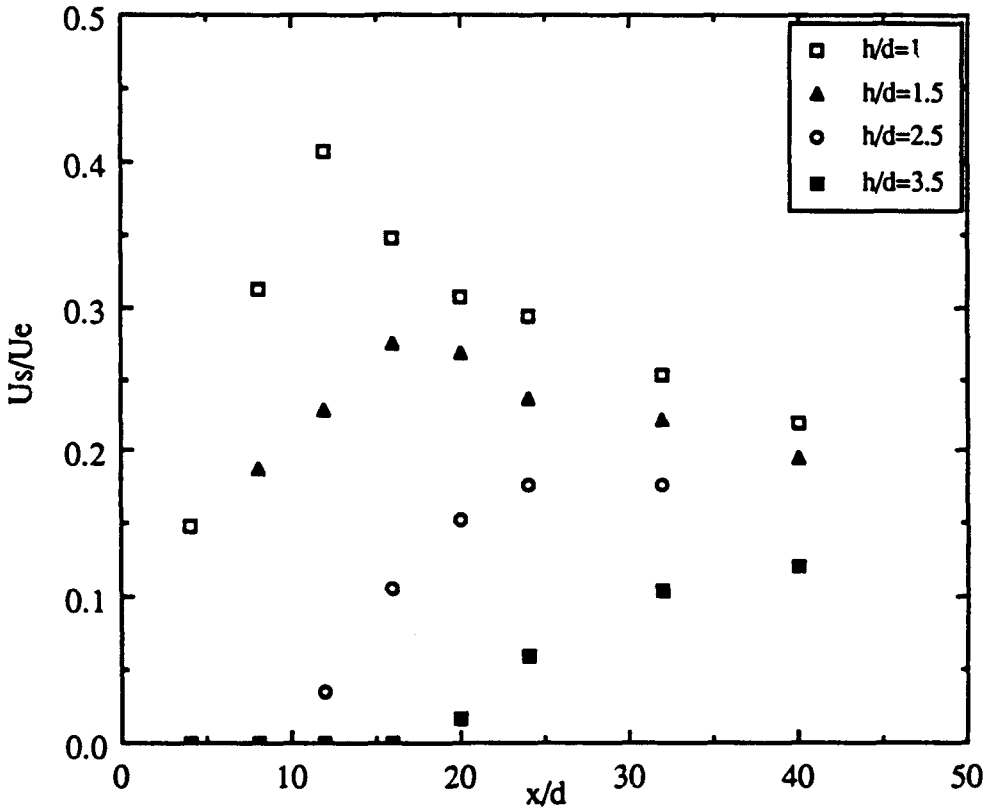


Figure 3.44 - Downstream evolution of the surface velocity normalized by the jet exit velocity U_e. U_e=200 cm/s, Re=1.27x10^4.

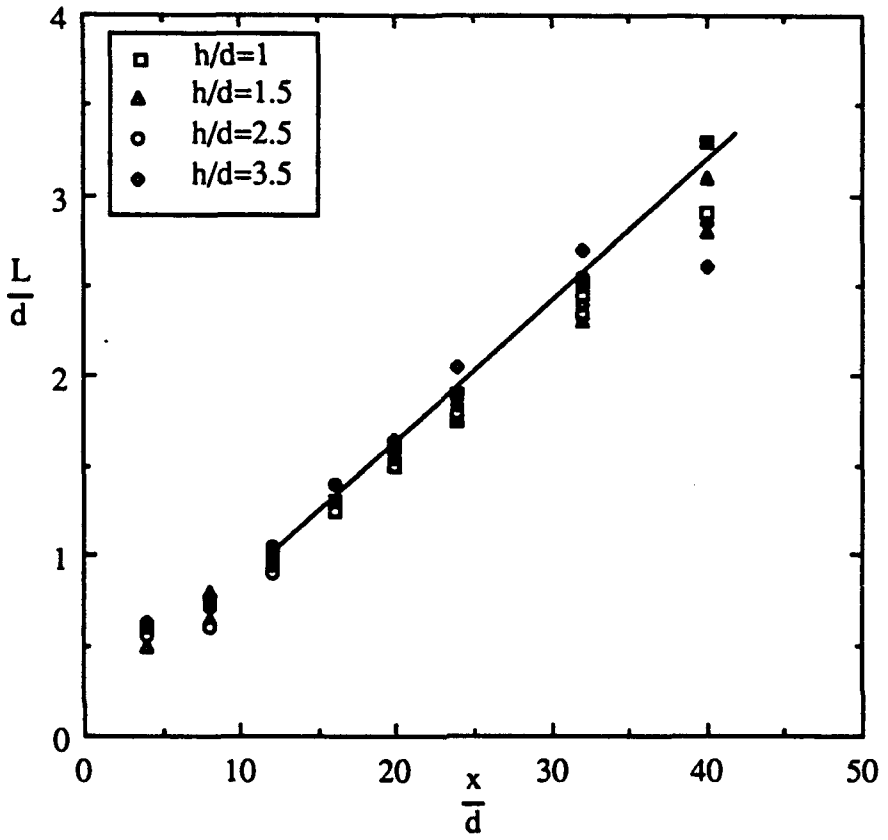


Figure 3.45 - Downstream evolution of the half velocity width of the mean velocity profiles. Solid symbols, width parallel to the free surface. Open symbols, width perpendicular to the free surface. ____ , least squares fit to the data for h/d=24. Ue=200 cm/s, Re = 1.27×10^4.

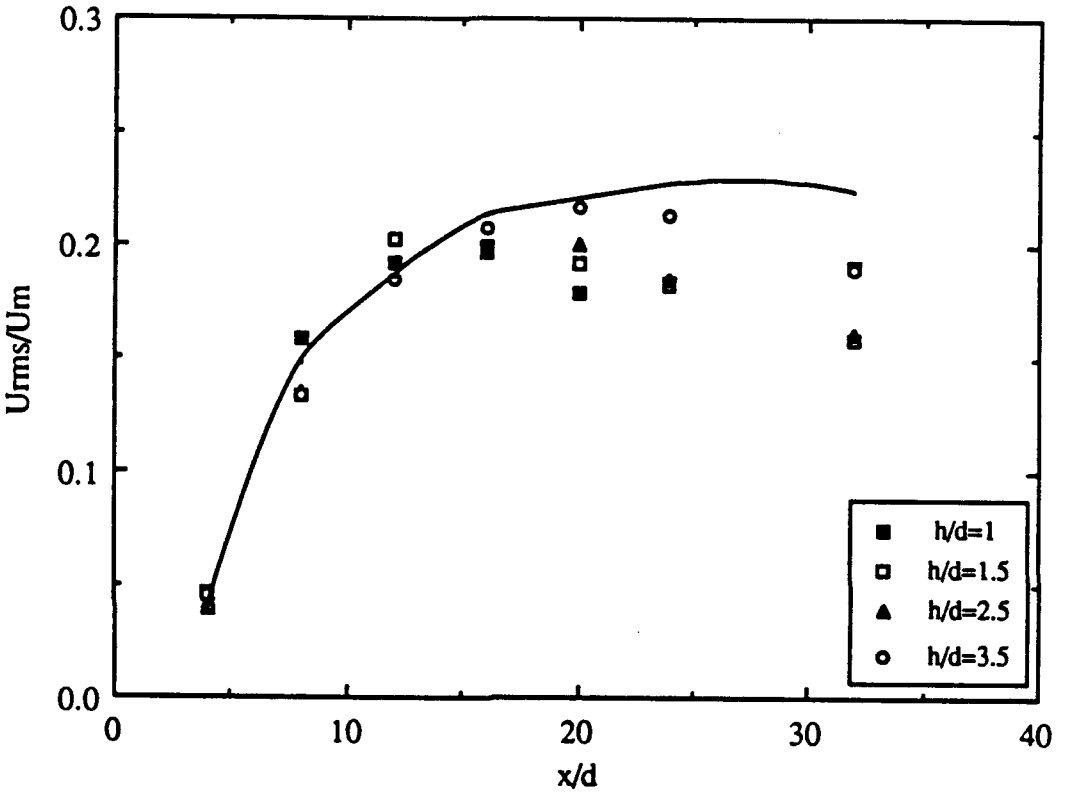


Figure 3.46 - Downstream evolution of normalized rms value of the velocity fluctuation on the jet centerline. Solid curve represents the free jet data. U_e=200 cm/s, Re=1.27x10^4.

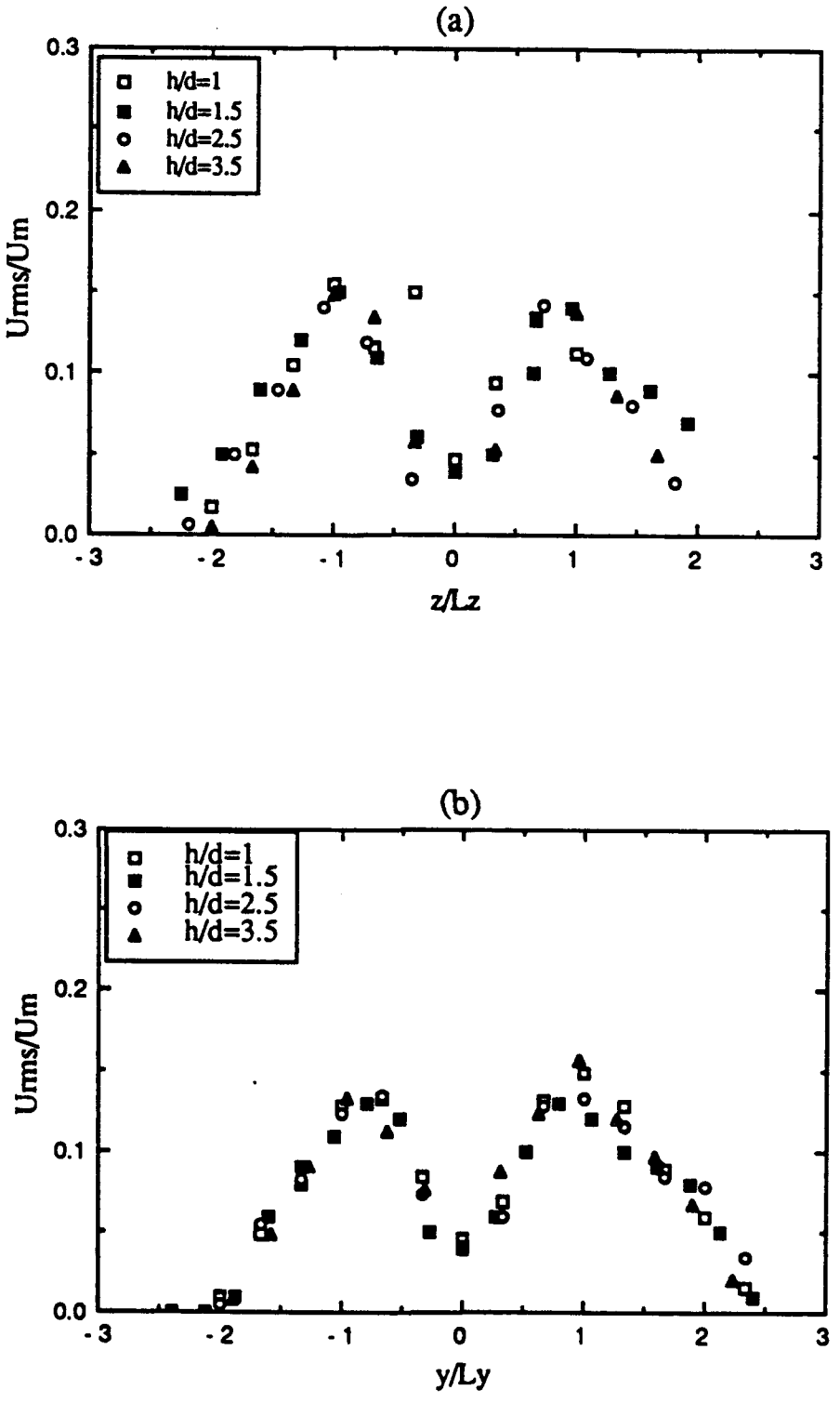


Figure 3.47 - Profiles of the rms value of the velocity fluctuation normalized by the local maximum mean velocity. Plot (a) profiles perpendicular to the free surface. Plot (b) profiles parallel to the free surface. U_e=200 cm/s, Re=1.27x10^4, x/d=4.

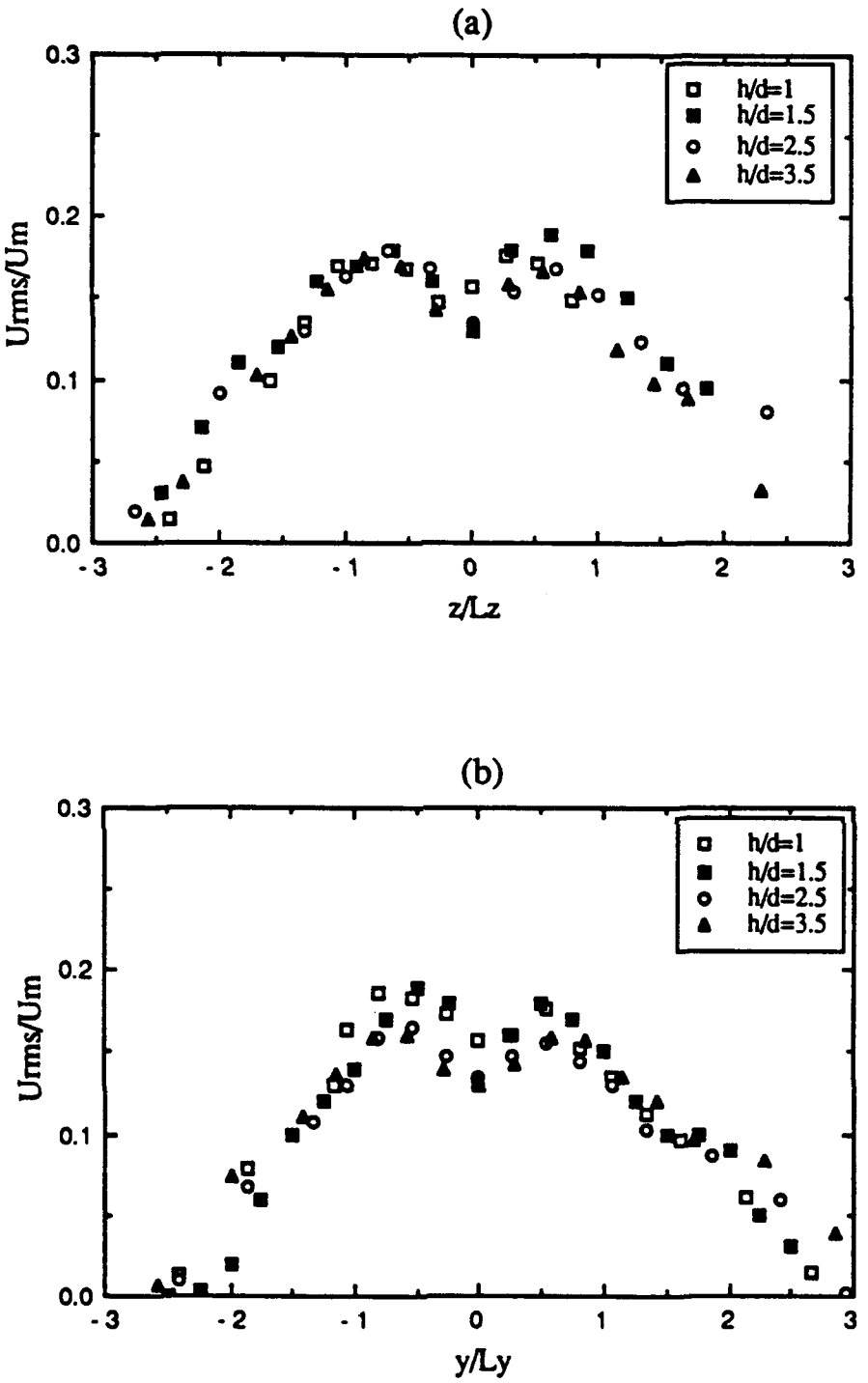
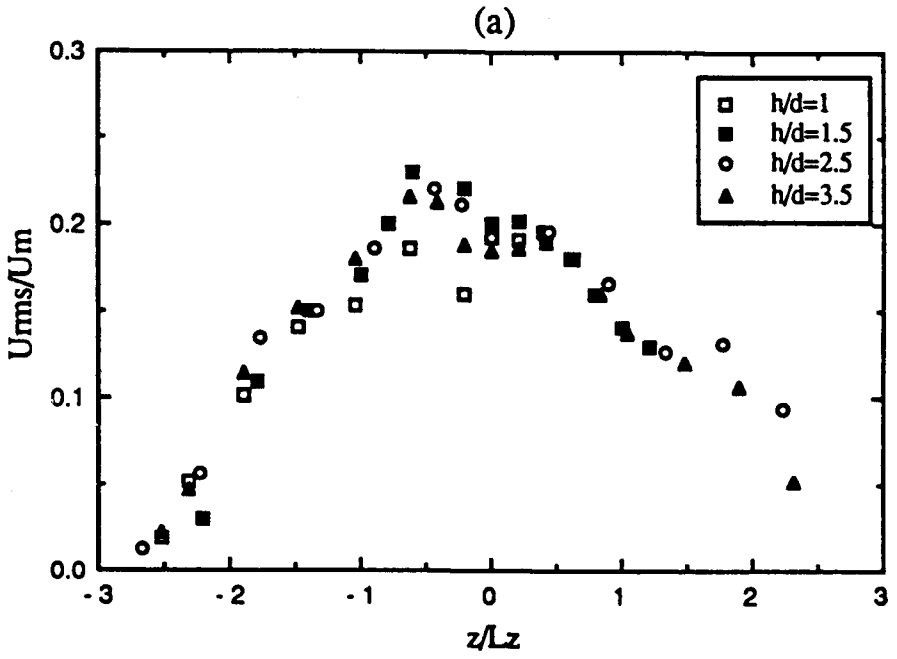


Figure 3.48 - Profiles of the rms value of the velocity fluctuation normalized by the local maximum mean velocity. Plot (a) profiles perpendicular to the free surface. Plot (b) profiles parallel to the free surface. U_e=200 cm/s, Re=1.27x10^4, x/d=8.



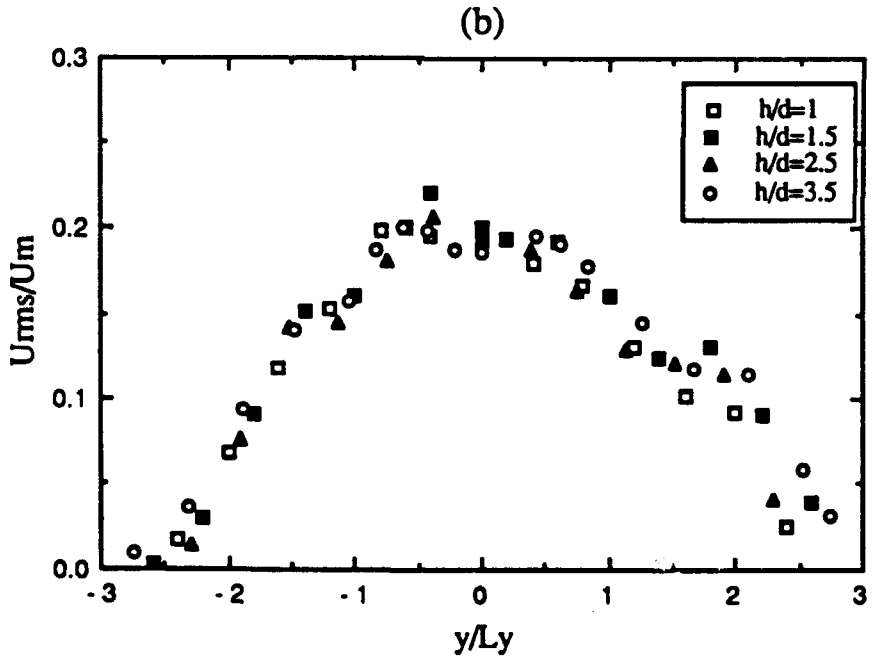


Figure 3.49 - Profiles of the rms value of the velocity fluctuation normalized by the local maximum mean velocity. Plot (a) profiles perpendicular to the free surface. Plot (b) profiles parallel to the free surface. U_e=200 cm/s, Re=1.27x10^4, x/d=12.

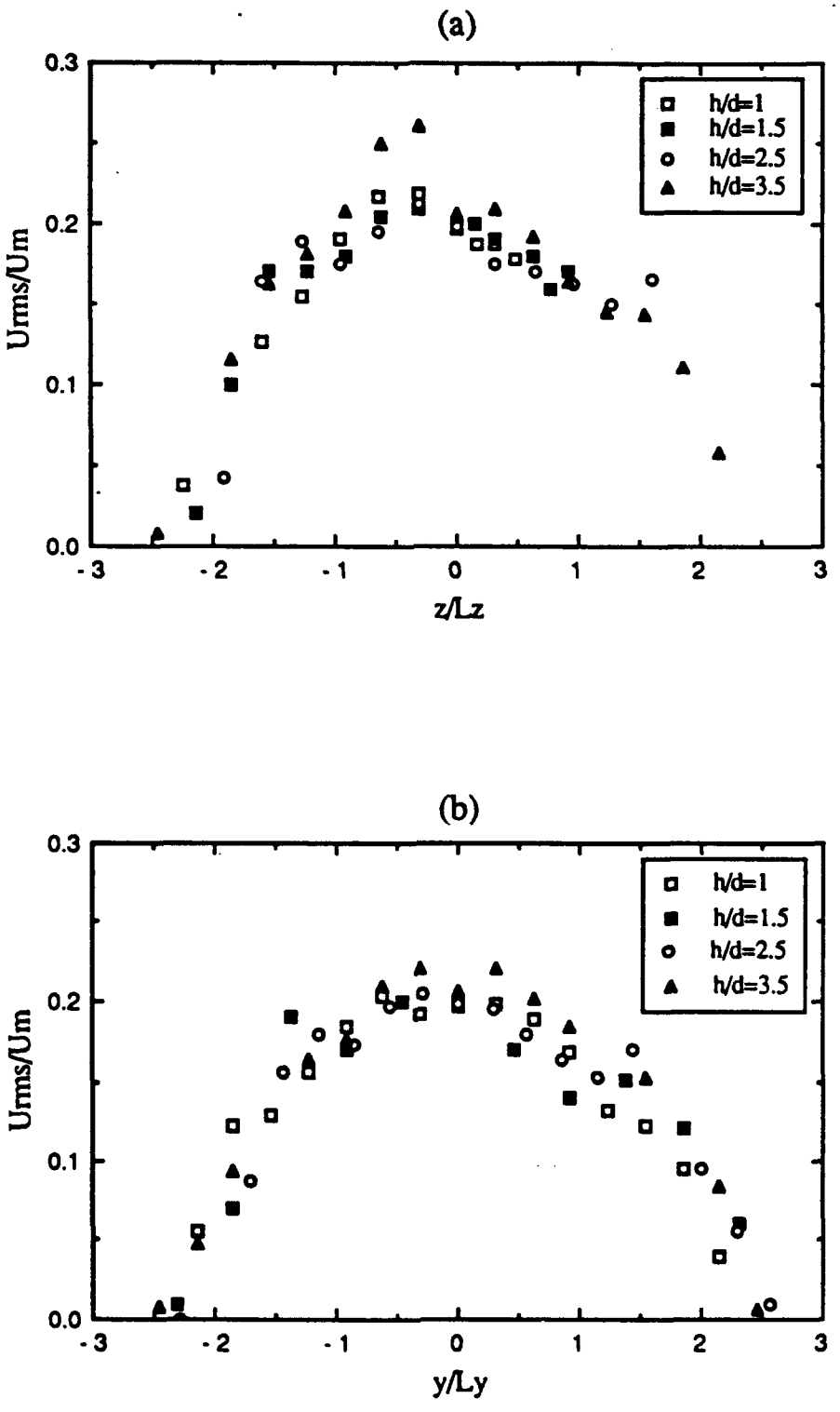


Figure 3.50 - Profiles of the rms value of the velocity fluctuation normalized by the local maximum mean velocity. Plot (a) profiles perpendicular to the free surface. Plot (b) profiles parallel to the free surface. U_e=200 cm/s, Re=1.27x10^4, x/d=16.

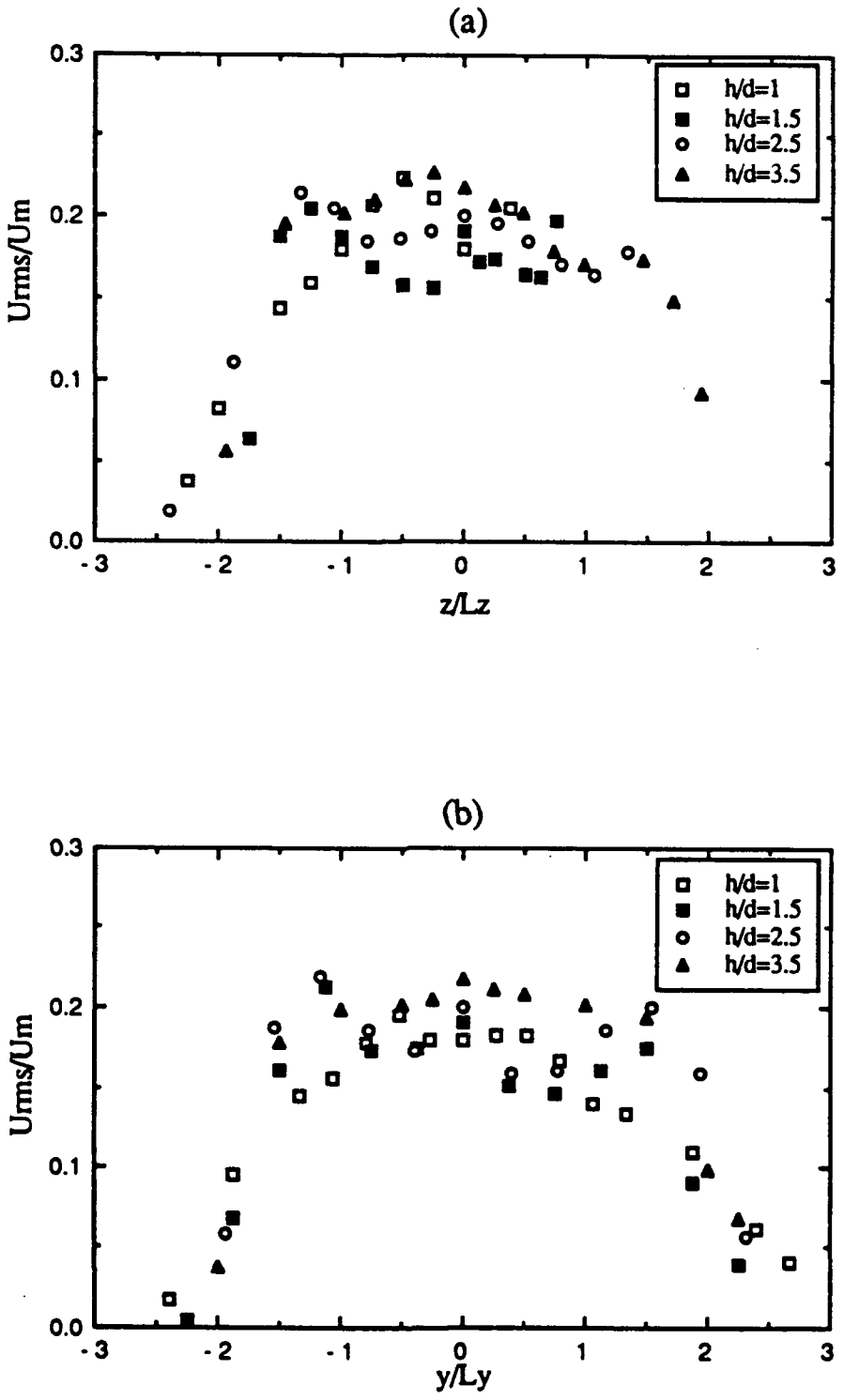


Figure 3.51 - Profiles of the rms value of the velocity fluctuation normalized by the local maximum mean velocity. Plot (a) profiles perpendicular to the free surface. Plot (b) profiles parallel to the free surface. U_e=200 cm/s, Re=1.27x10^4, x/d=20.

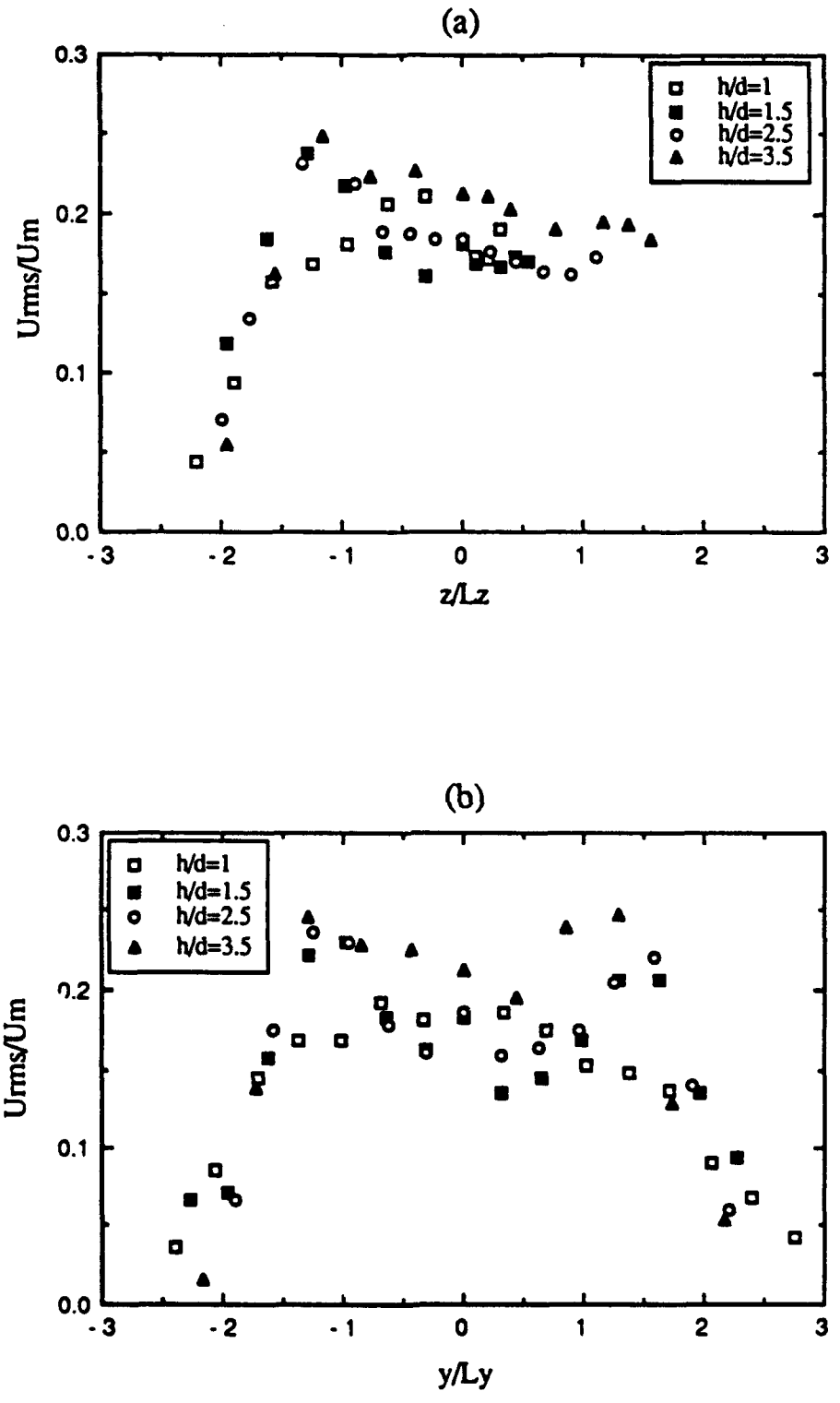


Figure 3.52 - Profiles of the rms value of the velocity fluctuation normalized by the local maximum mean velocity. Plot (a) profiles perpendicular to the free surface. Plot (b) profiles parallel to the free surface. U_e=200 cm/s, Re=1.27x10^4, x/d=24.

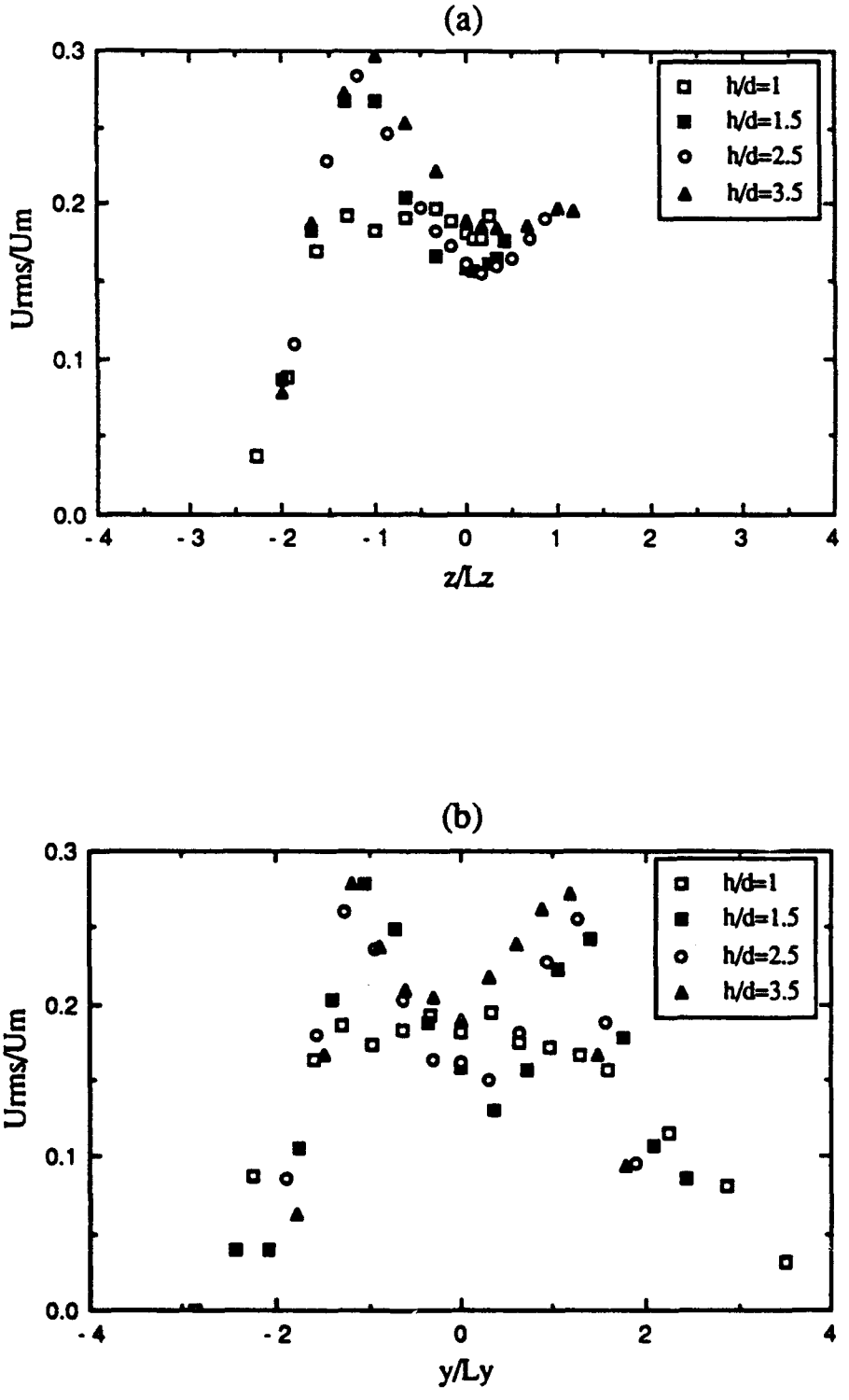


Figure 3.53 - Profiles of the rms value of the velocity fluctuation normalized by the local maximum mean velocity. Plot (a) profiles perpendicular to the free surface. Plot (b) profiles parallel to the free surface. U_e=200 cm/s, Re=1.27x10^4, x/d=32.

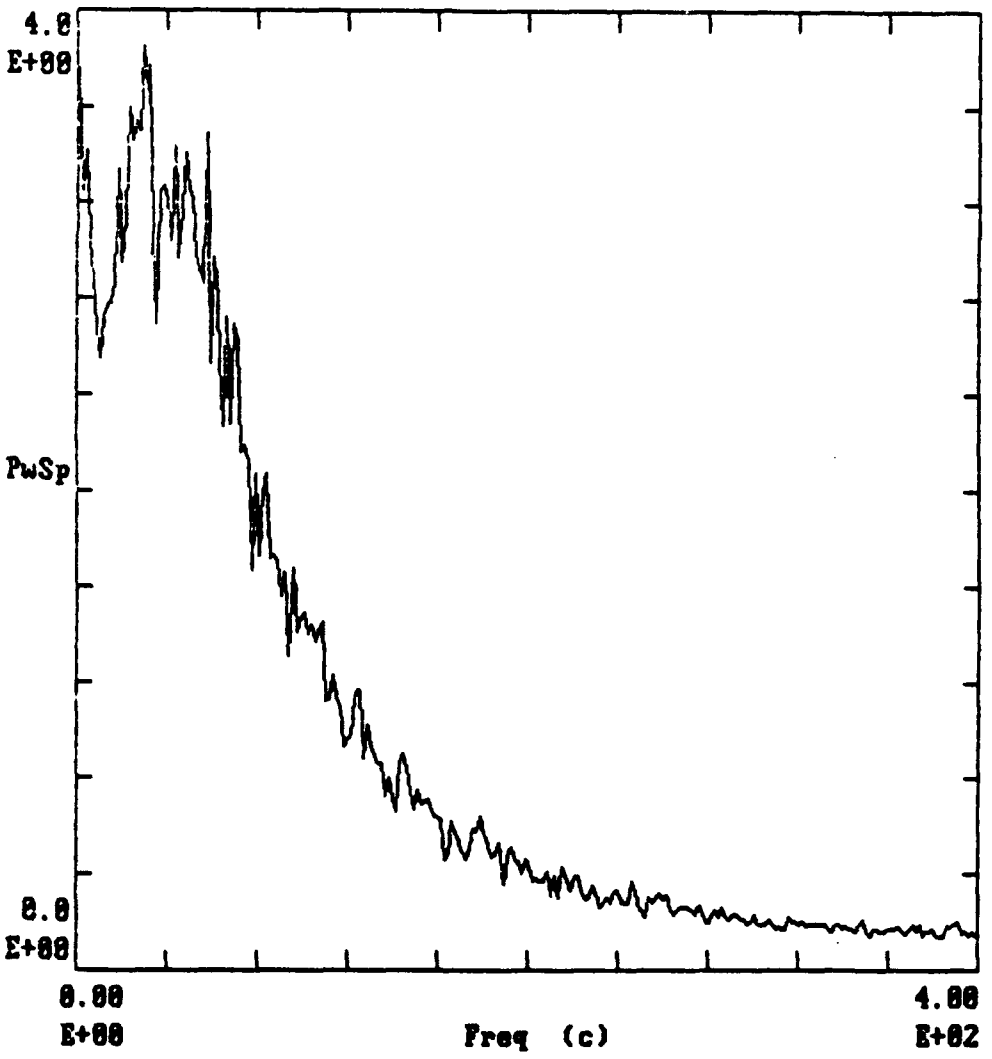


Figure 3.54 - Power spectrum of the velocity signal at x/d=8; y/d=0
U_e = 200 cm/s, Re = 1.27×10^4, h/d=1.

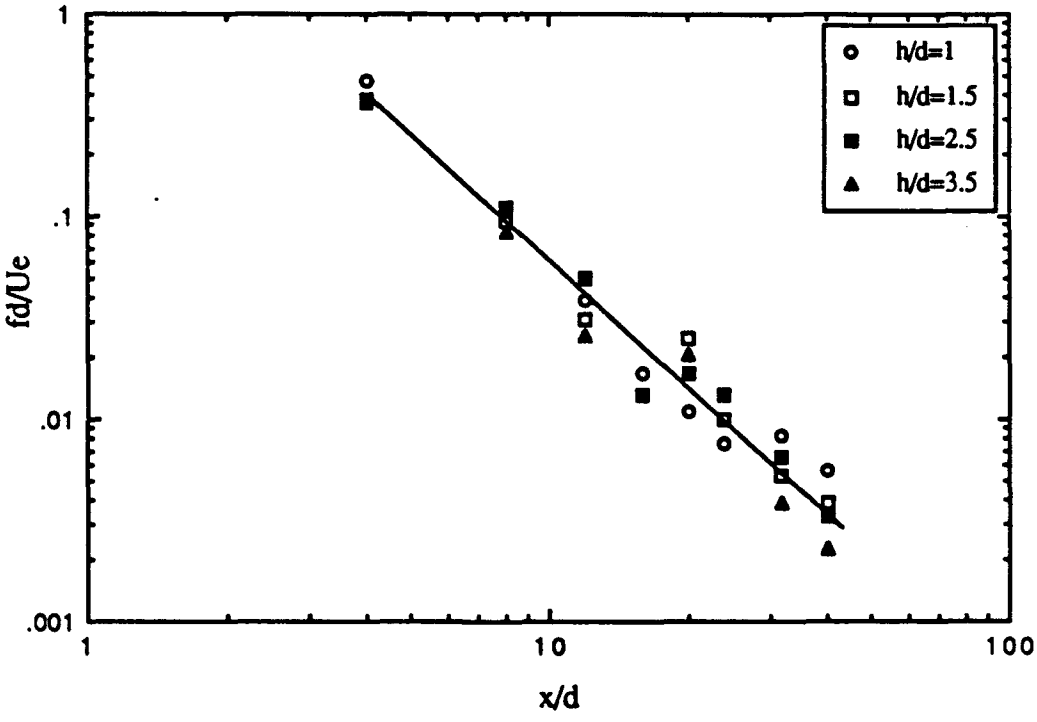


Figure 3.55 - Downstream evolution of the normalized frequency along the jet centerline. Straight line corresponds to the slope of -2. U_e=200 cm/s, Re=1.27x10^4.

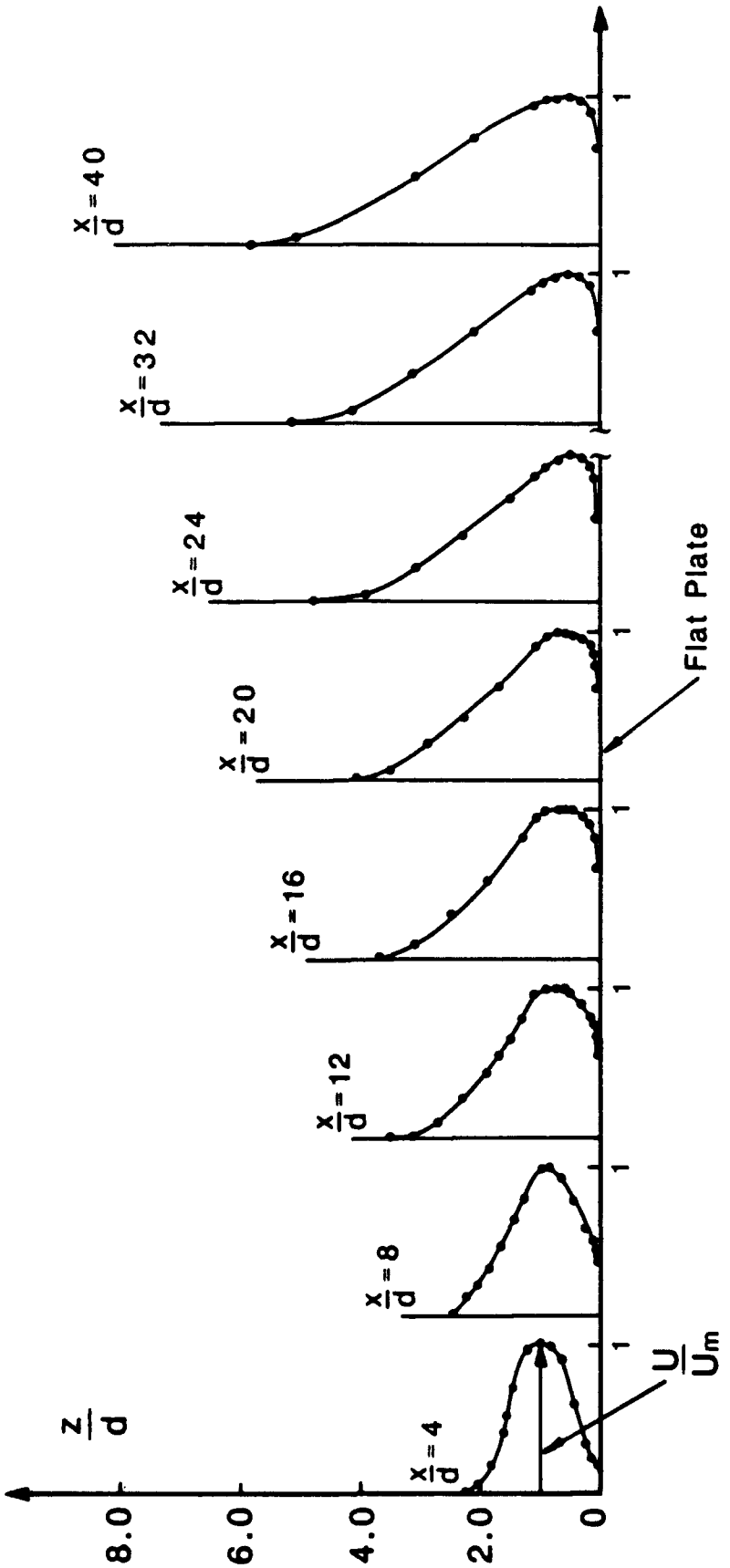


Figure 3.56 - Velocity profiles in the direction perpendicular to the solid wall.
U_e = 200 cm/s, Re = 1.27×10^4, h/d=1.

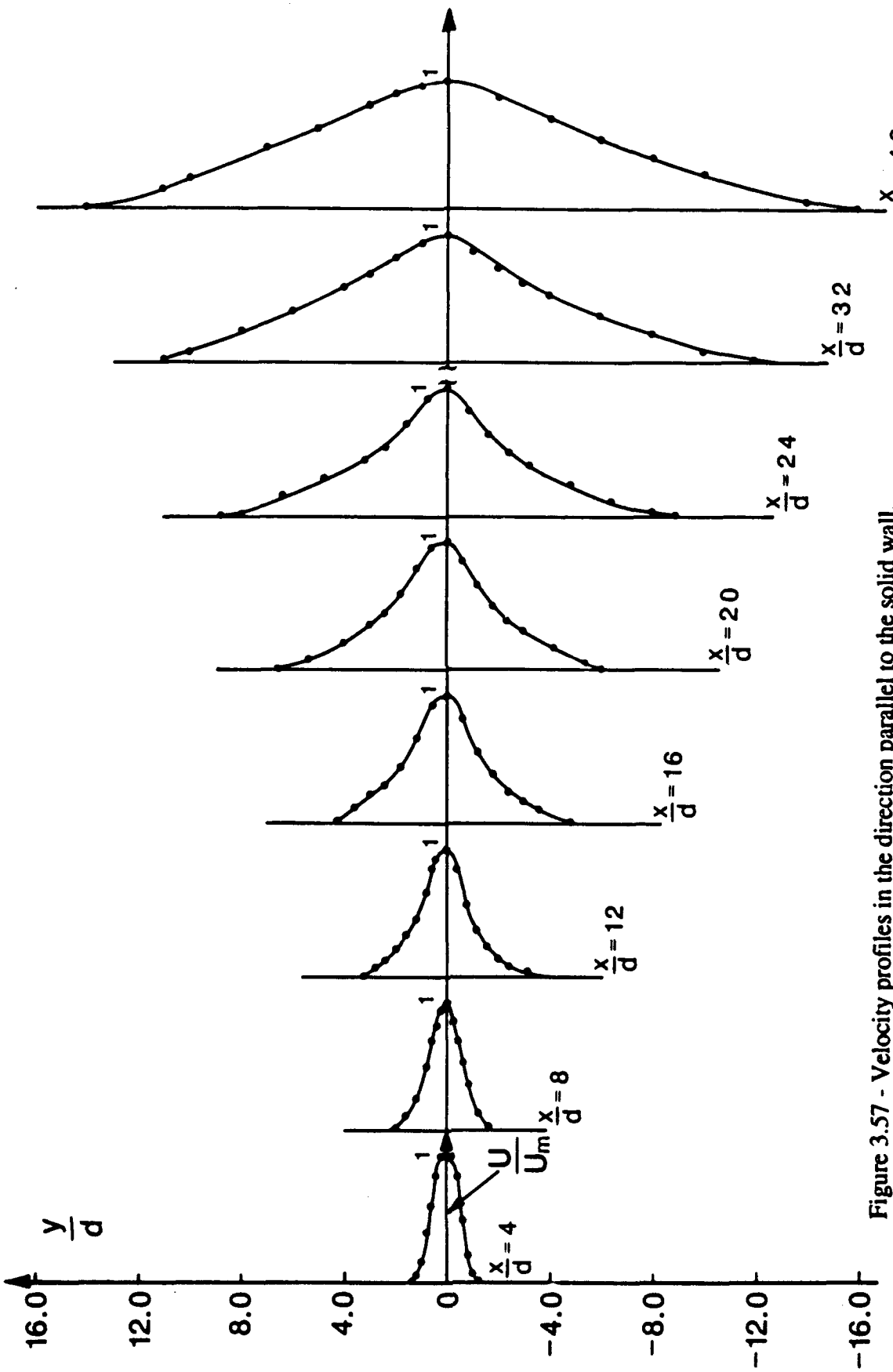


Figure 3.57 - Velocity profiles in the direction parallel to the solid wall.
U_e = 200 cm/s, Re = 1.27×10^4, h/d=1.

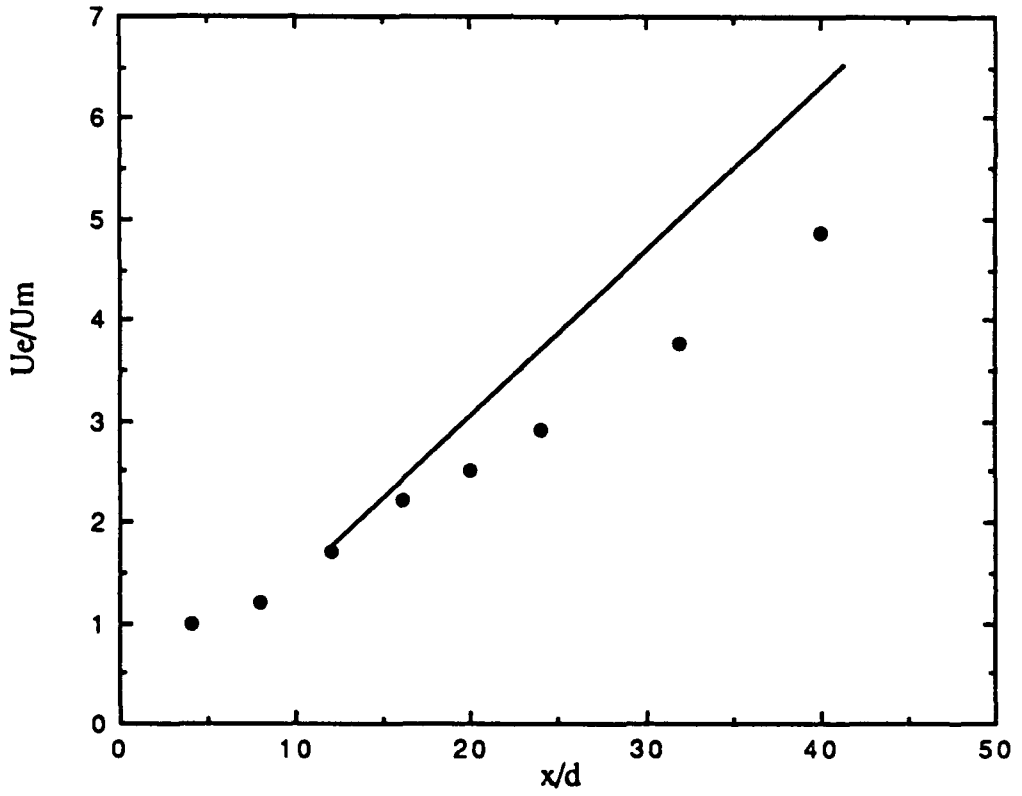


Figure 3.58 - Decay of maximum mean velocity with the downstream distance for the wall jet. ___, least squares linear fit to the free jet data. U_e = 200 cm/s, Re = 1.27×10^4, h/d=1.

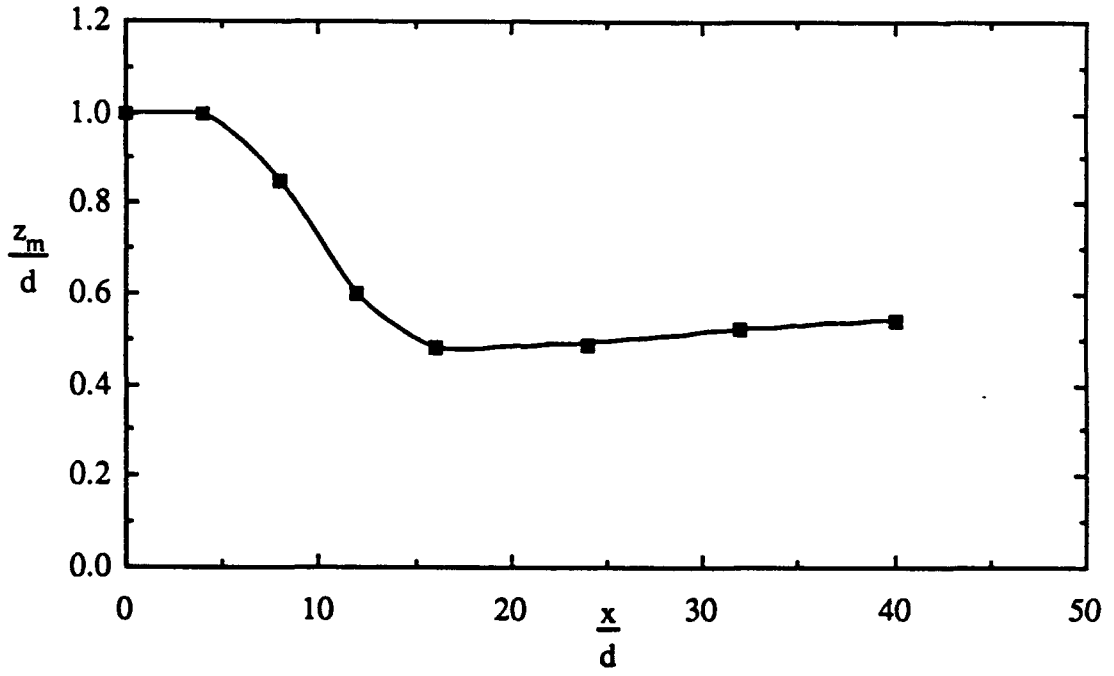


Figure 3.59 - Location of the maximum mean velocity for the wall jet. Solid symbols, distance from the solid wall. Ue= 200 cm/s, Re = 1.27×10^4 , h/d=1.

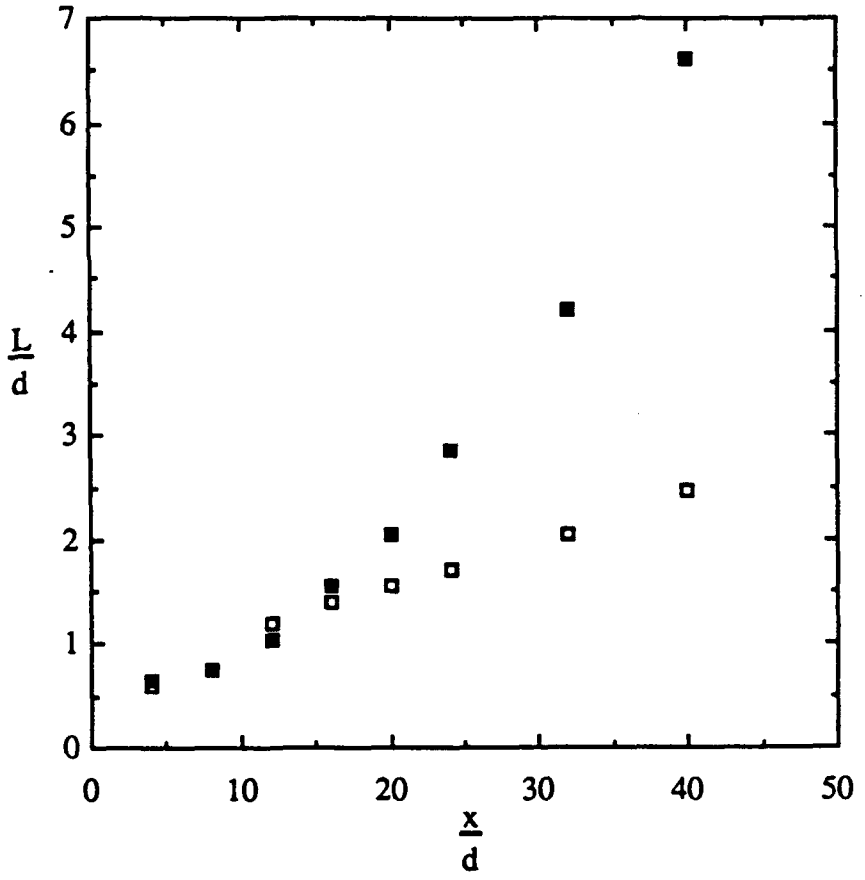


Figure 3.60 - Downstream evolution of half velocity width of the mean velocity profiles for the wall jet. Solid symbol, width parallel to the solid surface. Open symbol, width perpendicular to the solid surface.
Ue = 200 cm/s, Re = 1.27×10^4 , h/d=1.

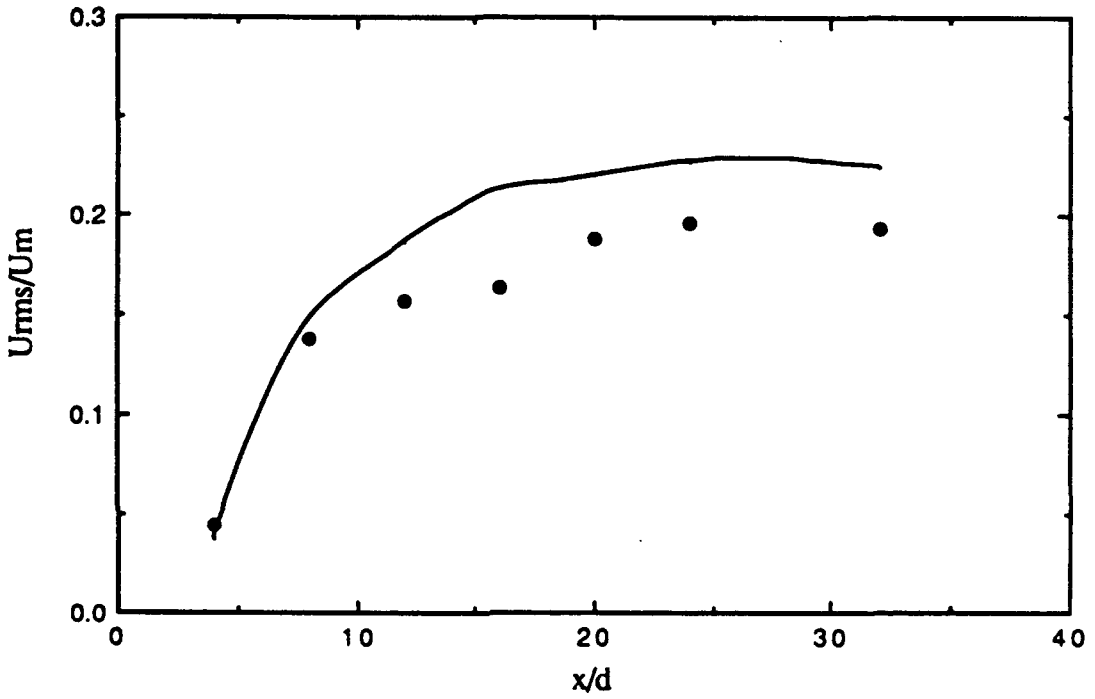


Figure 3.61 - Downstream evolution of the rms value of the velocity fluctuation for the wall jet. Solid curve represents the free jet data. U_e = 200 cm/s, Re = 1.27×10^4, h/d=1.

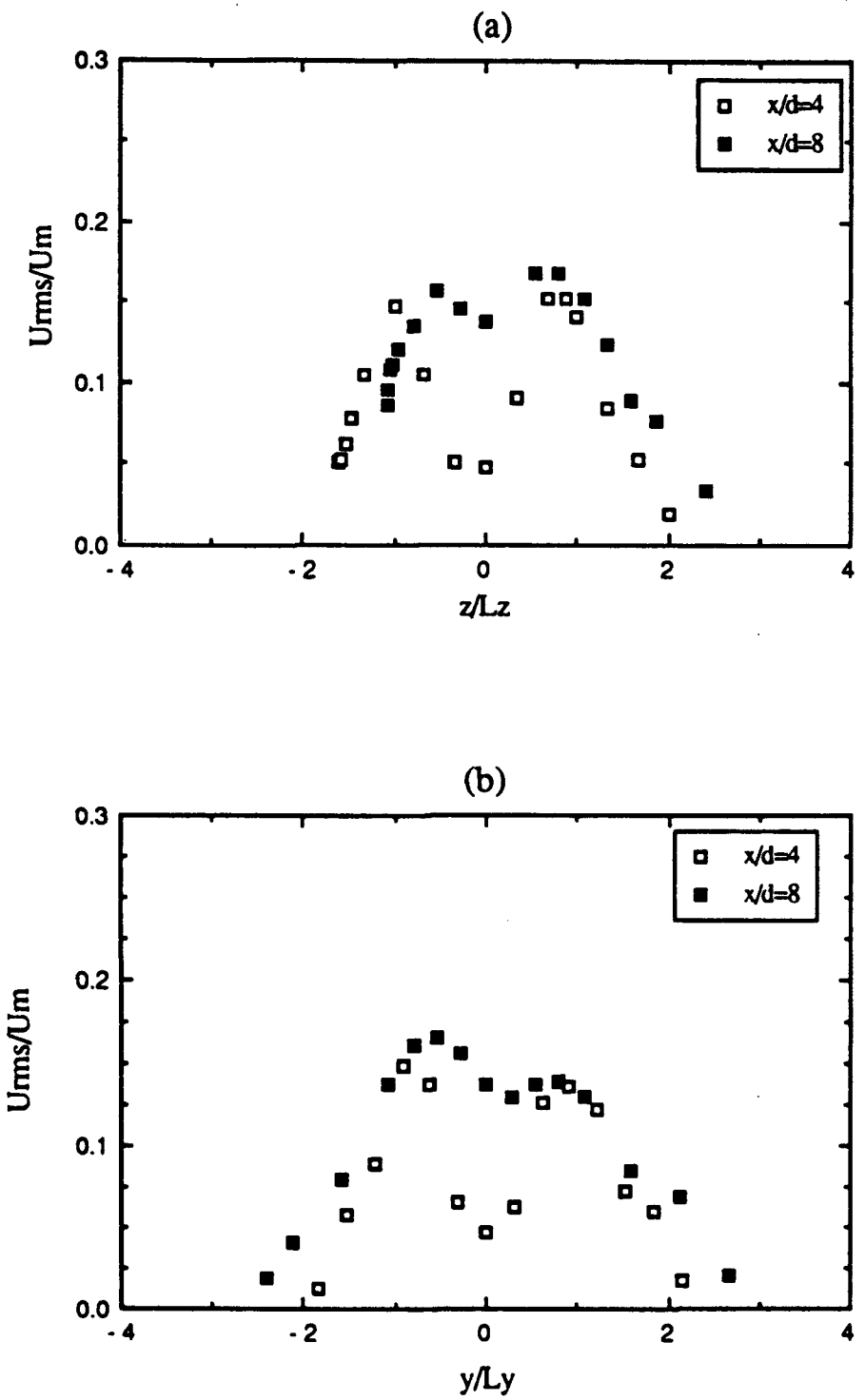


Figure 3.62 - Profiles of the normalized rms value of the velocity fluctuation for the wall jet. Plot (a) profiles perpendicular to the wall. Plot (b) profiles parallel to the wall.
U_e = 200 cm/s, Re = 1.27×10^4, h/d=1, x/d=4, 8.

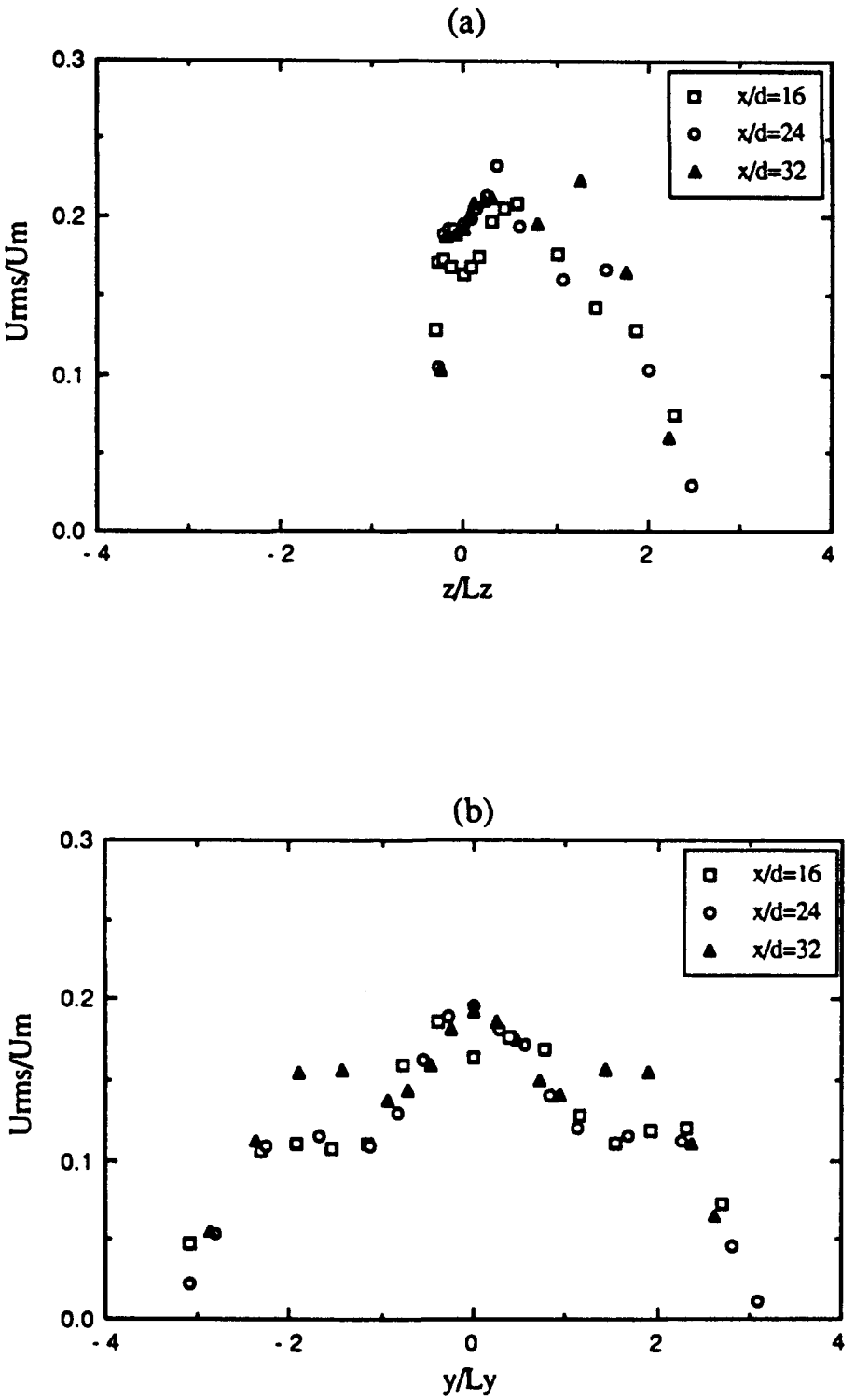


Figure 3.63 - Profiles of the normalized rms value of the velocity fluctuation for the wall jet. Plot (a) profiles perpendicular to the wall. Plot (b) profiles parallel to the wall.
U_e = 200 cm/s, Re = 1.27×10^4, h/d=1, x/d=16, 24, 32.

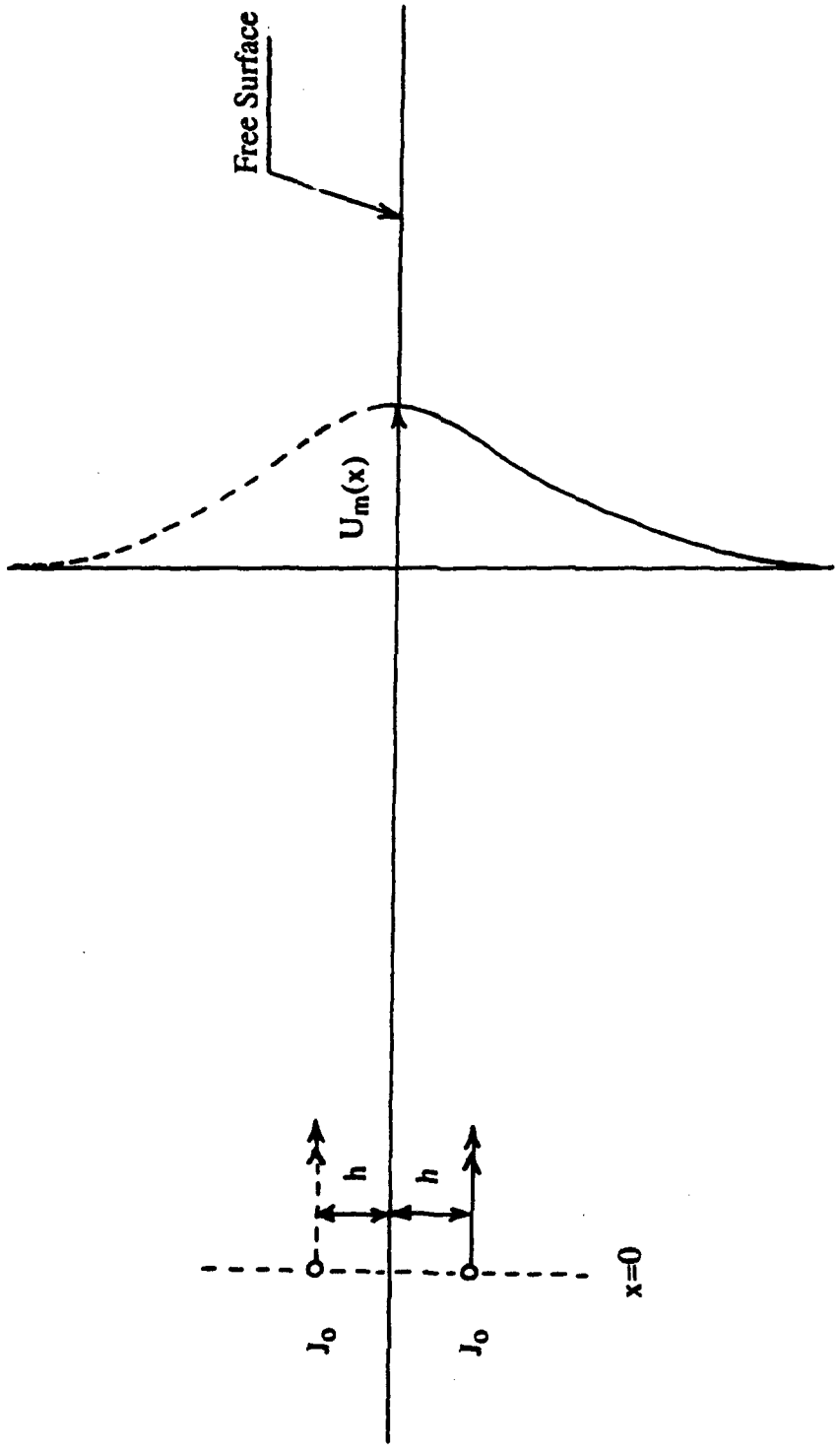


Figure 4.1 - Far field scaling of the free surface jet.

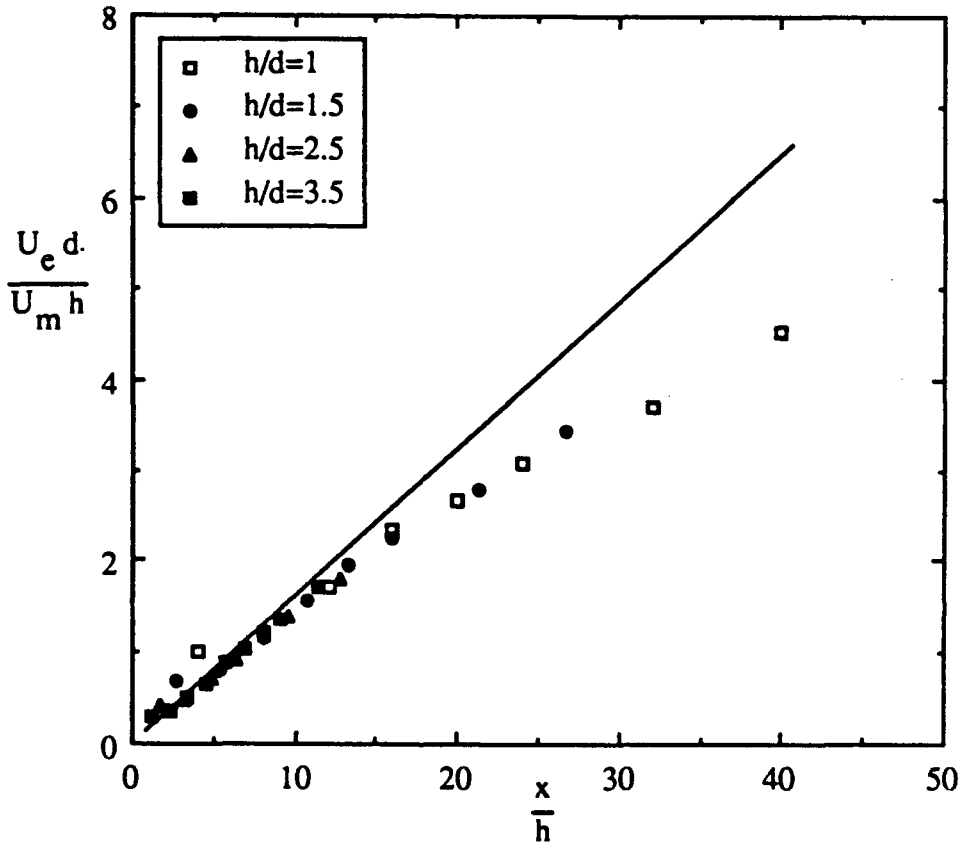


Figure 4.2 - Decay of maximum mean velocity for the free-surface jet. Solid line, slope = 0.162, corresponds to the free jet. Ue=200 cm/s, Re = 1.27×10^4 .

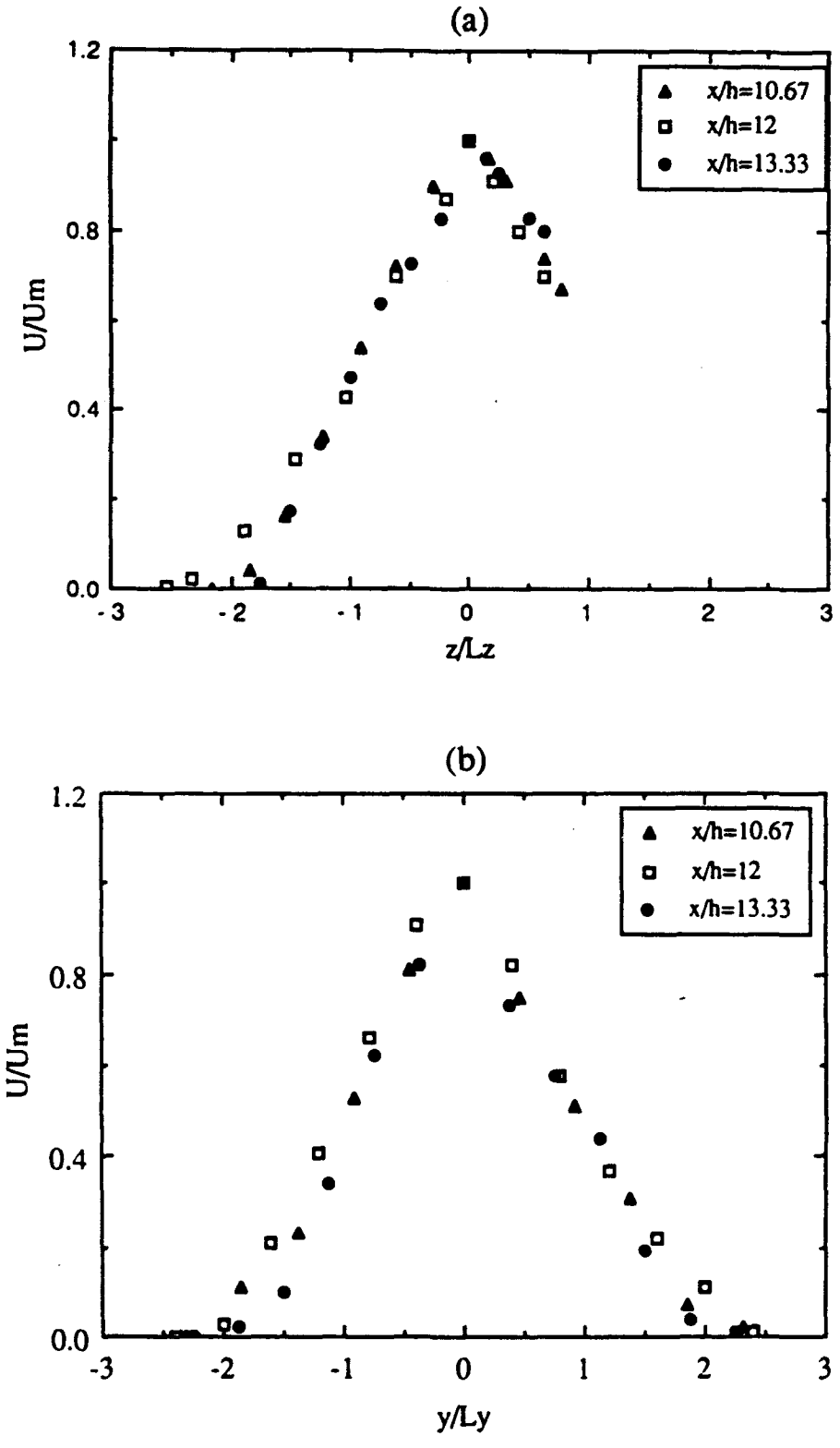


Figure 4.3 - Mean velocity similarity profiles for the free-surface jet. Plot (a) profiles perpendicular to the free surface. Plot (b) profiles parallel to the free surface.
U_e = 200 cm/s, Re = 1.27×10^4, x/h=10.67, 12, 13.33.

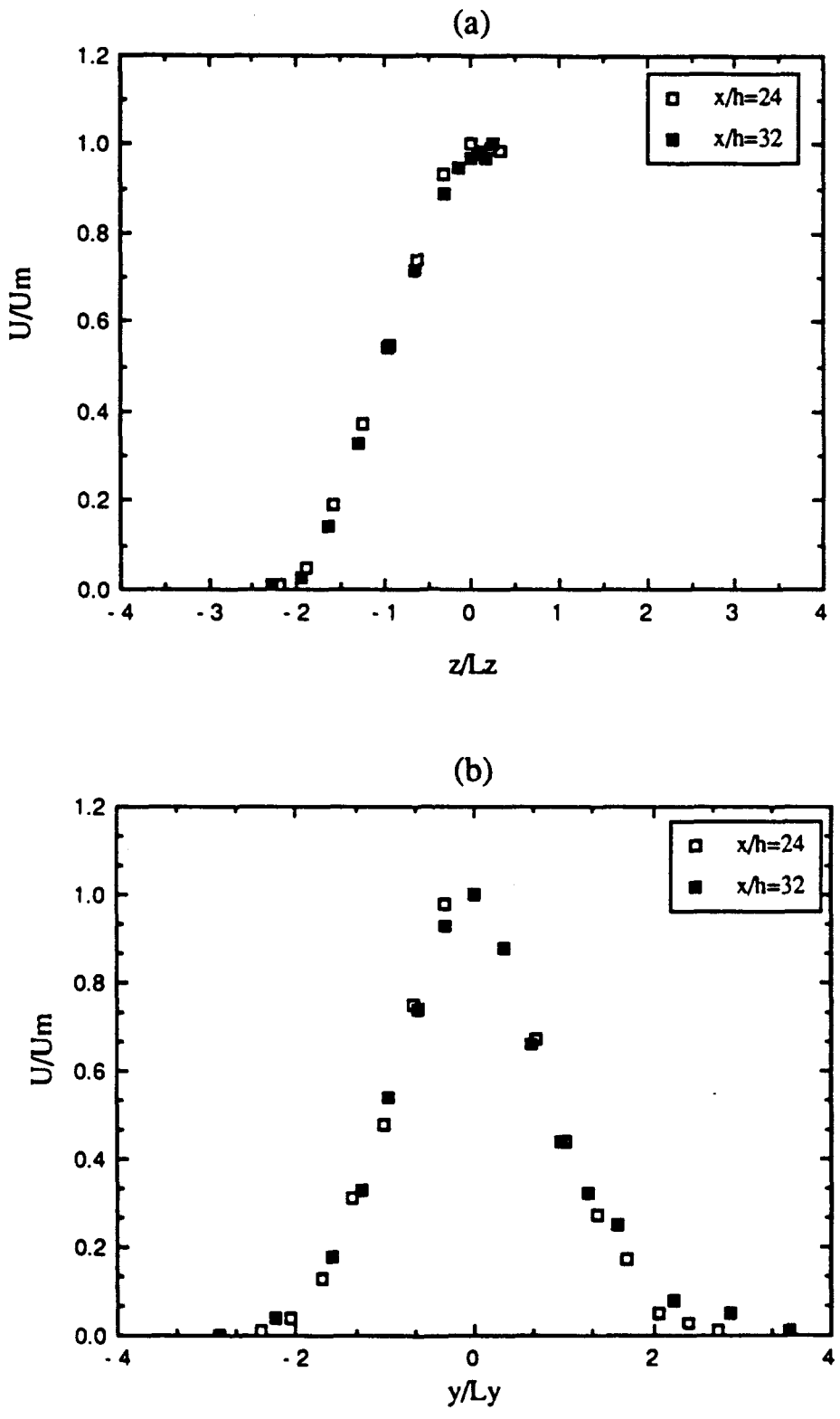


Figure 4.4 - Mean velocity similarity profiles for the free-surface jet. Plot (a) profiles perpendicular to the free surface. Plot (b) profiles parallel to the free surface.
U_e = 200 cm/s, Re = 1.27×10^4, x/h=24,32.

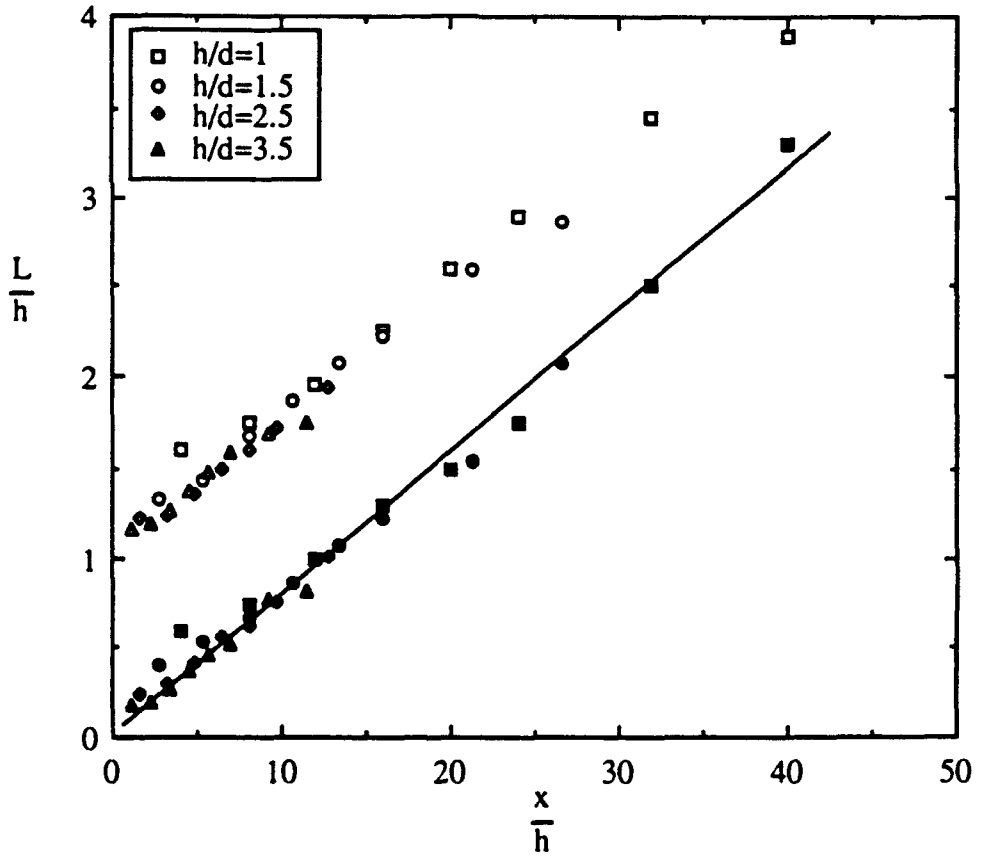


Figure 4.5 - Downstream evolution of half velocity width of the mean velocity profiles normalized by the jet depth h. Solid symbols, width parallel to the free surface. Open symbols, width perpendicular to the free surface.—— , least squares linear fit to the free jet data. Ue=200 cm/s, Re = 1.27×10^4.

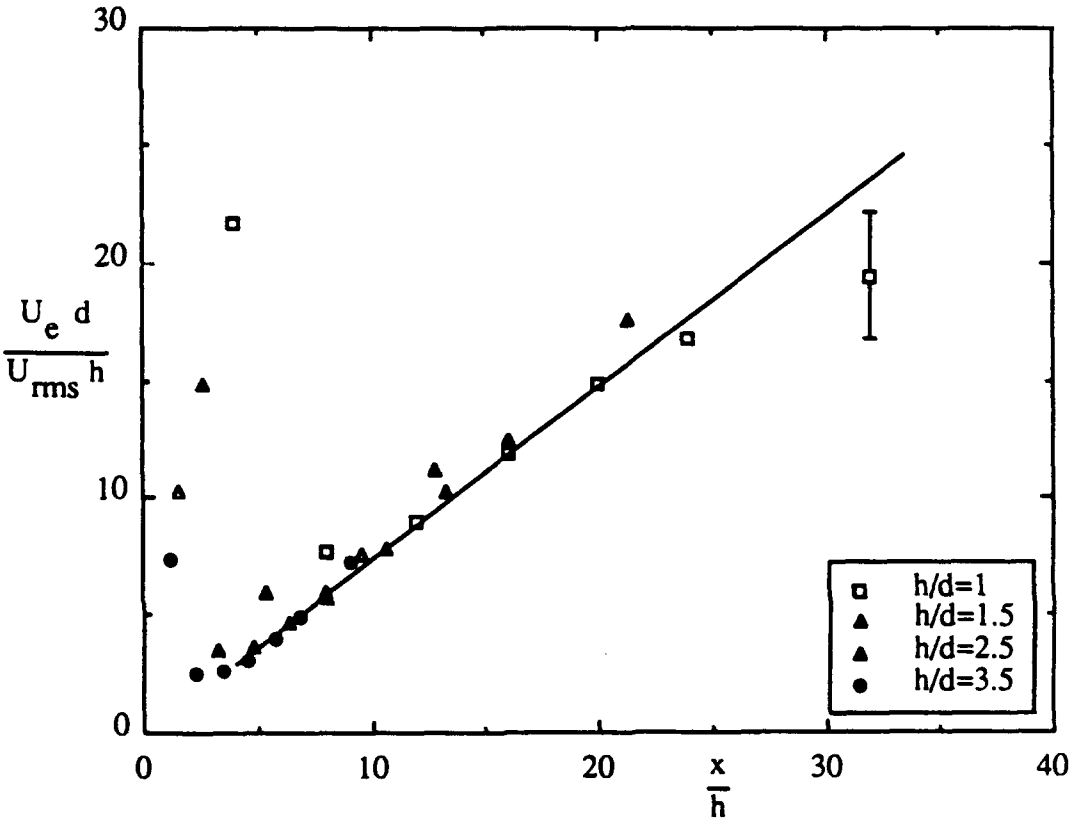


Figure 4.6 - Downstream evolution of normalized rms value of the velocity fluctuation along the centerline of the free surface jet. Solid line, least squares fit through the free jet data.
Ue = 200 cm/s, Re = 1.27×10^4.

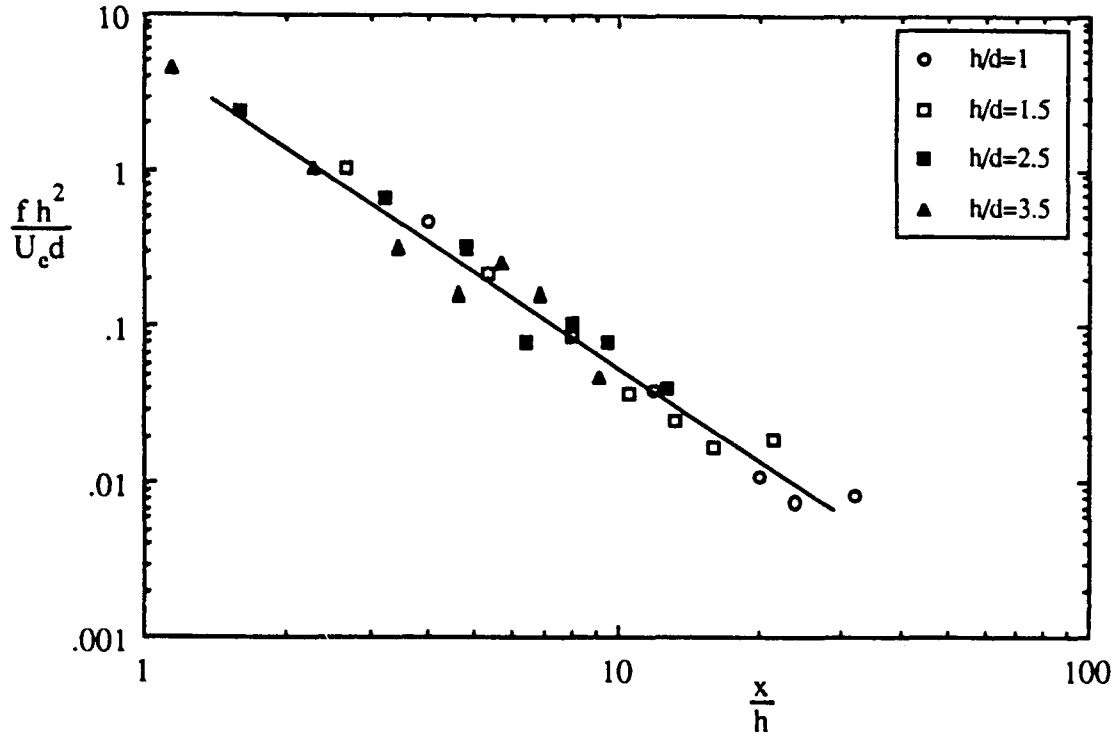


Figure 4.7 - Downstream evolution of normalized frequency along the jet centerline. Straight line corresponds to the slope of -2. Ue = 200 cm/s, Re = 1.27×10^4

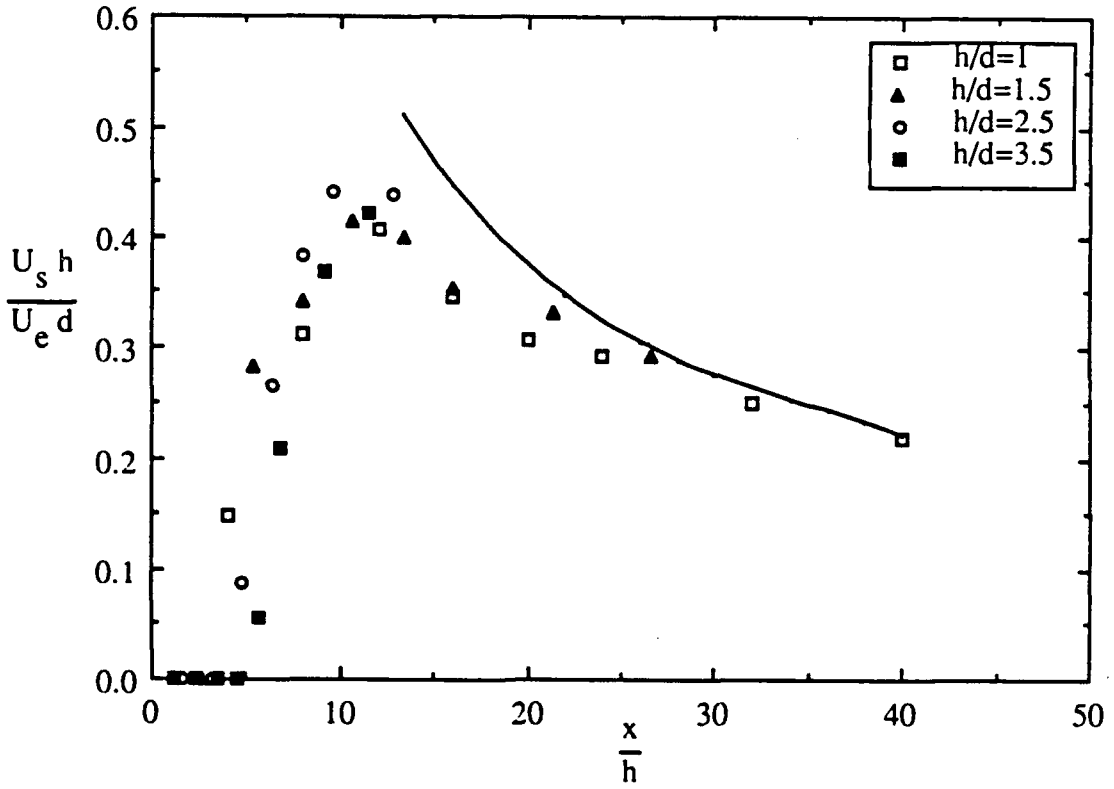


Figure 4.8 - Downstream evolution of normalized mean surface velocity. Solid curve, least squares fit through the maximum mean velocity data. Ue= 200 cm/s, Re = 1.27×10^4

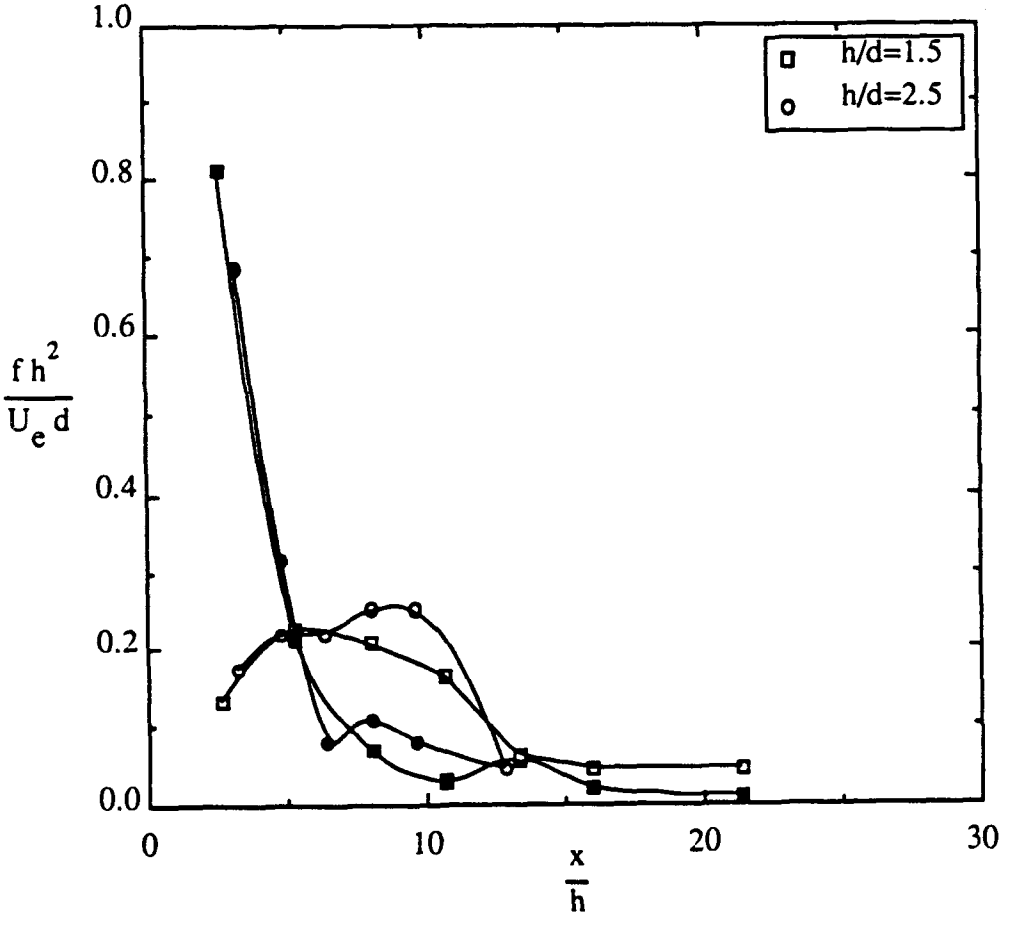


Figure 4.9 - Downstream evolution of normalized frequencies along the jet centerline. Solid symbols, frequency corresponding to velocity data. Open symbols, frequency corresponding to surface curvature data. Ue = 200 cm/s, Re = 1.27×10^3

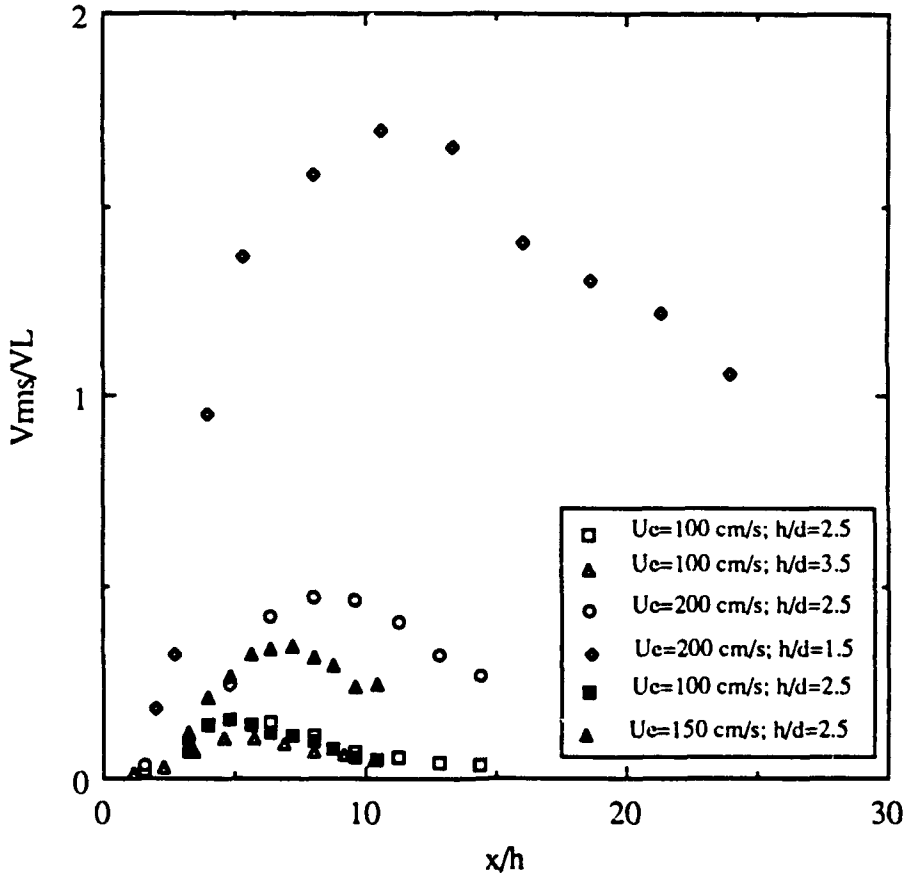


Figure 4.10 - Downstream evolution of the rms value of the surface curvature fluctuation along the jet centerline. Solid symbols d=1.27 cm. Open symbols d=0.64 cm.

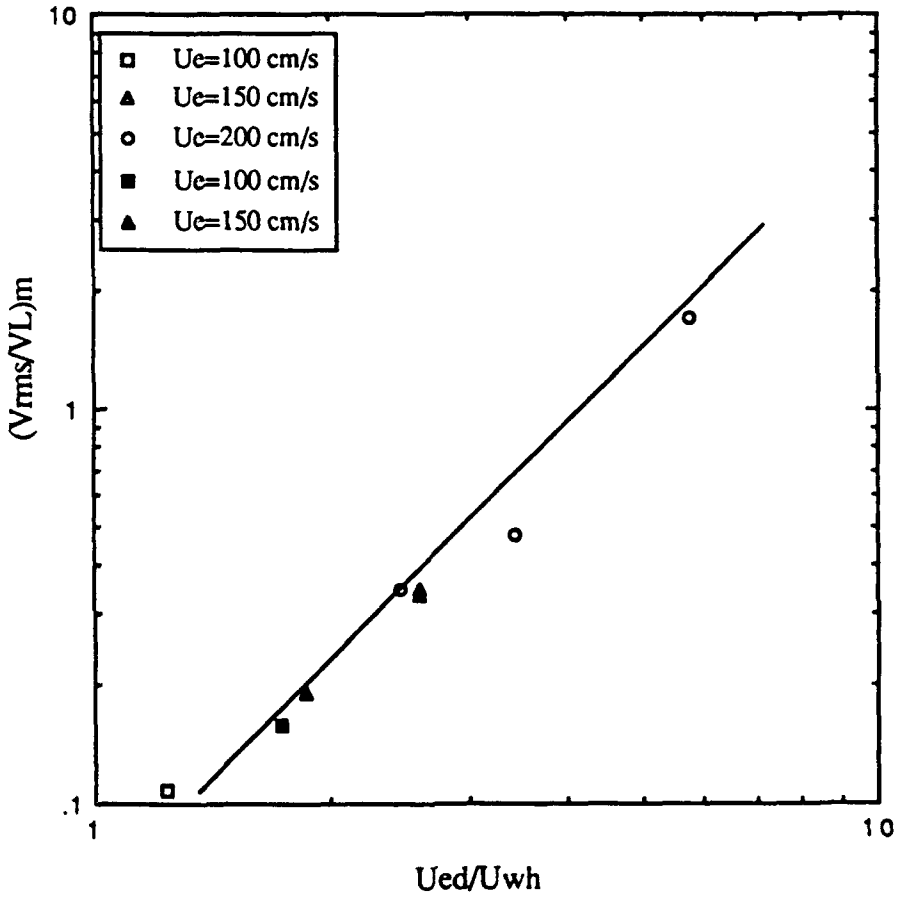


Figure 4.11 - Maximum rms surface curvature fluctuation as a function of the interaction 'strength'. Solid symbols d=1.27 cm. Open symbols d=0.64 cm. ___, slope=2.

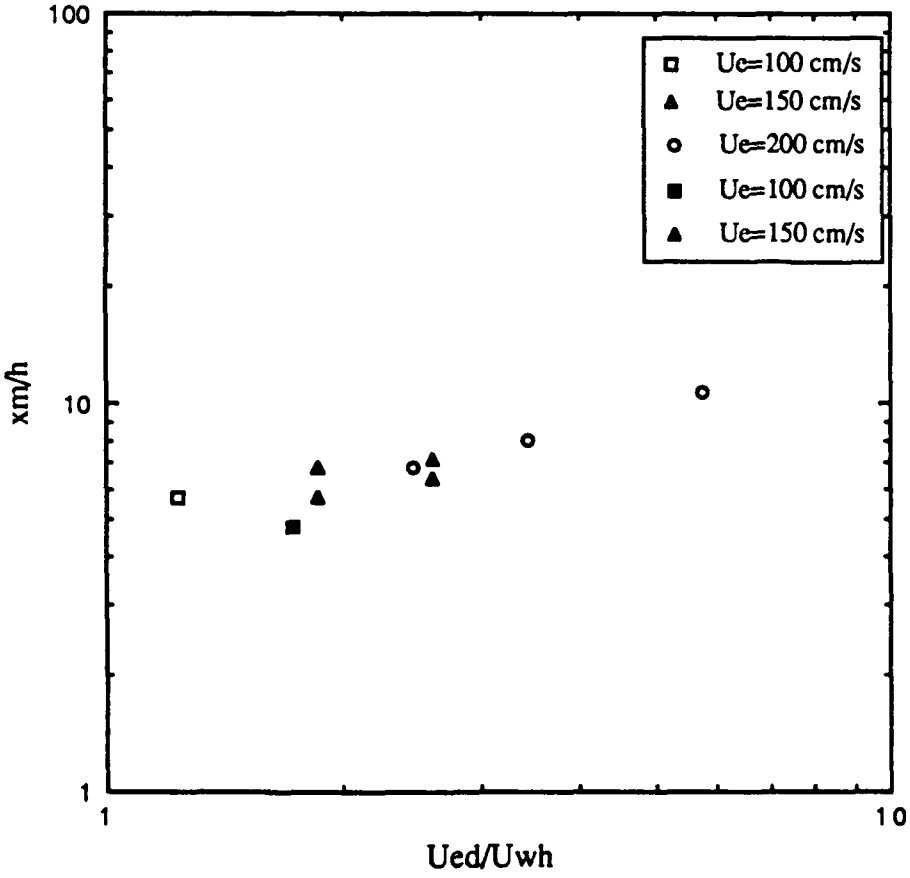


Figure 4.12 - Location of the maximum rms surface curvature fluctuation as a function of the interaction 'strength'. Solid symbols d=1.27 cm. Open symbols d=0.64 cm.

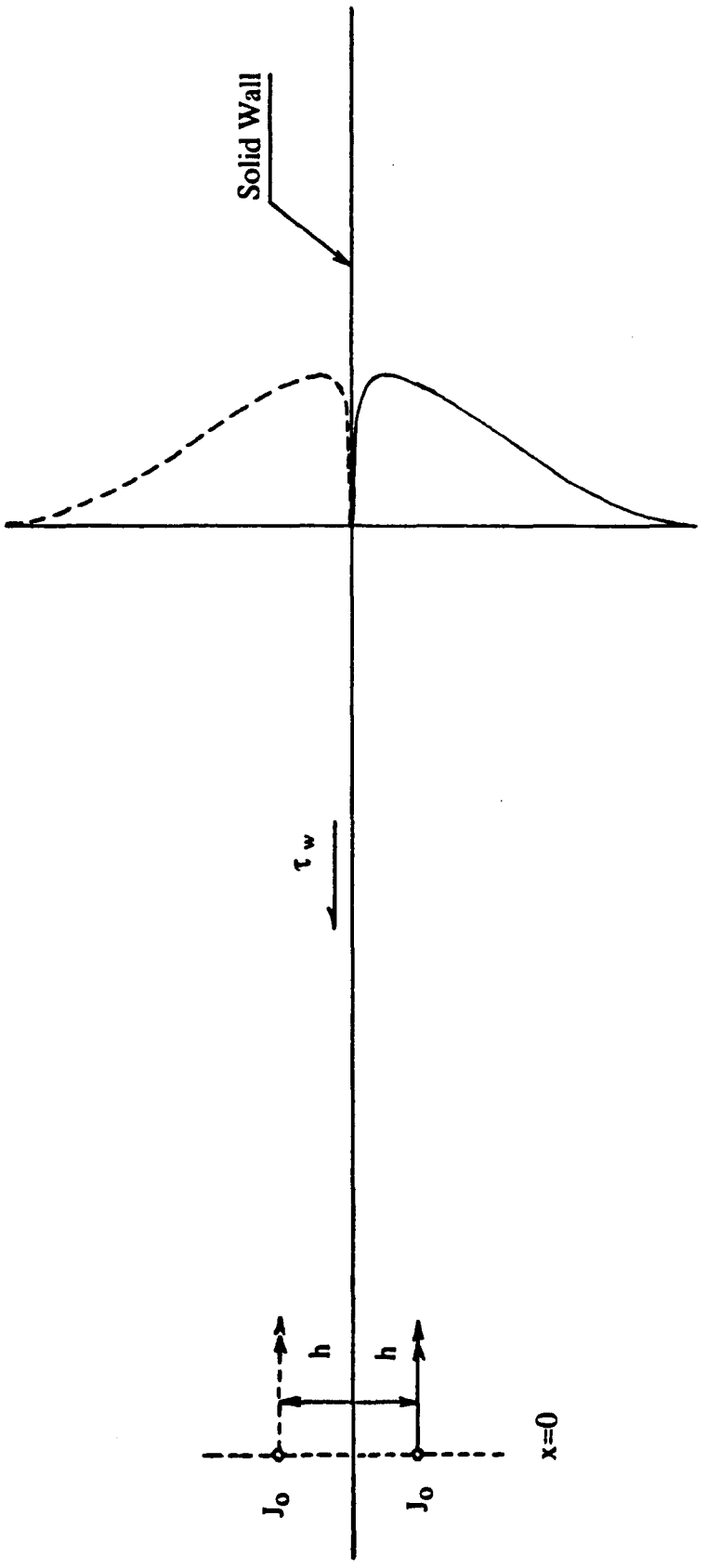


Figure 4.13 - Schematic diagram of the flow field for the wall jet.

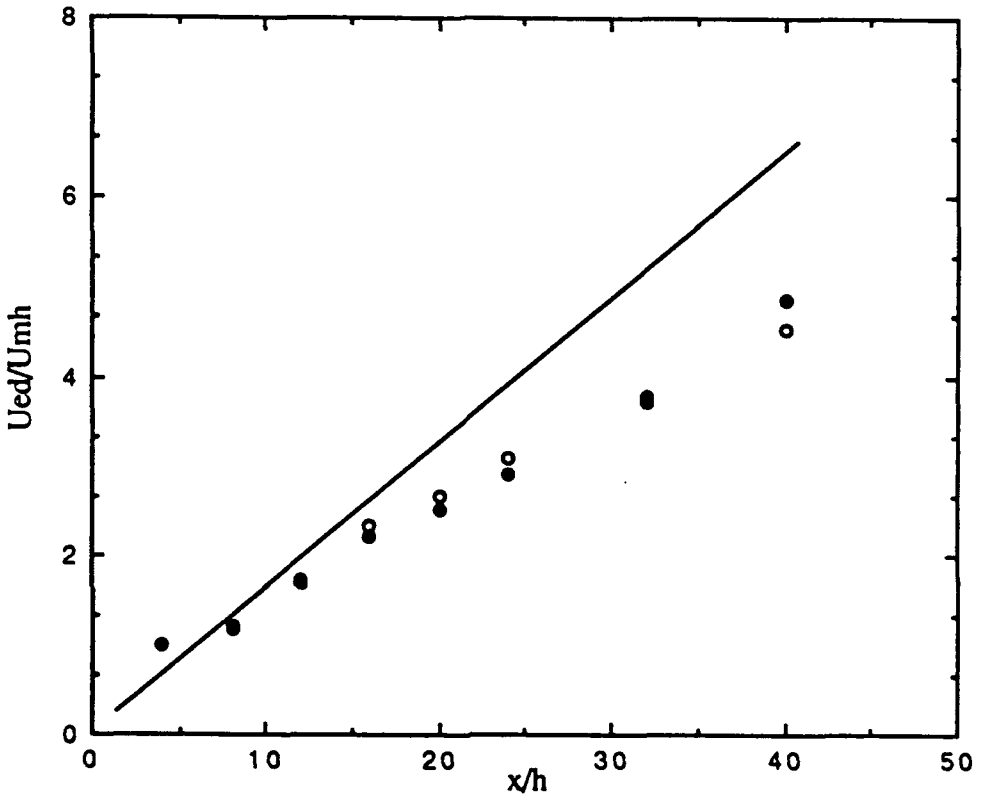


Figure 4.14 - Decay of maximum mean velocity for the wall jet and the free-surface jet. Solid symbol, wall jet. Open symbols, free-surface jet. Solid line corresponds to the free jet.
Slope=0.162. U_e = 200 cm/s, Re = 1.27×10^4, h/d=1.

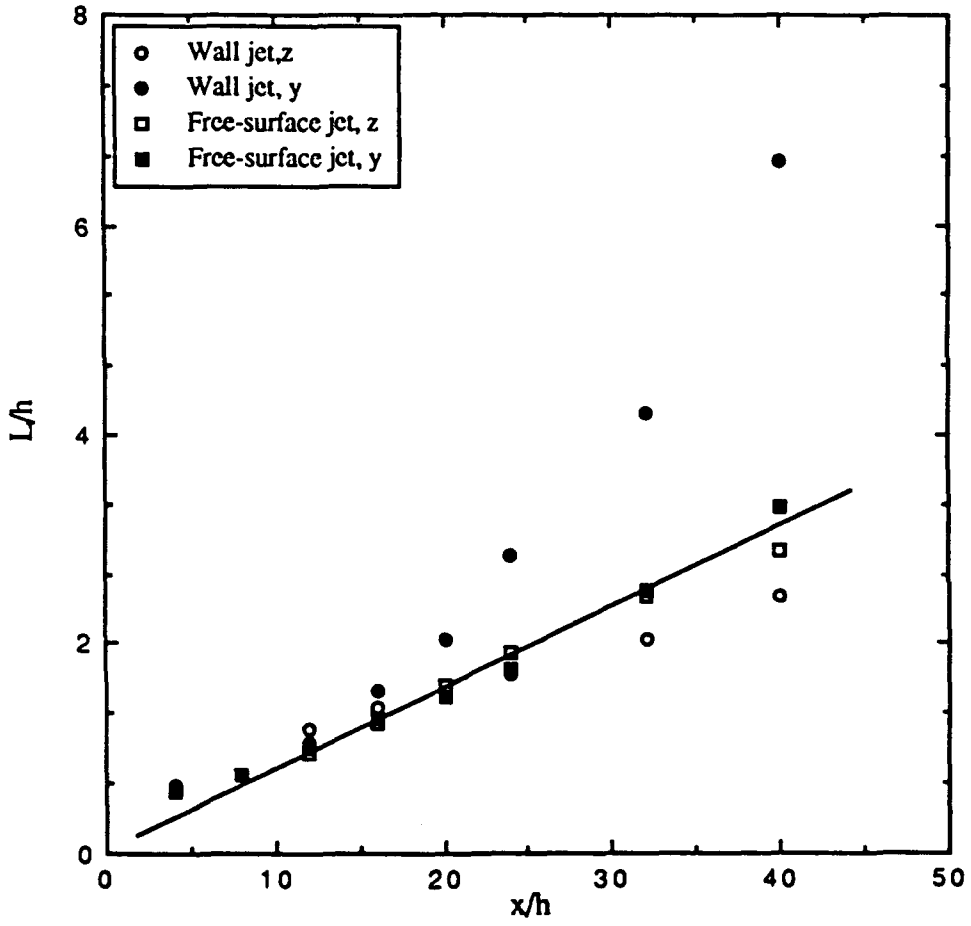


Figure 4.15 - Downstream evolution of half velocity width of the mean velocity profiles for the wall jet and the free-surface jet. Solid symbols width parallel to the surface. Open symbols width perpendicular to the surface.
U_e = 200 cm/s, Re = 1.27×10^4, h/d=1.

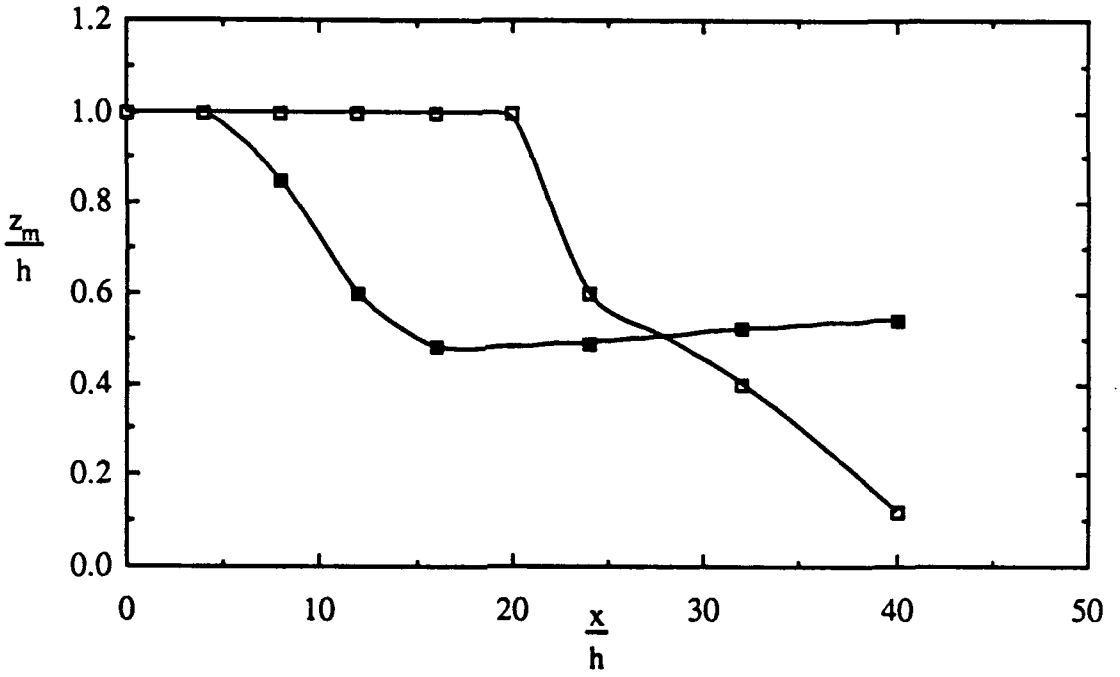


Figure 4.16 - Location of the maximum mean velocity. Solid symbols, distance from the solid wall. Open symbols, distance from the free surface. Ue= 200 cm/s, Re = 1.27 x 10^4, h/d=1.

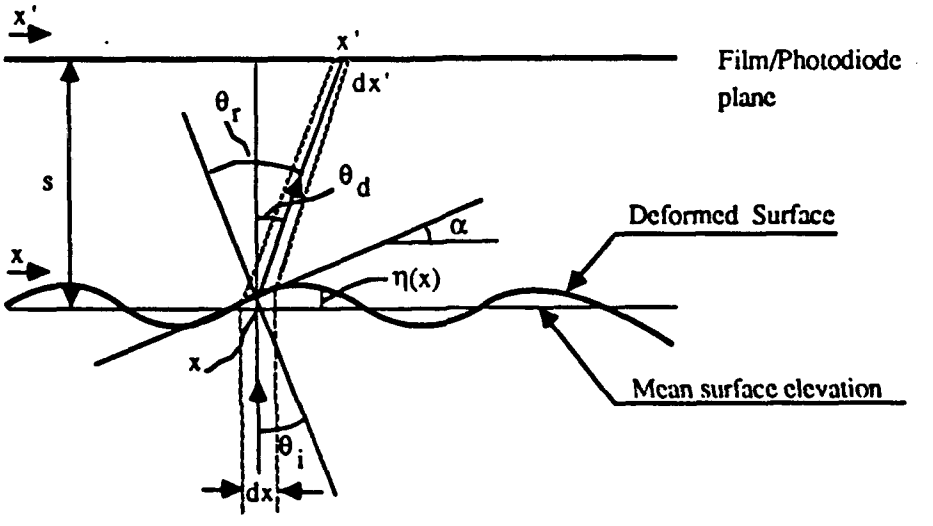


Figure A.1 - Geometry of the deformed water surface.

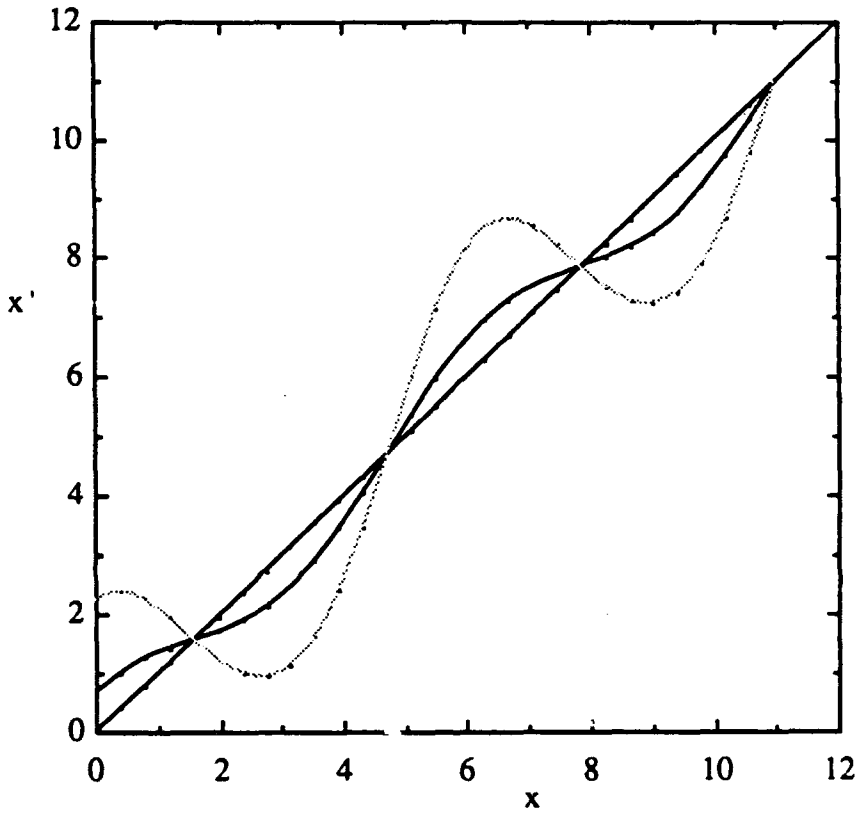


Figure A.2 - Plot of the location at which the ray of light intersects the photodiode plane, x', versus the location, $\hat{x}$, at which the incoming ray intersects the undisturbed surface.